Multi-Component Adsorption of Monoclonal Antibodies on Ceramic Hydroxyapatite

---

A Dissertation

Presented to

the faculty of the School of Engineering and Applied Science

University of Virginia

---

in partial fulfillment
of the requirements for the degree

Doctor of Philosophy

by

Yiran Wang

December 2019

APPROVAL SHEET

This Dissertation
is submitted in partial fulfillment of the requirements
for the degree of
Doctor of Philosophy

Author Signature: *Yiran Wang*

This Dissertation has been read and approved by the examining committee:

Advisor: Giorgio Carta

Committee Member: Bryan Berger

Committee Member: Liheng Cai

Committee Member: Rachel A. Letteri

Committee Member: Jogender Tushir-Singh

Committee Member: _____

Accepted for the School of Engineering and Applied Science:

Craig H. Benson, School of Engineering and Applied Science

December 2019

Abstract

Understanding the mechanism of protein adsorption and transport inside of chromatographic

adsorbent is critical for the downstream process design of the pharmaceutical industry, especially

for the multicomponent system, such as protein monomer and its isoform dimer. This work

forces on understanding a new form of hydroxyapatite (HAP) adsorbent, ceramic hydroxyapatite

(CHT). The work determined the internal structure of two types of CHT, Type I and Type II, and

the adsorption behavior of a monoclonal antibody (mAb) in monomeric and dimeric forms.

Internal porosities and apparent pore radii based on inverse size exclusion chromatography are

0.73 and 30 nm for Type I and 0.70 and 49 nm for Type II. Adsorption isotherms show higher

maximum capacities on Type I compared to Type II, in approximate agreement with the ratio of

surface areas. The isotherms are dependent on the Na^+ concentration consistent with an

electrostatically driven mechanism. Mixture adsorption shows selectivity toward the dimer.

Effective pore diffusivities for strong binding conditions, obtained by confocal microscopy, are

much smaller than the non-binding values for Type I but essentially the same for Type II,

indicating that diffusional hindrance by the bound protein is greater in the smaller pores of Type

I.

The separation dynamics of monoclonal antibody monomer/dimer mixtures are first examined by

frontal analysis. The binding capacity and selectivity are dependent on the CHT type and salt

concentration. While the rate of protein adsorption on CHT Type I is slow and controlled largely

by pore diffusion resulting in relatively poor separation, adsorption on CHT Type II is much

faster and better separation is obtained than with Type I. However, comparison with predictions

based on pore diffusion alone, reveals the presence of additional resistances associated with

adsorption and displacement kinetics. A spreading kinetics model assuming multiple binding

configurations coupled with pore diffusion was developed to describe these effects and found to be in quantitative agreement with the frontal analysis results and able to predict the separation achieved for conditions outside the range of the experiments. To help validate the assumed mechanism, isocratic elution experiments were also conducted at low protein loads. The chromatograms could be described by the solution of the spreading model coupled with pore diffusion in the linear region of the isotherm with parameters determined from the analytical moments confirming a trend of increasing tendency to spread and slower kinetics as the salt concentration is decreased and binding strength is increased.

Multicomponent separation is then examined by the gradient elution chromatography on two types of CHT adsorbents. Experimental results show that the pH drop introduced by the increased sodium concentration is significantly more extreme during a sodium chloride gradient compared to a sodium phosphate gradient. Therefore, a sodium phosphate gradient facilitates a better separation for this model mAb. The empirical interpolation (EI) method is employed in concert with the pore diffusion model coupled with lumped adsorption kinetics to predict multicomponent overloaded elution behavior. Predictions show good agreement with the experimental results for protein loads up to 85% of the column binding capacity.

Finally, a comparative study of the optimized separation process in the case of frontal analysis and gradient elution chromatography is presented using these mechanistic models developed in this work. The optimization behavior in terms of productivity and yield is examined under the constraints of monomer purity. The column simulations reveal that gradient elution exhibits higher productivity and yield compared to frontal analysis. However, with process optimization, frontal analysis can still achieve a separation process with 80% yield alongside a monomer purity cut-off at 95% which is applicable in an industrial setting.

Acknowledgments

Firstly, I would like to express my sincere gratitude to my advisor Prof. Giorgio Carta for the continuous support of my Ph.D study and related research, for his patience, motivation, and immense knowledge. He demonstrated what a brilliant and hard-working scientist can accomplish. It wouldn't have been possible to conduct this research without their precious support.

I would also like to thank my advisory committee members: Prof. Bryan Berger, Prof. Liheng Cai, Prof. Rachel Letteri and Prof. Jogender Tushir-Singh not only for their time and extreme patience but for their intellectual contributions to my development as a scientist.

I would also like to thank Bio-Rad for providing the financial support my research, AstraZeneca for providing the material for this work, and Bristol-Myers Squibb for a valuable industrial experience.

I would like to thank all my friends, the previous and current Carta lab members, especially Yige, Shaojie, Jing, Mimi, Jason, Arch, Preston, Andreas, Lucas and Joey. My experience in Charlottesville and in the lab was greatly enhanced because of all their support and companion. I would also like to thank Patricia for her valuable help during her visiting at UVA.

I would like to thank my family, especially my mom, Xiumin, for guiding me as a person, encouraging me to pursue my dream and supporting me all the time.

Finally, I want to thank with love to Ang for all his love, comfort, support, encourage, entertain and help throughout my time in graduate school.

Table of contents

List of Figures

List of Tables

List of Symbols

A	steric mass action constant during linear gradient elution experiments (mM^z) or the area under the peak in the EMG calculation
A_{iSEC}	surface area per adsorbent determined by inverse size exclusion chromatography (m^2/mL)
A_{BET}	surface area per adsorbent determined by Brunauer-Emmett-Teller method (m^2/mL)
Bi	Biot number
C	protein concentration in solution (mg/mL)
C_0	initial protein concentration in solution (mg/mL)
C_F	protein feed concentration (mg/mL)
C_{Na^+}	sodium concentration in solution (mM)
$C_{Na^+}^{initial}$	initial mobile phase sodium concentration (mM)
$C_{Na^+}^{final}$	final mobile phase sodium concentraton (mM)
C_{Load}	protein load concentration (mg/mL)
c	protein concentration in adsorbent pores (mg/mL)
c^*	equilibrium protein concentration in mobile phase (mg/mL)
CV_I	emergence of first shock front during two component frontal analysis experiments
CV_{II}	emergence of second shock front during two component frontal analysis experiments
CV_G	duration of the gradient in column volume units
D	column diameter (cm)
D_0	free solution diffusivity (cm^2/s)
D_e	effective pore diffusivity (cm^2/s)
D_L	axial dispersion coefficient (cm^2/s)
d_p	particle diameter (μm)
h	reduced HETP
K_D	distribution coefficient
K_d	dissociation equilibrium constant in BLI experiments ($= k_d/k_a$)
K_L	equilibrium constant in Langmuir isotherm (mL/mg)

K_S	equilibrium constant for the reversible conversion on the CHT surface
k	kinetic rate constant in column modeling (s^{-1})
k'	retention factor
k_a	association rate constant in BLI modeling (M^{-1} s^{-1})
k_d	dissociation rate constant in BLI modeling (s^{-1})
k_{des}	desorption rate constant ($mM^{-\beta}$ s^{-1})
k_f	film mass transfer coefficient (cm/s)
k'_∞	protein non-binding retention factor
k'_{Na^+}	salt rentention factor
k_L	rate constant in Langmuir isotherm (mg mL^{-1} s^{-1})
k_S	rate constant for the reversible conversion on the CHT surface (s^{-1})
L	column length (cm)
N	actual number of plates
n	refractive index of solution
P	process productivity (mg mL^{-1} min^{-1})
$Pr\,Y$	the product of process productivity and yield (mg mL^{-1} min^{-1})
q	adsorbed phase protein concentration (mg/mL)
q_m	maximum binding capacity in Langmuir isotherm (mg/mL)
q_L	protein concentration in the exchangeable bound state (mg/mL)
q_S	protein concentration in the unexchangeable bound state (mg/mL)
q^*	equilibrium adsorbed phase concentration (mg/mL)
$\langle \hat{q} \rangle$	average protein concentration in adsorbent (mg/mL)
r	particle radial coordinate in column modeling
r_m	molecule radius (nm)
r_L	rate of exchange with molecules in solution according to the Langmuir model
r_S	radial position of adsorption front in confocal microscopy experiments (μm) or rate of reversible conversion on the CHT surface according to spreading model
r_p	adsorbent radius (μm)
r_{pore}	adsorbent pore radius (nm)
t	time (s)

t_{cycle}	total cycle time (min)
t_G	retention time of the Gaussian input function in the EMG function (s)
t_0	offset time at the start of dissociation phase in BLI experiments (s)
u	superficial velocity (cm/s)
V_C	column volume (mL)
V_{Load}	protein load volume (mL)
V_{Elute}	elution volume (mL)
V_R	retention volume (mL)
v	interstitial velocity (cm/s)
v'	reduced velocity
x	column axial coordinate in column modeling
Y	process yield
z	protein effective charge

Greek Symbols

$\alpha_{i,j}$	adsorbent selectivity for species i over species j
β	constant parameter describing the ion impact on protein adsorption kinetic
ε	column extraparticle void fraction/porosity
ε_p	adsorbent intraparticle void fraction tested by salt
ε_p'	adsorbent intraparticle void fraction tested by protein
ϕ	column phase ratio
Γ	binding signal in BLI experiments (nm)
Γ_m	maximum binding signal in BLI experiments (nm)
γ	normalized gradient slope (mM)
μ_0	zeroth moment
μ_1	first momet of peak (s)
μ_2'	second central moment (s^2)
μ_3'	third central momennt (s^3)
ρ	adsorbent density (g/mL)

ρ_{water} water density (g/mL)

ρ_{HAP} HAP crystal density (g/mL)

ρ_{s} dimensionless front position in confocal microscopy experiments

σ_{G} standard deviation of the Gaussian peak of EMG function

τ Decay time of the system constant of EGM function

Chapter 1 Introduction and Objectives

1.1 Introduction

1.1.1 Therapeutic monoclonal antibodies

An antibody (Ab), also known as an immunoglobulin (Ig), is a large (~150 kDa) glycoprotein used by the immune system to identify and neutralize antigens or pathogens. Monoclonal antibodies (mAbs) are identical copies of an antibody that are used for therapeutic purposes. It was first generated through somatic cell hybrids by Kohler and Milstein in 1975 (Köhler and Milstein, 1975). After 10 years, in 1986, the first commercialized therapeutic antibody (Orthoclone OKT3®) was approved for the prevention of kidney transplant rejection by targeting a T-cell receptor complex protein (Goldstein, 1987; Leavy, 2010). After that, the US Food and Drug Administration (FDA) and the European Medicines Agency (EMA) approved more than 60 mAbs to not only treat disease like asthma and cancer that impacted millions of patients, but also treat orphan diseases with fewer patients (Borrebaeck and Carlsson, 2001; Ecker *et al.*, 2015). While mAbs can be used for broader targets, oncology and hematology remain the most prevalent medical applications (Grilo and Mantalaris, 2019). mAbs occupy a significant portion of the biopharmaceutical market. Past market data (2012–2017) indicated a doubling of the mAb market, a trend that is anticipated to continue to 2022 when mAb sales are expected to reach US$130–200 billion driven by a healthy pipeline, increasing roles for biosimilar and emerging economies (Chames *et al.*, 2009; Ecker *et al.*, 2015; Grilo and Mantalaris, 2019).

Immunoglobulins can be divided into five classes including α, δ, ε, μ, and γ immunoglobulins. Currently, all the mAbs in the market belong to one of the subclasses, gamma-immunoglobulin (IgG). IgG comprises two heavy chains (H, 50 kDa) and two light chains (L, 25 kDa) connected by disulfide bonds shown in Figure 1.1. The light chains contain one constant domain (C_L) and

one variable domain (V_L). The heavy chains contain three constant domains (C_H) and one

variable domain (V_H). The variable regions mediate antigen binding properties and the constant

regions interact with effector cells or molecules. Therefore, mAb structure can also be described

as fragment antigen binding (Fab) region and fragment crystallizable (Fc) domain. In addition to

naked antibodies, other therapeutic modalities based on the generic antibody molecule have been

gaining momentum in recent years (Almagro *et al.*, 2018). Those novel mAb modalities

including Fc-fusion proteins (Czajkowsky *et al.*, 2012), antibody-drug conjugates (ADC) (Beck

et al., 2017) and bispecific antibodies, (Brinkmann and Kontermann, 2017; Grilo and Mantalaris,

2019) have fueled the clinical development of more treatments.
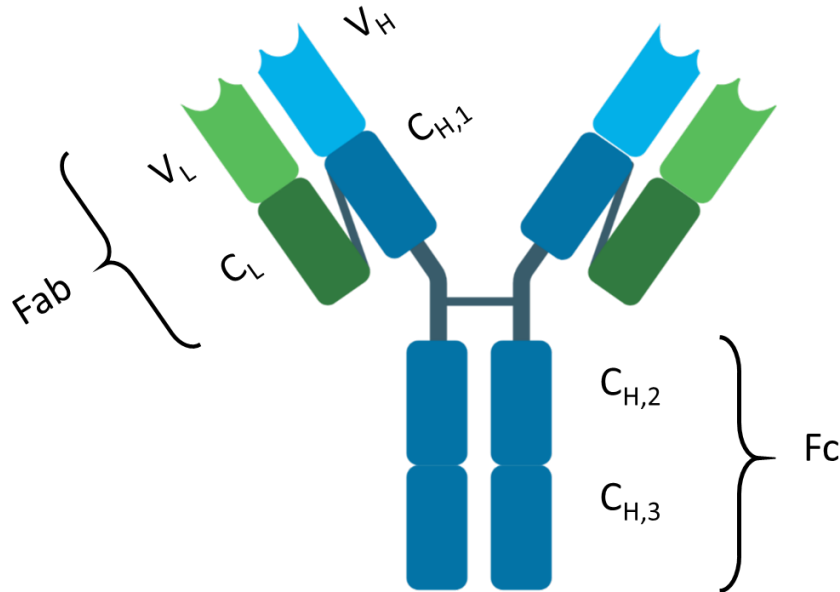
Figure 1.1. An illustration of the immunoglobulin G (IgG) structure. One IgG contains pairs of heavy chains (blue) and light chains (green). One heavy chain includes a variable domain (V_H) and three constant domains ($C_{H,1}$, $C_{H,2}$ and $C_{H,3}$) and one light chain includes a variable domain (V_L) and a constant domain (C_L)

The efficacy of therapeutic antibodies stems from various mode of actions (MOAs) shown in Figure 1.2. Most antibodies interact with components of the immune system through antibody-dependent cell-mediated cytotoxicity (ADCC) and complement-dependent cytotoxicity (CDC). Moreover, antibodies can neutralize the cell signaling pathway or work as drug delivery carriers (Almagro *et al.*, 2018; Buss *et al.*, 2012; Chames *et al.*, 2009). To trigger ADCC, antibodies first have to bind to the target cells through the Fab region and then recruit immune-effector cells that express receptors able to bind to the Fc region, and thus activate the immune-effector cells (such as NK cells) to respond or directly lyse the target cells. Similar to ADCC, CDC activity triggers the lysis of the target cell by initiating the complement system through the complement component 1q (C1q) protein. Additionally, many antibodies can utilize neutralization to block the pathophysiological function of their target molecules. In this case, antibodies bind to the ligand or receptor and block the target signaling pathway, resulting in the cellular activity being lost, proliferation being inhibited, and apoptotic programs being activated (Buss *et al.*, 2012; Zafir-Lavie *et al.*, 2007). In addition, antibodies can be applied as drug delivery carriers to directly kill the target cell when conjugated with radioisotopes, toxins, drugs or cytokines (Beck *et al.*, 2017; Zafir-Lavie *et al.*, 2007).
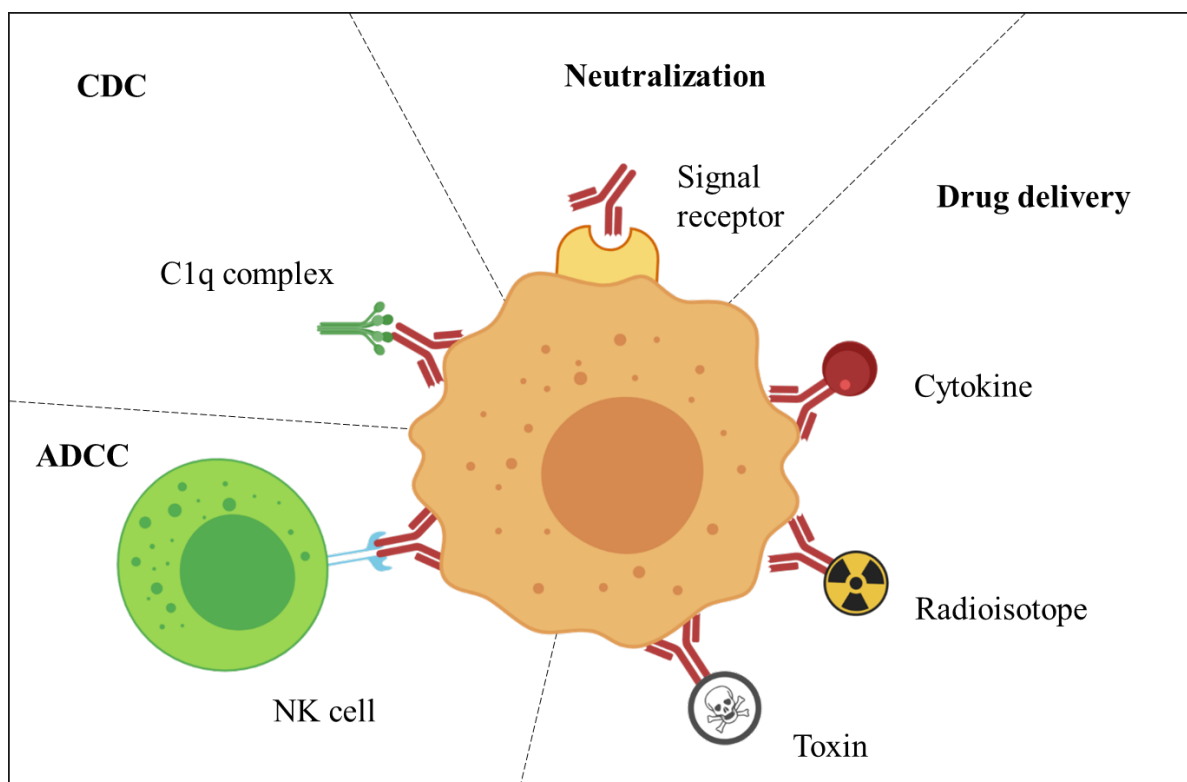
Figure 1.2. An illustration of different modes of action of antibodies.

1.1.2 Downstream process for monoclonal antibodies

Efficient purification is a critical step in the manufacturing process. The purification of mAbs requires a cascade of unit operations such as milling, mixing, filtration and sterilization. A generic process that could be employed for all kinds of mAb is desired in manufacturing. The generic process or a so-called platform can shorten the development time as process development can often be the rate-limiting step in the introduction of new therapeutics into clinical trials (Shukla *et al.*, 2007). Furthermore, a versatile platform can continuously and radically reduce the cost, labor and resources. A standard process has been agreed upon by the major biopharmaceutical cooperation shown in Figure 1.3. Among those steps, the key operation is the chromatographic process. Chromatography is a powerful separation method stems from the need for separation and identification chemical components of a complex mixture. Later,

chromatography is recognized by the pharmaceutical industry since it is the only general separation method that can reach such a high purity for the pharmaceuticals. Thereafter, chromatography is not only used for analytical purpose but also material preparation.

Most of the platform have involved the use of Protein A affinity chromatography as the first step to capture mAbs from cell culture by means of the high affinity between the Protein A resin and the Fc region of mAbs. Other modes of chromatography have been combined with Protein A as polish steps to achieve a higher purity level by reducing host cell protein impurities, high molecular weight aggregates, low molecular weight clipped species, DNA and leached Protein A (Almagro *et al.*, 2018; Lu *et al.*, 2009; Marichal-Gallardo and Álvarez, 2012; Musante *et al.*, 2013).

Primary recovery (Centrifugation)
↓
Capture (Protein A)
↓
Viral removal (Filtration/pH adjustment)
↓
Polishing (CEX/AEX/HIC/MMC)
↓
Viral removal (Filtration)
↓
Filling (UF/DF)
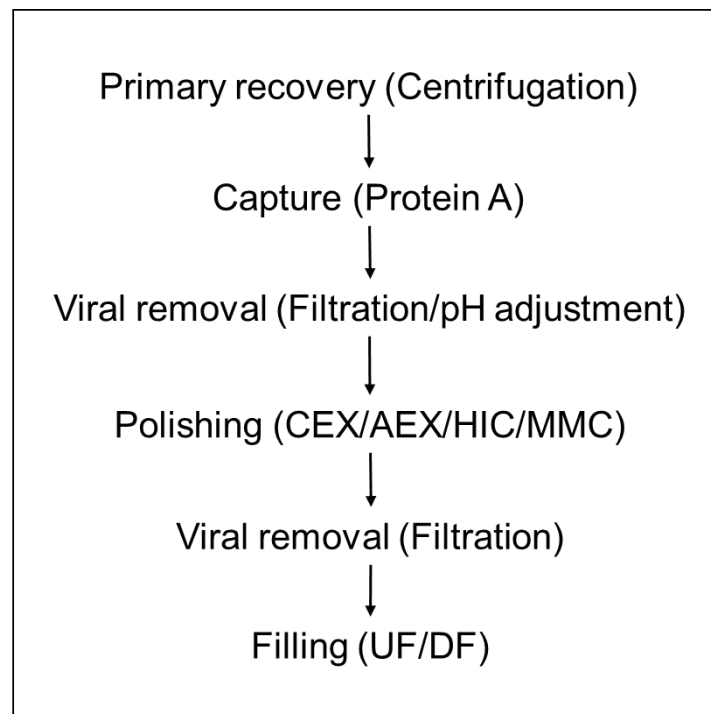
Figure 1.3 A simplified downstream process. (Hanke and Ottens, 2014)

During manufacturing, a mAb is exposed to various kinds of stress which can introduce unwanted aggregates. There are several chances for protein to form aggregates during cell culture. For example, accumulation of high amount of protein during expression may lead to intracellular aggregation (Schröder *et al.*, 2002; Zhang *et al.*, 2004). Secreted proteins also experience mechanical stresses such as stirring and turnover in the gas/liquid interface, which introduces more aggregates (Dengl *et al.*, 2013; Nakanishi *et al.*, 2001). After that, protein products have to go through even more unfavorable conditions during the purification steps. For example, both Protein A elution and viral clearance require low pH environments that have been known as a key factor causing the protein conformational change (Arosio *et al.*, 2013; Mason *et al.*, 2012; Mazzer *et al.*, 2015). In polish chromatography, step elution inevitably concentrates proteins, which also increases the aggregation tendency (Sukumar *et al.*, 2004). Freezing, dehydration and mechanical forces introduced by pumping, agitation and filtration are also common causes for aggregate generations (Abbas *et al.*, 2012; Kiese *et al.*, 2012; Bee *et al.*, 2010; Ferri *et al.*, 2002; Nakanishi *et al.*, 2001).

It is critical to remove aggregates as they generally reduce efficacy and most importantly cause several immunogenic effects due to the multiplicity of epitopes (Cromwell *et al.*, 2006). However, there is no clear restriction on the maximum allowable aggregate levels in biopharmaceutical products currently. Given the lack of information regarding clinical relevance, many specifications are narrowed down to unnecessary levels, based on previous manufacturing processes (Kozlowski and Swann, 2006).

As reviewed by Manning *et al.* (2010), protein aggregates can be classified as various types, such as reversible non-covalent oligomers, irreversible non-covalent oligomer, covalent oligomers and large aggregates (>10 -mer), through different association mechanisms including the association

6

of native monomer, aggregation of conformationally altered monomer, aggregation of chemically-modified monomer, nucleation-controlled aggregation and surface-induced aggregation. Due to the complicated aggregate formation mechanism and the lack of efficient methods to identify the aggregate type, most of the separation relied on empirical design to remove aggregate. Most of the aggregates can be removed in a polish chromatographic step after the Protein A capture step as shown in Figure 1.3, where separations are achieved by exploiting the differences in their physical properties, such as hydrophobicity, surface charge and size. The current polish step involves hydrophobic interaction chromatography (HIC), multimodal chromatography (MMC), cation exchange (CEX) and anion exchange (AEX) chromatography. Separation using HIC and CEX are discussed by many authors. However, there are always drawbacks related to those applications. For example, Kramarczyk *et al*. (2008) evaluated eight HIC resins combined with six buffers for their ability to purify a mAb using a high-throughput (HTS) system. The results indicate that the aggregates bind stronger to HIC resin compared to the monomer and the Phenyl Toyopearl 750 M resin with citrate buffer had the highest separation performance of all tested resins and conditions. However, HTS screening is conducted by tiny robot columns which cannot represent the column behavior in large scale so that the results are not comparable with most of the practical cases. Kumar and Rathore (2014) successfully removed the HMW species of a mAb with 95% recovery, however, using a CEX column combined with Capto Phenyl column or Sartobind Phenyl membrane. The added column/membrane polish step is undesired since it would decrease the separation efficiency as well as increase the cost of labor and facility. McCue *et al*. (2008) used a Phenyl Sepharose 6 Fast Flow to purify a recombinant fusion protein resulting in less than 3% aggregate in the final

product pool. However, the author also observed protein monomer irreversibly bound to this HIC adsorbent, reducing the yield from this purification step (McCue *et al.*, 2009).

1.1.3 Chromatography modalities

In addition to testing different adsorbents, different modes of operation are also applied to purify protein therapeutics. A commonly used chromatographic modality is bind-wash-elute chromatography (Asenjo and Andrews, 2009; Kozlowski and Swann, 2006). Figure 1.4 shows the basic features of bind-wash-elute chromatography for a separation example of a monomer (M) and dimer (D) mixture. In this example, the elution phase is operated with a linearly changing gradient (LGE) in mobile phase composition which is also referred to linear gradient elution chromatography. In the beginning, a certain amount of feed corresponding to a fraction of the column binding capacity is first loaded. If needed, the column is then washed with pure buffer to remove unbound or weakly bound impurities. The mixture is then eluted with a gradient in mobile phase composition that gradually decreases the binding strength. In industry, instead of gradient elution, isocratic elution or step elution are frequently used, where one or several pre-selected elution buffers are applied. Although isocratic or step elution are easy to operate, they cannot provide high productivity or high resolution for complicated systems (Felinger and Guiochon, 1998; Gallant *et al.*, 1996).

Attention regarding another chromatographic modality, frontal analysis (FA), has increased in recent years for protein separations. This interest stems in part from the fact that frontal analysis generally affords a higher utilization of the binding capacity compared to gradient elution, and in part because the separation can be conducted under isocratic conditions, thereby simplifying operations. Unlike bind-wash-elute mode, the mixture is loaded continuously until breakthrough of the more strongly adsorbed species (D) occurs, as seen in Figure 1.4. The weaker adsorbed

species (M) is recovered, ideally in pure form, between the pure component breakthrough front and the mixture breakthrough front. In this mode of operation, a binary mixture is continuously loaded to the column, resulting in two adsorption fronts – a fast moving front, corresponding to the weaker bound component, and a more slowly moving front corresponding to breakthrough of the more strongly bound component. Under ideal conditions, the weakly bound component is recovered in the column effluent between the first and the second front, while the more strongly bound component is held in the column and is recovered by elution together with any of the weakly bound components. If more than two components are present with greater binding strength, each of the more strongly bound species accumulates in the column and is removed during the elution step. Application of frontal analysis to antibody purification has been demonstrated by several authors using cation exchange resins for the separation of antibody charge variants (Tao *et al.*, 2012), and antibody monomer-dimer mixtures (Reck *et al.*, 2017), using anion exchange resins and adsorptive membranes for the separation of albumin monomer and aggregates (Hunter and Carta, 2001; Weinbrennef and Etzel, 1994). Although described with different terms such as "overload chromatography" (Liu *et al.*, 2011; Stone *et al.*, 2019) and "flow-through chromatography" (Wollacott *et al.*, 2015), frontal analysis has also been used to separate antibodies from aggregates and other impurities using either resins or adsorptive membranes. In general, the optimization of frontal analysis requires heavy experimental approaches or column simulation, since the selectivity of frontal analysis is highly dependent on operating conditions such as residence time, ionic strength, load concentration and pH.
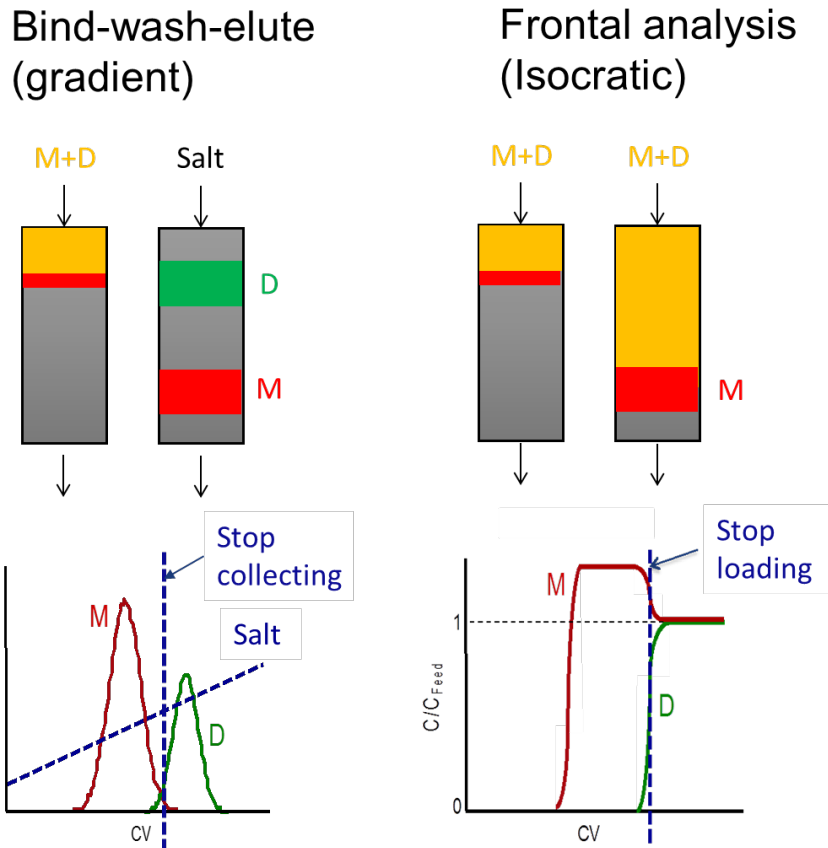
Figure 1.4. An illustration of frontal analysis and bind-wash-elute chromatographic modalities.

1.1.4 Chromatography modeling

Since separation design involves many parameters, the process is usually verified experimentally and the understanding of each parameter grasps from experiments. The design initially starts with changing one variable at a time which generates information on how this parameter influences the whole process. However, this approach may not be an exact representation of the real process since these results are impacted by a combination of parameters. Therefore, a simulation that sufficiently predicts protein separations over a broad range of operating conditions is necessary for rational process optimization. Additionally, the simulation work can serve to obtain the fundamental understanding of the interaction between proteins and chromatographic adsorbents.

As reviewed by Giddings (1991), the fundamental theory of chromatography utilize a chemical potential discontinuity in a direction perpendicular to that of convective transport. A typical chromatography column is a packed bed of spherical porous adsorbent medium as shown Figure 1.5. In most of the cases, flow is absent within the intra-particle pores. Inside of the adsorbents, the chemical potential discontinuity establishes some degree of separation of the sample components. Meanwhile, this separation is amplified by the flow of the mobile phase in the column axial direction, which is perpendicular to that discontinuous gradient (Guiochon, 2002). Therefore, the nature of chromatography requires both a mass balance of the solute in a slice of column and mass transfer kinetics in the column. Most of the chromatographic models are composed of a set of partial differential equations including: a rate equation to describe protein adsorption in spherical adsorbents, an adsorption equilibrium equation to describe the distribution of protein on the adsorbed phase versus the liquid phase and a conservation equation to describe the column dynamics. To build a reliable model, many transport and kinetic resistances need to be considered, such as external mass transfer, kinetic resistance to binding, pore diffusion and solid diffusion as shown in Figure 1.5C.

Historical attempts toward chromatographic modeling have demonstrated the validity of several models. In order of increasing complexity, these models includes the ideal model, lumped kinetic model, pore model and general rate model. The ideal model or the so-called local equilibrium model is the simplest model, as it assumes that the column has infinite efficiency. Thus, the band profile is only dependent on the equilibrium thermodynamics and appears as a sharp peak. On the other hand, the general rate model (GRM) describes the detailed mechanisms associated with all the possible resistances discussed previously (von Lieres and Andersson, 2010). Although the GRM model covers a comprehensive mechanism of molecular interaction and transport, practical

11

application is often hindered by computational complexity. To overcome this problem, lumped diffusion (Morbidelli *et al.*, 1982) or linear driving force (LDF) models (Glueckauf, 1955), which simplify the calculation by reducing the unknown parameters, are currently heavily used in this field. Furthermore, due to the heterogeneity of mAbs, different thermodynamic isotherm models have also been utilized including the Langmuir model, stoichiometric displacement (SD) model, steric mass action (SMA) model and colloidal model (Guélat *et al.*, 2012; Oberholzer and Lenhoff, 1999).

Many attempts have been made in modelling the chromatographic behavior of multicomponent system (Creasy *et al.*, 2018; Guélat *et al.*, 2012; McCue *et al.*, 2008; Zenhäusern and Rippin, 1998; Zhang *et al.*, 2019). For example, Sejergaard *et al.* (2014) demonstrated that the SMA model is capable of accurately describing the chromatographic separation of a modified human growth hormone and its aggregate on a multimodal Capto adhere resin. However, human growth hormone is a relatively small molecule lacking a high mass transfer resistance compared to mAbs. Borg *et al.* (2014) modeled multicomponent elution on CEX using GRM and SMA models for both low load and high load conditions. The result shows that the SMA model can predict protein behavior in the low load range, while the high load behavior is not well predicted by this model. Kluters *et al.* (2016) developed a modified SMA model to describe the pH gradient elution in mAb aggregate separation. In this case, the impact of pH was represented by the effective charge change in the SMA model. However, these authors did not evaluate the high protein load condition.
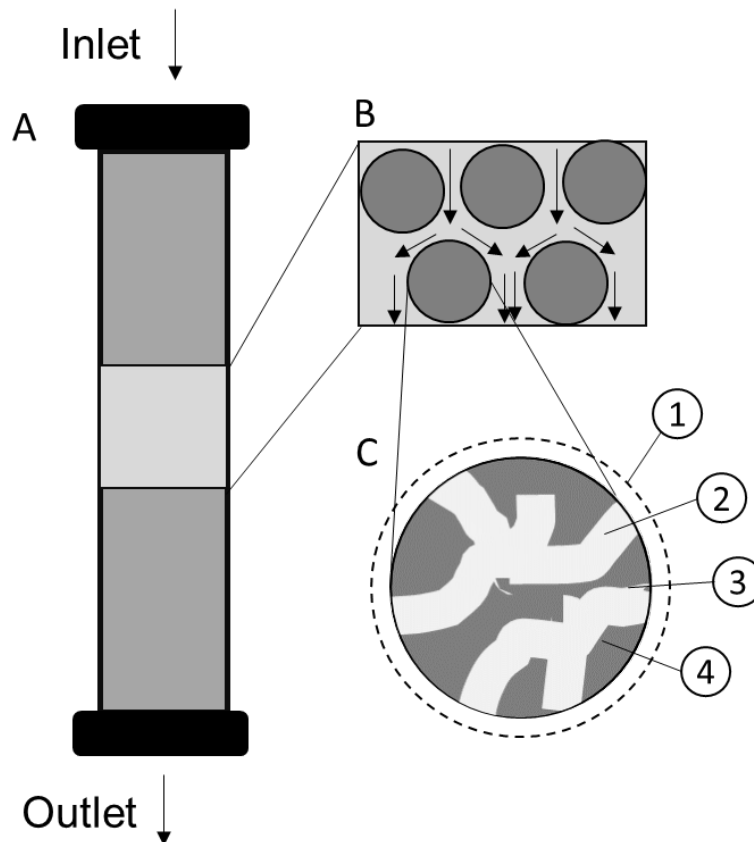
Figure 1.5. An illustration of the important resistance included in the general rate model (GRM) of column chromatography. A. Packed bed. B. Molecules transported through the interstitial bulk volume between the chromatography beads by convective flow. C. Other transport and kinetics resistances to protein adsorption in porous particles. (1) External mass transfer; (2) pore diffusion; (3) kinetic resistance to binding and (4) solid phase diffusion. (Carta and Jungbauer, 2010)

1.1.5 Hydroxyapatite

Hydroxyapatite (HAP) is among the earliest chromatographic materials, first applied by Tiselius (Tiselius *et al.*, 1956) in 1956 to purify biomolecules. HAP is a microcrystalline phase with bulk formula $Ca_5(PO_4)_3OH$. Proteins adsorb on HAP by interacting with different binding sites on the crystal surface (Gorbunoff, 1984a, 1984b; Gorbunoff and Timasheff, 1984; Kawasaki *et al.*, 1990). As reviewed by Cummings *et al.* (2009) , basic proteins, containing a predominance of lysine, arginine, and histidine residues, are generally thought to interact primarily with

negatively-charged phosphate groups ("P-sites") on the crystal surface, while acidic proteins, containing a predominance of acidic residues, are thought to interact primarily with positively-charged calcium ions ("C-sites") also present on the crystal surface (Gagnon *et al.*, 2009; Gorbunoff, 1984a, 1984b; Kawasaki, 1991; Schubert and Freitag, 2009). In practical applications, P-site interactions are typically modulated using non-binding salts, such as NaCl, that screen electrostatics, while C-site interactions are typically modulated with binding or displacing salts, such as sodium phosphate, that interact with the surface calcium ions. Of course, multimodal interactions on both P- and C-sites are also possible and are thought to result in unique selectivity (Boschetti and Jungbauer, 2000; Horenstein *et al.*, 2003; Jungabauer *et al.*, 1989; Jungbauer *et al.*, 2004).

While the earliest microcrystalline HAP materials were friable and difficult to pack in columns, the more recent commercial availability of spherical, ceramic-hydroxyapatite (CHT) particles has greatly expanded the range of practical applications. Spherical particles suitable for protein chromatography are obtained by spray-drying HAP nanocrystals to obtain porous particles with sizes useful for process scale applications (20-80 μm) (Cummings *et al.*, 2009). After spray drying, the particles are sintered at high temperature to stabilize the structure and attain mechanical stability. Since the sintering temperature also affects porosity and pore size, different CHT types are available with properties that are optimized for different applications. Agarose-HAP composites, where HAP crystals are embedded in spherical agarose beads are also commercially available as described for example in refs. (Fargues *et al.*, 1998; Milligan *et al.*, 1987).

Many different process applications of HAP have been described, including, to cite just a few examples, the separation of DNA and RNA of different sizes (Giovannini and Freitag, 2000;

Hori *et al.*, 1990; Watanabe *et al.*, 1999), the isolation of plasmid DNA (Giovannini and Freitag, 2002; Schmoeger *et al.*, 2010; Shi *et al.*, 2007), the purification of various enzymes (Cummings *et al.*, 2009), the purification of virus-like particles produced in recombinant yeast (Cook *et al.*, 1999), the isolation of immunoglobulins from plasma fractions (Stanker and Vanderlaan, 1985) and monoclonal antibodies from cell culture supernatants (Giovannini and Freitag, 2000; Jungbauer *et al.*, 1989; Luellau *et al.*, 1998; Saito *et al.*, 2012; Stanker *et al.*, 1985), the removal of aggregates from single-chain antibodies (scFV) and from full-length monoclonal antibodies (Gagnon, 2008; Gagnon *et al.*, 2006; Sun *et al.*, 2016), the separation of antibody charge variants (Saito *et al.*, 2016), and the separation of different molecular forms of recombinant IgA and IgM products (Aoyama and Chiba, 1993).

However, despite the widespread use of HAP, in general, and of CHT, in particular, only a handful of studies have been published on the characterization and modeling of protein adsorption equilibrium and kinetics in materials for chromatographic applications especially at high protein loads and for multicomponent systems. As a result, the development and design of chromatographic separations using CHT remains largely empirical. Giovannini and Freitag (2000) measured binding capacity for different CHT types and found it to be correlated with chromatographic performance for plasmid and antibody purification. Fargues *et al.* (1998) published a detailed study on the adsorption of bovine serum albumin and hemoglobin on an agarose-HAP composite both as individual components and as mixtures. They found that adsorption of these two proteins was mass-transfer controlled and used a solid diffusion model to describe their adsorption kinetics. Competitive binding of the two proteins was also demonstrated and was also be described by a solid diffusion model albeit with diffusion coefficients that were very different from those used to describe single-component binding.

15

Unfortunately, other transport models, including pore diffusion, which would likely have been a more physically realistic representation of the actual process, were not used. Moreover, because the particle structure is completely different, the results of Fargues *et al.* are not applicable to CHT. Finally, Jungbauer *et al.* (1989) reported a detailed study on the adsorption of IgG on "nanophased" porous hydroxyapatite particles in comparison with commercial CHT media. These authors reported adsorption isotherms, dynamic binding capacities (DBC), and elution profiles for IgG and concluded that particle size had a strong influence on the effect of flow rate on the DBC. The authors showed that their 30 μm diameter nanophased HAP particles eliminated pore diffusion resistance giving velocity-independent DBC.

1.2 Motivations and goals

As summarized above, only limited data are currently available in the literature on protein adsorption on CHT for multicomponent systems, particularly for antibody monomer-dimer mixtures. Additionally, an accurate quantitative model has not been presented thus far to describe the dynamics of single and two-component adsorption in these systems.

Therefore, the goals of this dissertation are:

(1) Characterizing the structural properties of CHT Type I and Type II and deriving the relationship between the physical properties with the adsorption performance by comparing CHT Type I and Type II;

(2) Understanding the competitive binding of monoclonal antibody on CHT particles and investigating the buffer effect of salt concentration and salt type, as well as explaining the results with suitable multi-component isotherm model;

(3) Establishing experimentally the feasibility of implementing frontal analysis-based and gradient elution-based separations of mAb monomer-dimer mixtures

(4) Developing a spreading rate model and extending the EI model to describe the diffusion and competitive binding of the two-component system; and

(5) Comparing frontal analysis and gradient elution chromatography for mAb monomer-dimer separation at high protein load conditions and providing an optimization strategy for a practical separation using CHT.

Chapter 2 Structure Characterization of Ceramic Hydroxyapatite Type I and Type II

2.1 Introduction

As a chromatographic medium, ceramic hydroxyapatite (CHT) consists of hydroxyapatite (HAP) nanocrystals with bulk formula $Ca_5(PO_4)_3OH$ that are spray dried and then sintered at high temperature to obtain nearly spherical macroporous beads with high mechanical stability. The sintering temperature is known to affect the crystal morphology and, thus, pore size as well as available surface area (Malina *et al.*, 2013; Ramirez-gutierrez *et al.*, 2017). Different types of CHT are commercially available and are usually classified according to these properties. Understanding the physical properties of chromatographic adsorbent is very important in process optimization and mechanistic model development as well as in improving future adsorbent design.

Particle size is a critical factor that affects the performance of liquid chromatography, especially in column resolution and dynamic binding capacity (DBC). As particle size decreases, the resolution improves but the DBC decreases. For example, the particle size of adsorbents used for analytical purposes is normally smaller than 10 μm, but that of adsorbents used for material preparation is typically between 30 to 100 μm (Carta and Jungbauer, 2010). It is important to understand not only the average particle size, but also the particle size distribution. A broad distribution would increase the column pressure as well as reduce the packing quality.

Another important physical property is intra-particle porosity, which could vary widely depending on the particle structure. For example, it can be above 90% for gel structure adsorbents such as agarose and cross-linked dextran or it can be near 0% for the pellicular stationary phase (Carta and Jungbauer, 2010). Since adsorption kinetics of large

biopharmaceuticals for preparative chromatography are commonly controlled by intraparticle diffusion, increasing pore size increase the particle performance by reducing diffusion hindrance. On the other hand, larger pore size leads to smaller surface area and less binding capacity. It is necessary to choose the adsorbent with an appropriate pore size based on the objective of the process.

The goal of this chapter is to elucidate the structure of CHT particles. We chose two types of CHT to conduct this study, CHT Type I and Type II (Bio-Rad Laboratories, Hercules, CA, USA), which are chemically identical to each other but obtained at different sintering temperatures and, thus, have different pore sizes, in order to relate structure to protein adsorption properties. Particle size is observed directly under the microscope and analyzed by Image J. The intraparticle morphology of internal pore structure are characterized by transmission electron microscopy (TEM). Pore size is determined from both nitrogen adsorption and inverse size exclusion chromatography. The former method calculates the surface area by analyzing the amount of nitrogen adsorbed by the solid surface with different pressure. The latter is based on the chromatographic retention of non-interacted solutes of known size.

2.2 Materials

Samples of CHT Type I and Type II with 40 μm nominal particle size were obtained from Bio-Rad Laboratories (Hercules, CA, USA). Chemicals used in buffer separation were obtained from Thermo Fisher Scientific (Waltham, MA, USA) and MilliporeSigma (St. Louis, MO, USA).

2.3 Methods

2.3.1 Transmission electron microscopy

Transmission electron microscopy (TEM) was used to image the internal structure of the CHT particles. For this purpose, the CHT particles were first washed with ethanol-water mixtures with increasing ethanol concentration from 0 to 100%, saturated with the acrylic resin LR White (London Resin Company, London, UK), and finally incubated at 45°C overnight to set the resin. The solidified samples were then ultra-microtomed into 80 nm sections by diamond knife and imaged with a JEOL JEM-1230 transmission electron microscope.

2.3.2 Inverse size exclusion chromatography

The intraparticle porosity and apparent pore size were obtained by inverse size exclusion chromatography (iSEC) according to the method described by Hagel *et al.* (1996) but using polyethylene glycol (PEG) probes with molecular mass between 0.3 and 100 kDa obtained from MilliporeSigma (St. Louis, MO, USA) instead of dextran probes since the latter were found to interact with CHT. PEG samples up to 35 kDa were used as received from the supplier, while the 100 kDa sample was purified by SEC with a Superdex 200 Increase 10/300 GL column to remove lower molecular mass species. The iSEC experiments were conducted with particles packed according to the CHT manufacturer instructions into 1 cm diameter × 10 cm long Tricorn 10/100 columns (GE Healthcare, Pittsburg, PA, USA) at 5 mL/min to a final bed volume V_C =6.6±0.2 mL. The packing quality was determined from an acetone pulse injection, which gave reduced HETP and asymmetry factors of 3.9 and 1.1, respectively, for the CHT Type I column and 3.0 and 1.2, respectively, for the CHT Type II column. 10 µL injections of 5 g/L of each PEG probe in 250 mM NaCl, 5 mM Na_2HPO_4 at pH 7 were made using a Waters HPLC system with a Model 2414 refractive index detector (Waters, Milford, MA, USA). The retention volume

at the peak maximum, V_R, was used to calculate the distribution coefficient of each PEG probe while the Carman-Kozeny equation was used to determine the extraparticle porosity, ε. The apparent pore radius, r_{pore}, and intraparticle porosity, ε_p, were then obtained by comparing the experimentally determined values of $K_D = (V_R/V_C - \varepsilon)/(1-\varepsilon)$ with the following equation, which assumes cylindrical pores with a uniform radius:

$$K_D = \varepsilon_p \left(1 - \frac{r_m}{r_{pore}}\right)^2 \qquad (2.1)$$

where r_m is the PEG radius. The latter was estimated from the correlation in (Fee and Van Alstine, 2004) based on the PEG molecular mass. Other models for K_D were also considered including a log-normal distribution of pore size as suggested, for example, by Yao and Lenhoff for other chromatographic adsorbents (Yao and Lenhoff, 2004). However, in our case, as also observed by others (Hagel *et al.*, 1996), we found that fitting our K_D data using a single pore size according to Eq. (2.1) or a log-normal distribution of pore sizes resulted in essentially the same quality of fit thereby preventing model discrimination. As a result, for simplicity we limited our analysis to Eq. (2.1).

2.3.3 Intraparticle surface characterization

The specific surface area was measured by N_2 sorption using a Micromeritics ASAP 2020 instrument (Micromeritics Inc., Norcross, GA, USA). The samples were evacuated for 600 min at 393 K prior to the N_2 sorption according to the Brunauer-Emmett-Teller (BET) model in the Micromeritics ASAP2020 software package (Sing, 1982).

2.4 Results and discussion

2.4.1 Particle size distribution

Both CHT Type I and CHT Type I samples with 40 μm nominal particle size were used in this work. The volume average particle size and distribution were obtained as prerequisite information for the following study since the size distribution will influence the adsorption rate. Figure 2.1 shows representative microphotographs and the volume average particle diameter distribution obtained in this work. As seen by optical microscopy, the particles are roughly spherical in both cases and the actual volume-average particle diameters and standard deviations for Type I and Type II are 39.9±10.4 μm and 41.3±9.9 μm, respectively, calculated from over 800 particles observed under microscope. The particle size distribution of each sample is also provided in Figure 2.1.
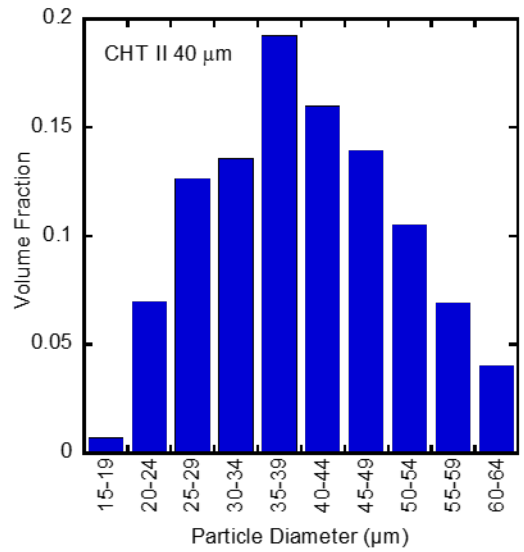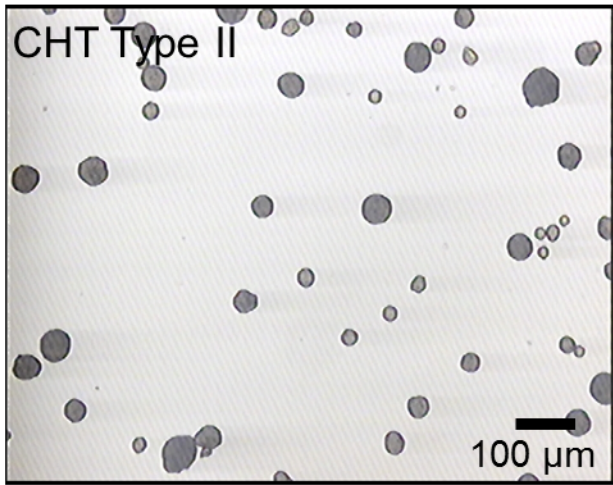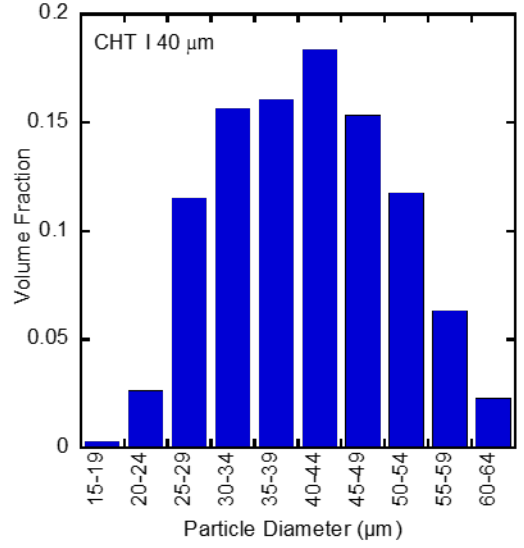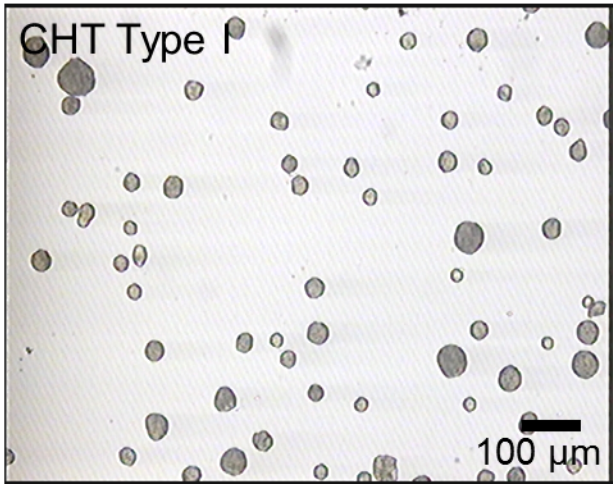
Figure 2.1. Representative particles under optical microscope (left) and particle size distributions (right) of CHT Type I (top) and Type II (bottom) beads.

2.4.2 Intraparticle structure

Figure 2.2 shows representative TEM images of CHT particles at low (a, c) and high (b, d) magnification for both CHT Type I and Type II. In these images, the gray areas are the embedding LR White resin while the dark features are the CHT crystals. The white spots are defects due to the sectioning and/or incomplete infiltration of the embedding resin. At lower magnification (Figure 2.2a, c), it can be seen that the hydroxyapatite crystals are distributed fairly evenly throughout the particle. The HAP nanocrystals are easily discernible at the higher magnification (Figure 2.2b, d) for both CHT types. For Type I (a, b), the crystals appear acicular with size around 20x100 nm. For Type II (c, d), the crystals are more rounded with size up to about 200 nm. For both types, the crystals appear connected to each other at multiple points of contact. The pores, defined by the spaces between crystals, are up to 200 nm in size for Type I and up to 300 nm for Type II.
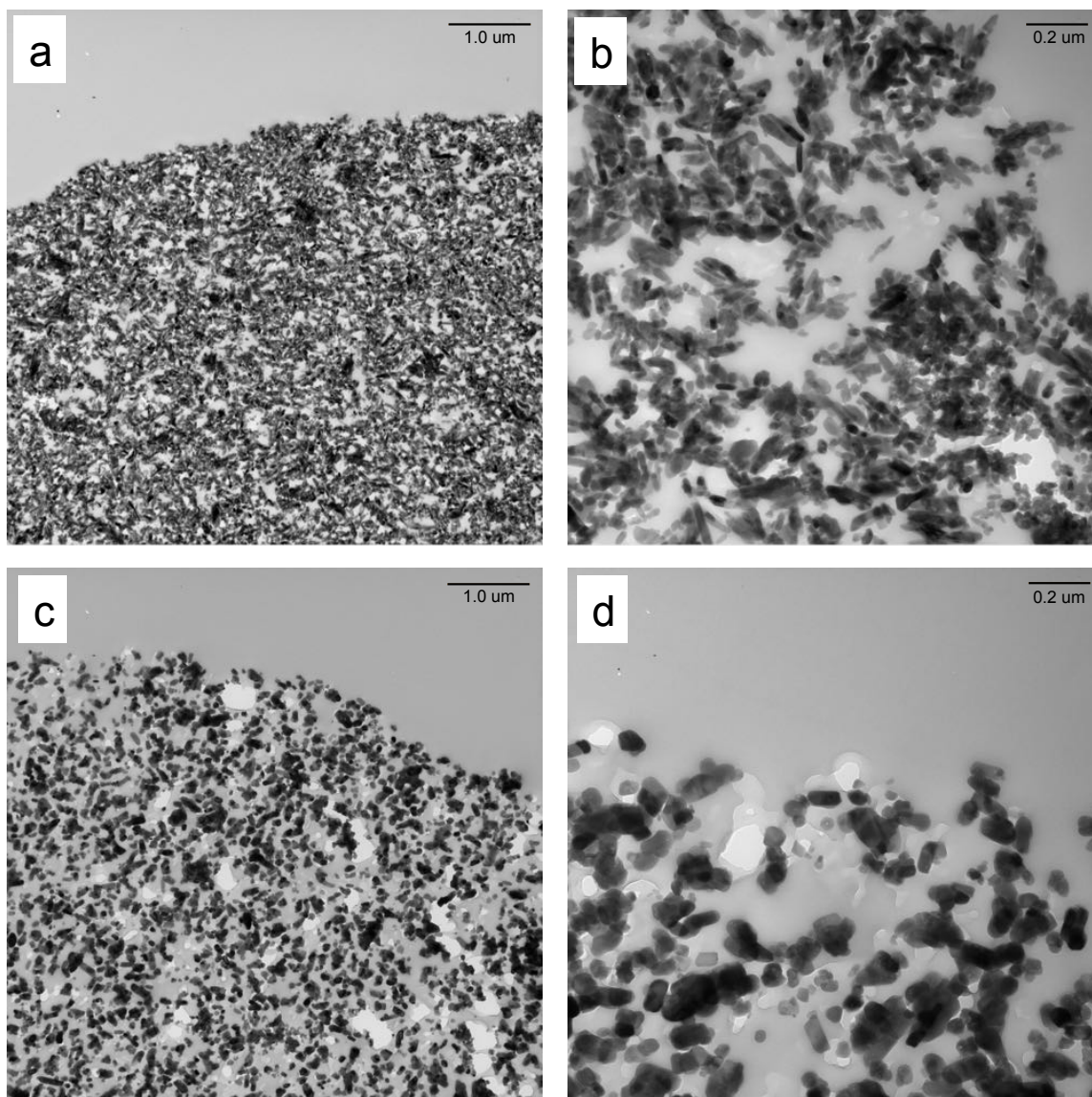
Figure 2.2. TEM images of sections of CHT particles at 10,000X (a and c) and 40,000X (b and d). (a) and (b) are for CHT Type I and (c) and (d) are for CHT Type II.

2.4.3 Pore size characterization

The pore size and porosity of the CHT particles were obtained by inverse size exclusion chromatography (iSEC) using polyethylene glycol (PEG) probes with molecular weight between 300 and 100,000 Da as shown in Figure 2.3. Figure 2.4 shows the K_D-values for the PEG probes and for mAb monomer and dimer vs. their radius, r_m. The mAb results are discussed in the subsequence section. Table 2.1 shows the values of ε_p and r_{pore} determined by regression of the

25

PEG data according to Eq. (2.1). Other relevant properties, including the BET surface area and the surface area calculated from the iSEC PEG results as $AiSEC = 2\varepsilon_p / r_{pore}$, are also given. The BET and iSEC surface areas are comparable in magnitude but differ significantly. The differences stem in part from the fact that the iSEC-based area is based on a cylindrical-pore geometry, which is obviously only a rough approximation. On the other hand, both the BET and the iSEC-based measurements provide a similar ratio in the range 1.6-1.7 between the surface areas of Type I and that of Type II. As seen from these results, while intraparticle porosities are similar, the apparent pore size of CHT Type II based on the iSEC measurements is about 60% larger than that of Type I, suggesting that the latter could have faster mass transfer kinetics for large proteins. The surface area is, however, smaller for Type II compared to Type I, suggesting lower binding capacity as noted by Jungbauer *et al.* (2004) and Giovannini and Freitag (2002).
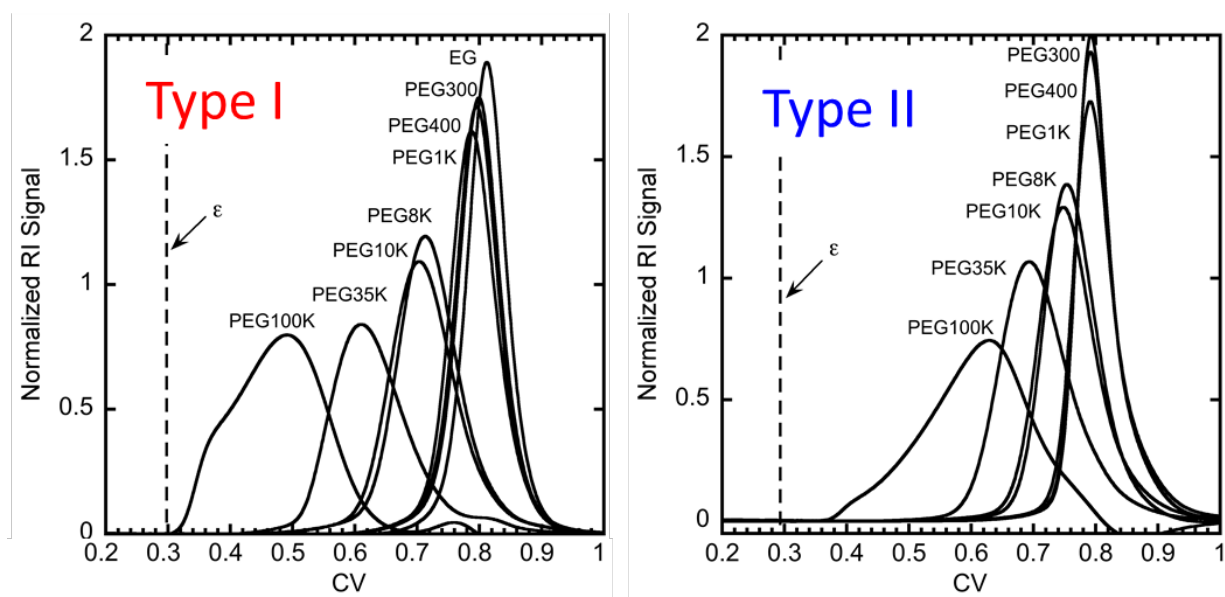
Figure 2.3. iSEC results for PEG pulse injection on CHT Type I and Type II in 250 mM NaCl 5 mM Na$_2$HPO$_4$ at pH 7.0.
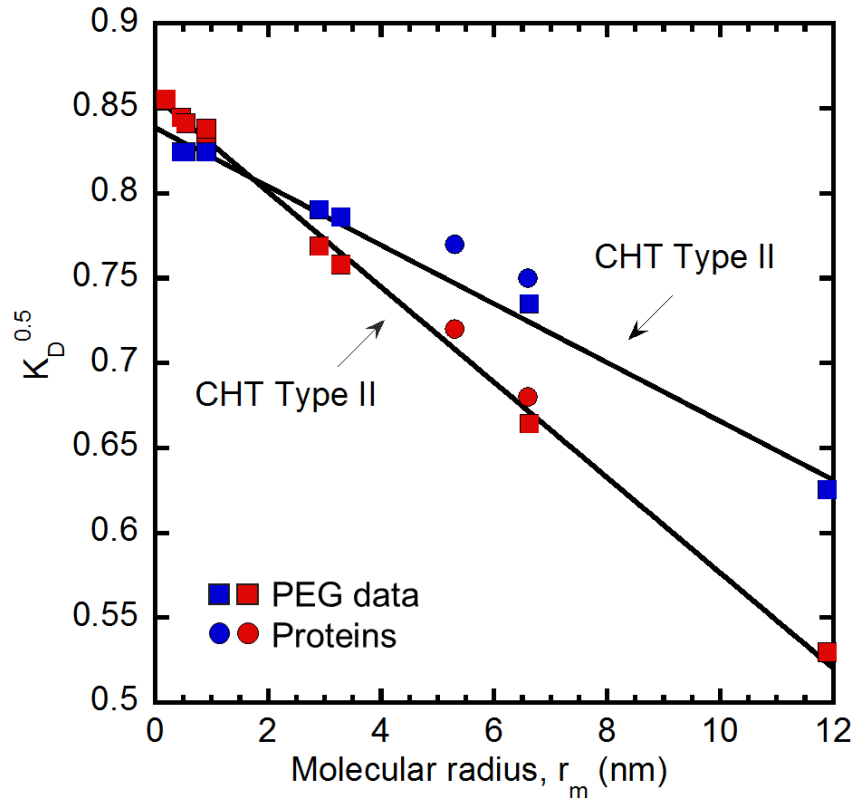
Figure 2.4. Distribution coefficient vs. molecular radius obtained from the iSEC measurements with PEG probes and with mAb monomer and dimer under non-binding conditions. Lines are based on Eq. (2.1) with parameters regressed to the PEG data.

2.4.4 Density

The density of hydrated CHT particles, used to convert mass-based adsorption measurements to a volume basis, was determined with a pycnometer. For this purpose, hydrated CHT particles were prepared as follows. First, particles were immersed in the loading buffer and then drained by centrifuging them at 10,000 rpm for 15 min in microcentrifuge filters to remove the liquid from the extraparticle space. Then the weight of hydrated particles was measured in pycnometer. The volume was calculated by replacing a water-filled pycnometer with hydrated particles and converting the displaced water volume into the hydrated CHT particle volume. The density obtained from the experimental measurement is 1.66 g/mL. This value can be compared with that obtained with the following equation:

27

$$\rho = \rho_{water}\varepsilon_p + \left(1 - \varepsilon_p\right)\rho_{HAP} \tag{2.2}$$

where the theoretical density of HAP (ρ_{HAP}), is 3.1 g/mL (Ratner *et al.*, 2009). The value of ρ

obtained from this equation is 1.60 g/mL based on the ε_p value obtained from the iSEC

experiments.

Table 2.1. Summary of physical properties of the CHT samples used in this work.

Property	CHT Type I	CHT Type II
Mean particle diameter and range, d_p (µm)	41.3	39.9
Hydrated particle density (g/mL)	1.63	1.66
Extraparticle porosity of packed column[a], ε	0.30	0.29
Intraparticle porosity[b], ε_p	0.73±0.01	0.70±0.01
Pore radius[b], r_{pore} (nm)	30±4	49±2
Surface area, A_{iSEC} (m²/mL particle)	48	30
Surface area, A_{BET} (m²/mL particle)	33	20

(a) based on column pressure drop and Carman-Kozeny equation
(b) based on iSEC with PEG probes

Chapter 3 Competitive Binding of Monoclonal Antibody Monomer-dimer Mixture on Ceramic Hydroxyapatite

3.1 Introduction

As summarized in the Chapter 1, only limited data are currently available in the literature on protein adsorption on ceramic hydroxyapatite (CHT) for multicomponent systems, particularly for antibody monomer-dimer mixtures. Additionally, an accurate quantitative model has not been presented thus far to describe the dynamics of single and two-component adsorption in these systems. The objective of this chapter is thus twofold. The first is to characterize and model the adsorption equilibrium and kinetics of a monoclonal antibody (mAb) in monomeric and dimeric forms and to relate the results to the internal structure of the CHT particles. The second is to measure and model the competitive adsorption equilibrium and kinetics of two-component binding for mAb monomer-dimer mixtures. In order to pursue these objectives, methodologies previously developed to study antibody adsorption in CEX resins are extended with appropriate modifications to CHT. The results are expected to be useful as a model to assess the ability of CHT to separate these mixtures at high protein loads.

3.2 Materials and methods

3.2.1 Materials

Samples of CHT Type I and Type II used in this chapter were as same as those discussed in Chapter 2. The mAb monomer-dimer mixture used in this work was provided by MedImmune (Gaithersburg, MD, USA) and is the same as that used by Reck *et al.* (2015, 2017) and by Creasy *et al.* (2018) for adsorption studies on a cation exchange resin. The pI is about 8.6 for both monomer and dimer (Reck *et al.*, 2015). The mixture, containing about 68% monomer and 32% aggregated species, was a sample enriched in soluble aggregates derived from a Protein A eluate. As shown by Reck *et al.* (2015), the aggregates species are predominantly dimers. Molecular

radii determined by size exclusion chromatography (SEC) with in-line dynamic light scattering (DLS) were 5.5 and 7.2 nm for the monomer and dimer peaks, respectively (Reck *et al.*, 2015). Isolated monomer and isolated dimer samples, each with purity >96% and >94% were obtained from the dimer-enriched sample by preparative SEC with a Superdex 200 Increase 10/300 GL column from GE Healthcare (Pittsburg, PA, USA) as described in Reck *et al.* (2015). Chemicals used in buffer separation were obtained from Thermo Fisher Scientific (Waltham, MA, USA) and MilliporeSigma (St. Louis, MO, USA).

3.2.2 Adsorption measurements

Adsorption isotherms were obtained by adding known weights of hydrated CHT particles in the range 20-40 mg that had been washed with the load buffer and spun in centrifugal microfilters to remove the extraparticle liquid to solutions with volumes in the range 0.5-1.0 mL having different initial protein concentrations contained in plastic tubes with different phosphate and NaCl concentrations. The ratio of particle to solution volumes was estimated to yield a ~50% drop from the initial protein concentration. The tubes were sealed and slowly rotated end-over-end on a wheel at room temperature. After 24 h, the CHT particles were settled by centrifugation at 10,000 rpm for 15 min and the supernatant concentration was determined with a Nanodrop 2000c UV–Vis spectrophotometer (Thermo Fisher Scientific, Wilmington, DE, USA) for single component measurements and by analytical SEC with a Waters Acquity BEH SEC 200 Å column (diameter × length = 4.6 mm × 150 mm, 1.7 μm particle size) and a Waters Acquity H-Class UPLC system (Milford, MA, USA) for mixture measurements. In either case, the adsorbed amount was calculated by material balance.

The stability of the monomer and dimer in solution during the 24 h incubation for the isotherm measurements was tested both by comparing the analytical SEC chromatograms before and after

24 h incubation and by dynamic light scattering. The results, shown in Figure 7.1 and Figure 7.2 and Table 7.1 of Appendix confirmed the stability of these solutions with and without the presence of the CHT particles.

3.2.3 Confocal laser scanning microscopy

Confocal laser scanning microscopy (CLSM) was used to image the intraparticle distribution of bound protein during transient adsorption using the isolated mAb monomer and dimer samples conjugated to Rhodamine Red and Rhodamine Green amine reactive dyes, respectively. The dyes were obtained from Life Technologies (Waltham, MA, USA) and conjugation was done as described in (Reck *et al.*, 2015). The degree of labeling (DOL) was 0.06 and 0.09 after conjugation for the monomer and dimer sample, respectively. Each conjugated sample was diluted with the corresponding native protein to attain a final DOL of 0.01. Batch CLSM experiments were done with the diluted conjugated protein samples in 5 mL tubes using an amount of CHT estimated to yield less than 10% drop of protein concentration in solution. Mixing was provided by rotating the tubes end-over-end at 30 rpm. At various times, samples were pipetted out and centrifuged at 13,000 rpm for 30 s to separate the particles from the supernatant using Spin-X microfiltration tubes (Corning Incorporated, Corning, NY). Since the refractive index of HAP is very high (n =1.63-1.64 according to (Holzmann *et al.*, 2009)), prior to imaging, the particles were immersed in benzyl alcohol (n = 1.54) to reduce the refractive index difference between the CHT and the solution. Figure 7.3 in Appendix provides optical microscope images of CHT particles in water and benzyl alcohol. The optical microscopy images of the CHT beads immersed in benzyl alcohol did not show any evidence of particles cracking or being otherwise disrupted. The time of exposure to benzyl alcohol was short (a few minutes) which helped ensure that the particles remained intact. CLSM images were obtained with a Zeiss

LSM 510 microscope with Plan-Neofluar 64X/1.3 NA oil objective (Carl Zeiss MicroImaging, LLC, Thornwood, NY, USA) as described in Reck *et al.* (2015). Images of the partially saturated particles taken at different times after immersion in benzyl alcohol were identical indicating that the method provides a reliable view of the intraparticle distribution of adsorbed protein during the transient adsorption process.

The digitized CLSM images were analyzed using MATLAB *imfindcircles* function with different sensitivity and edge threshold. This method provides an estimation of the equivalent circle radius of irregularly shaped beads using a circular Hough transform.

All adsorption measurements were conducted in phosphate buffers at pH 7 and at room temperature (22±2 ᵒC). This pH is sufficiently below the mAb isoelectric point (~8.6) that it is likely that the strong positive charge associated with these molecules suspended the interaction between carboxyl groups of mAbs and the C-sites of CHT adsorbent.

3.2.4 Chromatographic analysis for non-binding conditions

HETP measurements for non-binding conditions (500 mM Na_2HPO_4 at pH 7) were also made for the isolated monomer and dimer samples in the CHT columns using an AKTA Pure 25 system from GE Healthcare with UV detection at 280 nm. The results were analyzed by the moment method and used to calculate the distribution coefficient, K_D, of each protein in the CHT particles and the effective pore diffusivity, D_e, from the slope of the reduced HETP curve according to the following equation: (Carta *et al.*, 2005)

$$\frac{D_e}{D_0} = \frac{1}{30}\frac{\varepsilon}{1-\varepsilon}\left(\frac{k'}{1+k'}\right)^2\left(\frac{dh}{dv'}\right)^{-1} \qquad (3.1)$$

where D_0 is the free solution diffusivity (equal to 3.9x10^{-7} and 2.8x10^{-7} cm^2/s for the monomer

and dimer, respectively (Reck *et al.*, 2015)), $k' = (1-\varepsilon)K_D/\varepsilon$ is the protein retention factor,

$h = \mathrm{HETP} / d_p$, is the reduced HETP, and $v' = vd_p/D_0$ is the reduced velocity, with v being the

interstitial velocity.

3.3 Results and discussion

3.3.1 Adsorption equilibrium measurements

Figure 3.1 shows the adsorption isotherms for the mAb monomer and the mAb dimer on CHT

Type I and Type II at 20, 100, and 180 mM Na$^+$ concentrations with different combinations of

NaCl and phosphate. The *q*-values are given in mg per mL of particle volume. As seen in this

figure, in all cases protein adsorption decreases with the Na$^+$ concentration. However, data at 100

mM Na$^+$ obtained with either 50 mM disodium phosphate or with 10 mM disodium phosphate

with the addition of 80 mM NaCl show essentially the same isotherm for both monomer and

dimer and for both Type I and Type II. This result leads to the conclusion that both monomer and

dimer bind through a cation-exchange mechanism, which is modulated by the Na$^+$ concentration

and approximately independent of the phosphate concentration. At the same Na$^+$ concentration

more dimer is bound compared to monomer on a mass basis. Finally, it is evident that for each

condition more monomer and more dimer bind on Type I than on Type II, consistent with the

higher surface area of Type I. The solid lines in these figures are based on the Langmuir isotherm

model:

$$q = \frac{q_m K_L C}{1 + K_L C} \tag{3.2}$$

with parameter values fitted to the data and given in Table 3.1. The steric mass action (SMA)

model (Brooks and Cramer, 1992), which assumes a stoichiometric exchange of the protein for

same-charge counter-ions, was also considered. However, the SMA model did not improve the fit of the isotherm data compared to the simpler Langmuir model despite having more parameters. The Langmuir isotherm was found to fit the data within the experimental accuracy of the measurements. As seen from this table, at the lowest Na^+ concentration, the ratios of q_m-values for Type I and Type II are 1.67±0.17 and 1.66±0.42 for the monomer and dimer, respectively. These ratios are very close to the ratio of surface areas measured by iSEC (1.6-1.7) in Chapter 2 indicating that the nanocrystal surface is largely accessible by both molecules. Based on the maximum binding capacities observed for the monomer of 95 mg/mL for Type I and 55 mg/mL for Type II, specific protein binding capacities can be estimated based on the BET surface area to be 2.9 and 2.8 mg/m^2 for Type I and Type II, respectively. These values can be compared with the maximum binding capacities observed for IgG on a variety of saturated surfaces that generally fall in the range 2-5 mg/m^2 (Norde and Lyklema, 2012; Ortega-Vinuesa *et al.*, 1998; Xu *et al.*, 2006). Our values fall in the expected range for IgG-saturated surfaces suggesting that most of the surface area in the CHT is actually available for protein binding and that relatively high protein packing densities can be attained on the surface of the HAP crystals.
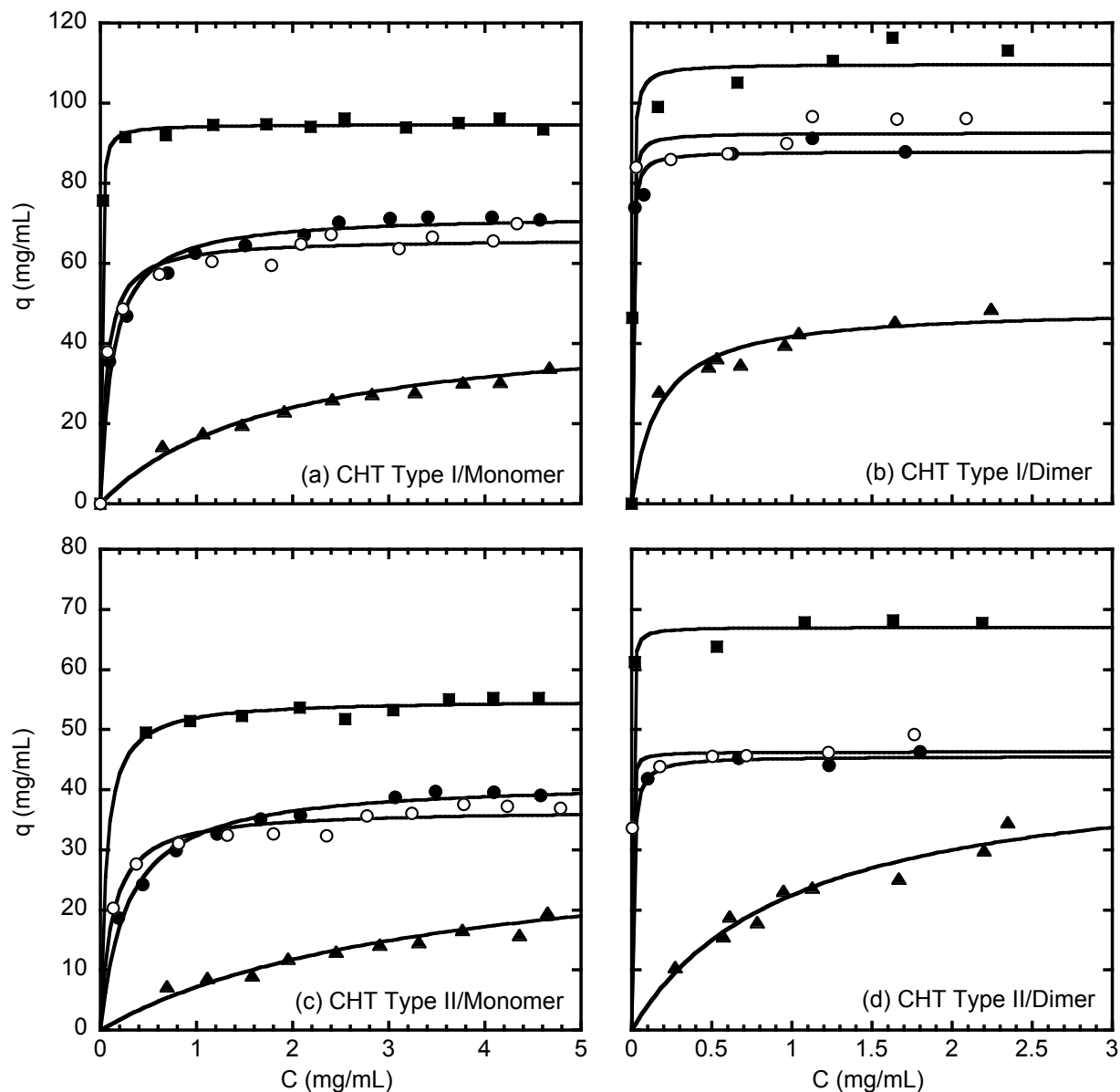
Figure 3.1. mAb monomer (a, c) and mAb dimer (b, d) adsorption isotherms on CHT Type I and Type II at different NaCl and phosphate concentrations with 20, 100, and 180 mM Na^+. All data are at pH 7 adjusted by adding phosphoric acid. ■: 10 mM Na_2HPO_4; ●: 10 mM Na_2HPO_4 + 80 mM NaCl; ○: 50 mM Na_2HPO_4; ▲: 10 mM Na_2HPO_4 + 160 mM NaCl. Solid lines are based on Eq. (3.2) with parameters in Table 3.1.

Table 3.1. Langmuir isotherm parameters fitted to the one component data in Figure 3.1 and to the binary data in Table 3.2. For each mobile phase composition, the top numbers are for CHT Type I and bottom numbers are for CHT Type II. q_m-values are in mg per mL of particle volume.

Buffer/System	mAb monomer		mAb dimer	
	q_m (mg/mL)	K_L (mL/mg)	q_m (mg/mL)	K_L (mL/mg)
10 mM Na$_2$HPO$_4$ One component data	94.7±0.4	156±11	110±2.0	240±50
	55.0±0.6	17.0±4.1	67.0±1.0	520±210
10 mM Na$_2$HPO$_4$ Binary data	94.7±0.4	65.6±11	110±2.0	230±50
	55.0±0.6	65.0±3.0	67.0±1.0	320±50
10 mM Na$_2$HPO$_4$ +80 mM NaCl One component data	72.2±1.1	7.91±1.0	87.9±2.3	230±82
	41.6±0.7	3.53±0.3	45.6±0.7	113±45
50 mM Na$_2$HPO$_4$ One component data	66.2±1.1	15.2±2.4	92.6±2.0	290±170
	36.7±0.7	8.33±1.3	46.3±0.8	520±110
10 mM Na$_2$HPO$_4$ +160 mM NaCl One component data	46.2±2.9	0.54±0.09	48.9±2.6	0.58±1.5
	32.3±4.7	0.29±0.08	45.1±4.6	0.99±0.23

Table 3.2 shows the binary adsorption equilibrium data obtained for monomer-dimer mixtures 10 mM Na$_2$HPO$_4$. As seen from this table, the dimer is preferred compared to the monomer for both Type I and Type II. However, the selectivity is slightly larger for the latter (average selectivity of 4.3 for Type I vs. 5.8 for Type II). The difference in selectivity is modest, however, likely because while the physical structure is affected by the sintering temperature the surface chemistry of the nanocrystals is the same. We conjecture that the slightly higher selectivity of Type II may be a result of modestly improved accessibility to the surface by the larger dimer

molecules afforded by the larger pores. Predictions of binary adsorption based on the two-component Langmuir isotherm (Ruthven, 1984):

$$q_i = \frac{q_{m,i} K_{L,i} C_i}{1 + K_{L,M} C_M + K_{L,D} C_D} \tag{3.3}$$

are also included in this table. Using the q_m and K_L values determined from the single component data resulted in poor predictions with an average absolute error of 46 and 35% for monomer and dimer, respectively, on Type I and of 78 and 39% for monomer and dimer, respectively, on Type II. These large errors occur, in part, because the single component isotherms are very steep resulting in a highly inaccurate determination of the K_L values. Fitting the K_L values to the binary data directly to Eq. (3.3), while keeping the same q_m-values determined form the single component data, resulted in much better agreement with an average absolute error of 11 and 14% for monomer and dimer, respectively, on Type I and of 24 and 6% for monomer and dimer, respectively, on Type II. q-values calculated with these parameters (also given in Table 3.1) are shown in Table 3.2. The multicomponent version of the steric mass action law model was also considered as an alternative to the multicomponent Langmuir isotherm. However, using parameters fitted to the single component isotherm data the predictive accuracy was not improved significantly compared with the simpler Langmuir model.

Table 3.2. Binary isotherm data for monomer-dimer mixtures in 10 mM Na_2HPO_4. All concentration are in mg/mL. q-values are given in mg per mL of particle volume.

Experimental data for CHT Type I					Predicted for CHT Type I		
C_M	C_D	q_M	q_D	$\alpha_{D,M}$	q_M	q_D	$\alpha_{D,M}$
0.56	0.29	34	89	5.1	34	70	4.0
1.3	0.79	30	68	3.7	30	74	4.0
2.6	0.36	50	45	6.6	64	35	4.0
3.0	2.0	35	68	3.0	29	76	4.0
4.4	1.2	51	57	4.1	48	54	4.0
4.6	2.1	42	61	3.2	37	67	4.0
Average ± stand. dev.				4.3±1.4			4.0
Experimental data for CHT Type II					Predicted for CHT Type II		
C_M	C_D	q_M	q_D	$\alpha_{D,M}$	q_M	q_D	$\alpha_{D,M}$
0.48	0.2	12	45	9.2	18	45	6.0
0.99	0.61	15	51	5.4	14	50	6.0
1.1	1.2	13	53	3.6	8.3	57	6.0
2.0	0.77	24	43	4.8	19	44	6.0
2.8	0.35	35	32	7.2	34	25	6.0
3.1	1.4	21	44	4.4	17	47	6.0
Average ± stand. dev.				5.8±2.1			6.0

3.3.2 Mass transfer

From a practical viewpoint, mass transfer is expected to be important under both binding conditions and non-binding conditions – the former determining transport during the load step of a bind and elute process and the latter during elution and during operation in a flow-through mode.

The mass transfer rates of the mAb monomer and mAb dimer under non-binding conditions were determined from pulse-response experiments. The peaks obtained at flow rates between 0.5 and 4.0 mL/min are shown in Figure 3.2. The protein effective pore diffusivities can be obtained from the corresponding van Deemter plot as reduced HETP vs. reduced velocity as shown in Figure 3.3. For both monomer and dimer, the slopes are higher for Type I than for Type II, indicating greater diffusional hindrance in the smaller pores of the former material. Table 3.3 summarizes the K_D and D_e values obtained from these data. These K_D values and those obtained for PEGs of similar size are comparable as seen in Figure 2.4 in Chapter 2. The monomer and dimer D_e values are a fraction of the corresponding values of the free diffusivity D_0 because of a diffusional hindrance. The smaller D_e values for Type I and for the dimer compared to Type II and the monomer are consistent with the smaller pore size of Type I and the larger molecular size of the dimer, respectively.

39
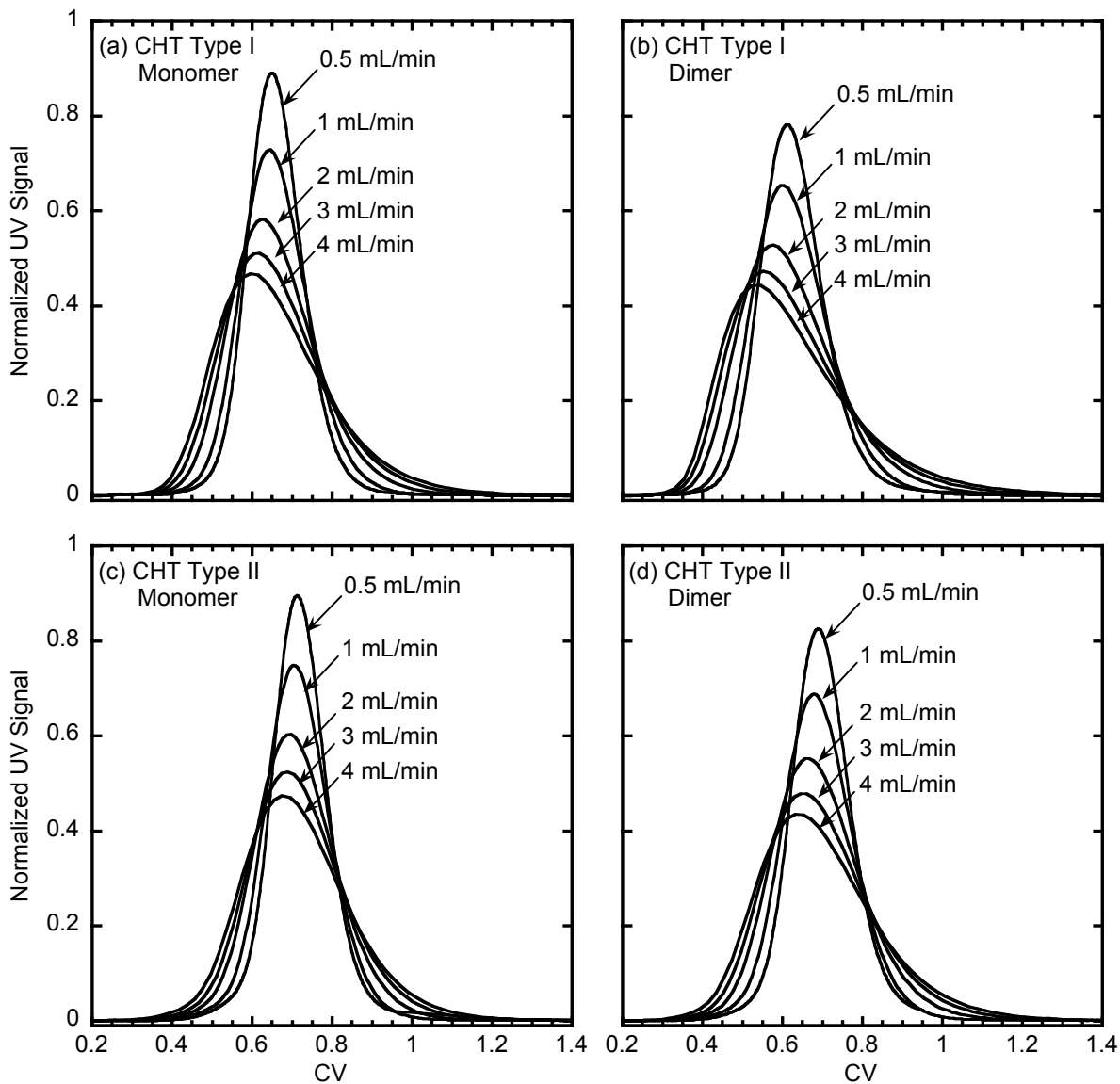
Figure 3.2. Isocratic elution peaks obtained from mAb monomer and mAb dimer in CHT Type I (a and b) and Type II (c and d) at different flow rates under non-binding conditions (500 mM Na_2HPO_4).
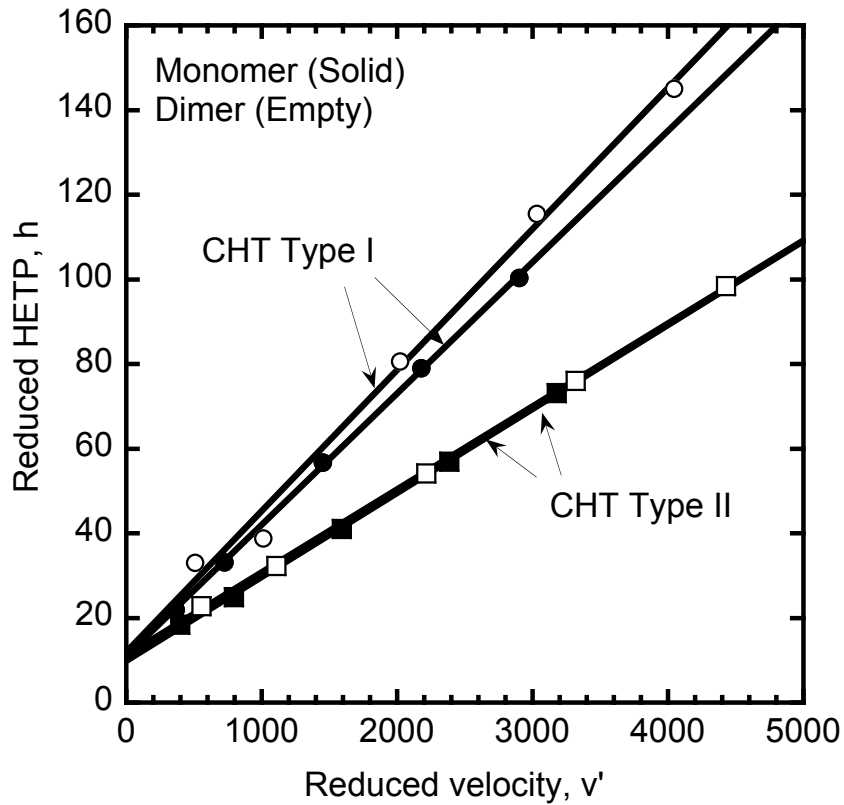
Figure 3.3. Reduced HETP vs. reduced velocity obtained for the mAb monomer and the mAb dimer in CHT Type I and Type II columns from pulse injections under non-binding conditions (500 mM Na$_2$HPO$_4$).

Table 3.3. Intraparticle effective pore diffusivities determined under non-binding conditions (500 mM Na$_2$HPO$_4$) and under strong binding conditions (10 mM Na$_2$HPO$_4$) for CHT Type I and Type II. D_e-values are in 10^{-7} cm^2/s. D_0-values are 3.9×10^{-7} and 2.8×10^{-7} cm^2/s for the monomer and dimer, respectively.

Molecule	CHT Type	Non-binding conditions			Binding conditions		
		K_D	D_e	$\dfrac{D_e}{D_0}$	D_e	$\dfrac{D_e}{D_0}$	$\dfrac{D_{e,\text{binding}}}{D_{e,\text{non-binding}}}$
Monomer	I	0.52±0.01	0.54±0.01	0.14	0.13±0.04	0.033	0.24
	II	0.61±0.01	0.94±0.01	0.24	1.07±0.02	0.26	1.09
Dimer	I	0.47±0.01	0.33±0.02	0.12	0.083±0.04	0.029	0.25
	II	0.58±0.01	0.66±0.01	0.24	0.78±0.02	0.28	1.18

Mass transfer characteristics under binding conditions were obtained from CLSM experiments in

10 mM Na_2HPO_4. For these conditions, the adsorption isotherms are very steep for both species

and CHT types. Figure 3.4 shows the single component adsorption results. As seen in this figure,

the behavior is qualitatively the same in all four cases with adsorption occurring with a sharp

adsorption front between the inner protein-free core and the outer, protein-saturated layer. A

closer inspection of the images shows that adsorption occurs faster for the monomer compared to

the dimer and is much faster for Type II compared to Type I for both monomer and dimer. For

example, as seen in Figure 3.4, full saturation with the monomer requires more than 60 min for

Type I but requires less than 10 min for Type II. Similarly, full saturation with the dimer requires

more than 120 min for Type I but less than 15 min for Type II.

Figure 3.5 shows the dimensionless front position, $\rho_s = r_s / r_p$, where r_s is the actual front

position, vs. time normalized by the actual particle radius, r_p. The data are scattered due, in part,

to the fact that the particles are not exactly spherical. Nevertheless, it is evident that the

adsorption front moves into the particle faster initially, then more slowly, and finally very

quickly as the particle becomes completely saturated. This behavior is consistent with the well-

known shrinking-core (SC) model (Ruthven, 1984). Treating the isotherm as rectangular and

assuming that the adsorption process is controlled by diffusion in the particle pores, the

following equation describes the relationship between front position and time (Martin *et al.*,

2005; Reck *et al.*, 2015):

$$2\rho_s^3 - 3\rho_s^2 + 1 = \frac{6CD_et}{q_mr_p^2} \tag{3.4}$$

where C is the protein concentration in solution. The calculated ρ_S-values obtained by fitting

this equation to the data are shown by the lines in Figure 3.5 and the corresponding fitted D_e-

values are given in Table 3.3. As seen in this table, the D_e values are all smaller than the free

solution diffusivity as a result of the limited porosity, tortuosity, and diffusional hindrance of the

pore network. Comparing non-binding and binding conditions shows a large difference between

D_e values for Type I but essentially no difference for Type II. We surmise that the Type I

behavior results from the bound protein restricting the space available for diffusion and thus

causing additional diffusional hindrance. Because the pores are substantially larger in Type II

restriction of diffusional transport due to the bound protein appears to be insignificant.

Interestingly, although as shown by the TEM images some large pores exist in both Type I and

Type II materials where diffusional hindrance is likely to be minimal, the overall kinetic

behavior seems to be more closely correlated with the average pore radii determined by iSEC in

chapter 2, 30 and 49 nm for Type I and Type II, respectively.

(a) mAb monomer (top) and dimer (bottom) on CHT Type I

1 min | 10 min | 60 min | 120 min
1 min | 10 min | 60 min | 120 min | 180 min
20 µm

(b) mAb monomer (top) and dimer (bottom) on CHT Type II

1 min | 5 min | 10 min | 15 min
1 min | 5 min | 10 min | 15 min
20 µm
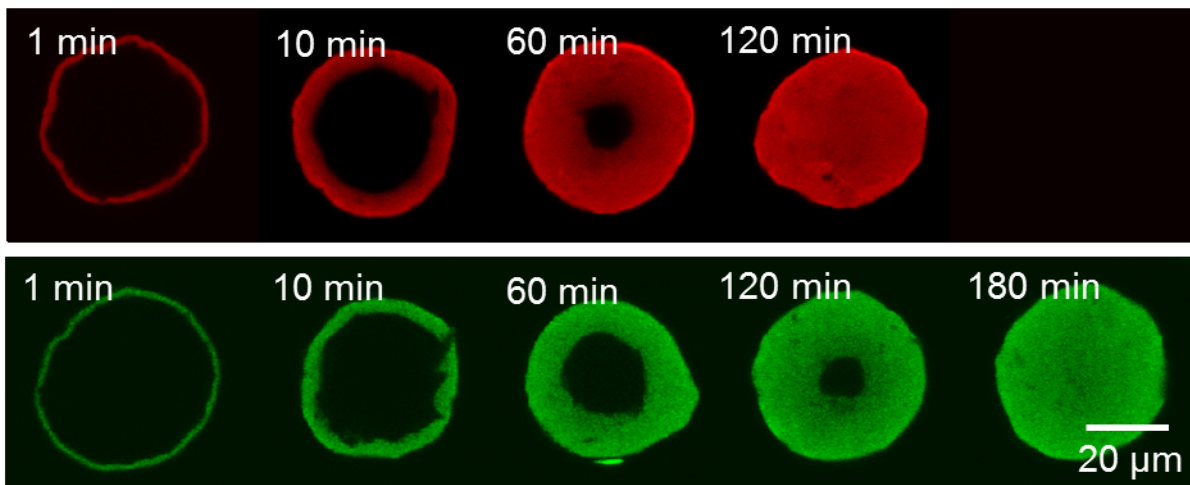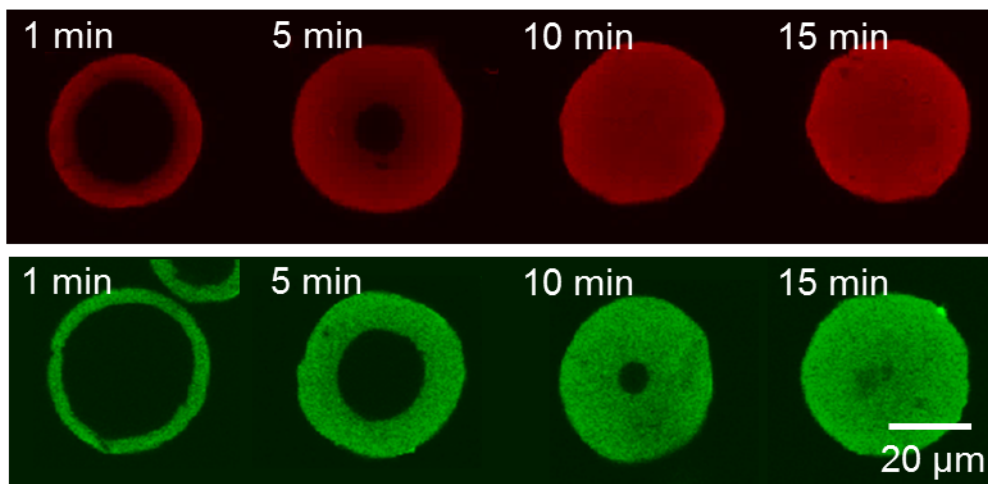
Figure 3.4. CLSM images for single component adsorption of the mAb monomer and the mAb dimer in 10 mM Na_2HPO_4 on (a) CHT Type I particles and (b) CHT Type II particles. Monomer and dimer concentrations were 1 mg/mL.
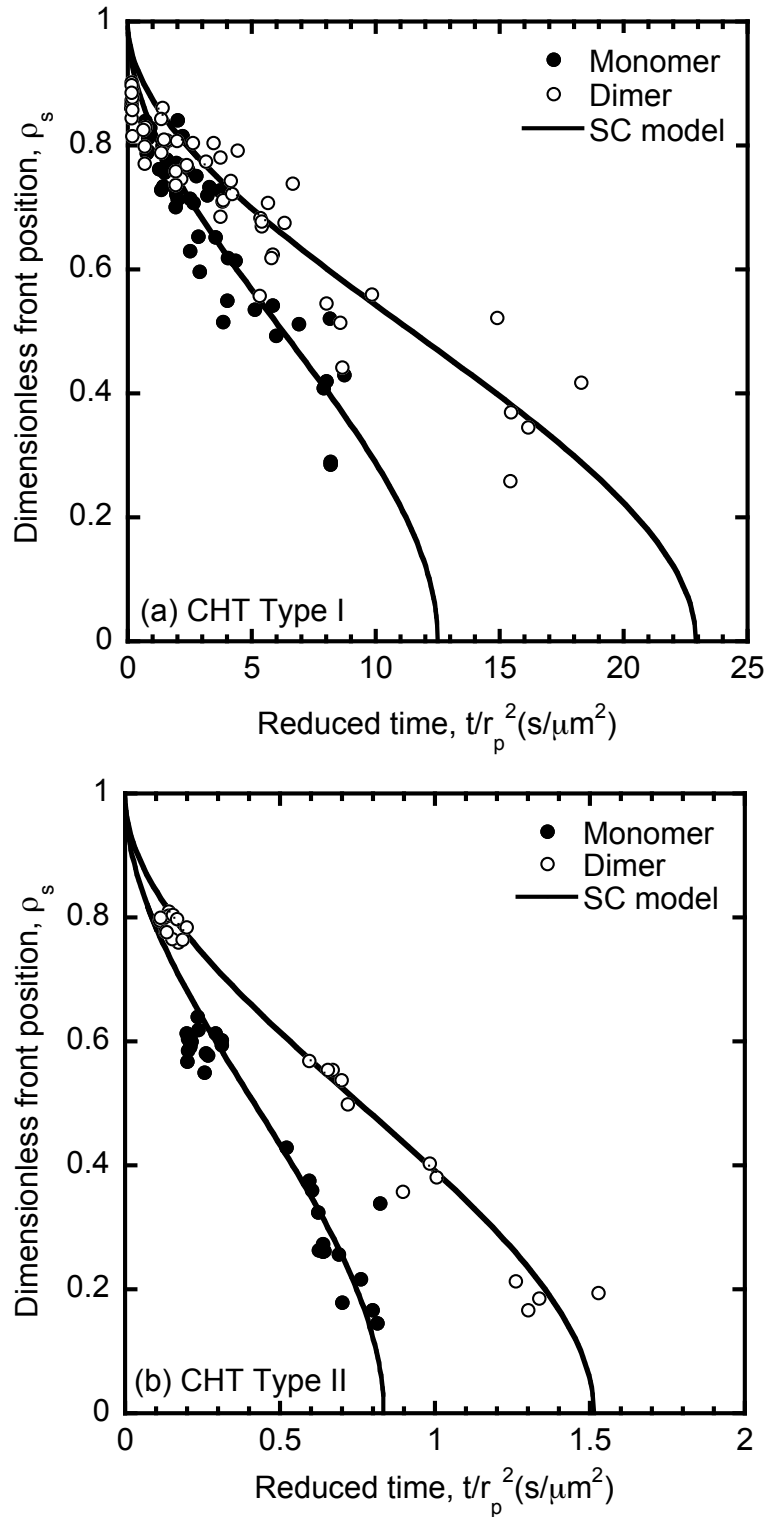
Figure 3.5. Dimensionless position of adsorption front for the mAb monomer and the mAb dimer on (a) CHT Type I particles and (b) CHT Type II particles for the conditions of Figure 3.4. Lines are based on Eq. (3.4).

Figure 3.6 and Figure 3.7 show the CLSM results obtained from the adsorption of the mAb monomer-dimer mixture on CHT Type I and Type II, respectively, for the same conditions as Figure 3.4. Clear evidence of displacement of bound monomer by the dimer is seen for both Type I and Type II. In both cases, the weaker binding monomer diffuses ahead of the strong binding and slower diffusing dimer, concentrating in a ring ahead of the dimer front and eventually accumulating near the center of the particles. For a longer time, the excess bound monomer is largely displaced by the advancing dimer front so that the particles attain an essentially uniform distribution of monomer and dimer. The time needed for the process is obviously much longer for Type I (about 180 min) compared to Type II (about 20 min) as a result of the smaller pores and slower transport in Type I. Figure 3.8 shows the dimensionless positions of the two fronts observed during adsorption of the mixture as a function of reduced time. The faster moving front corresponds to the monomer binding to the clean HAP nanocrystals while the slower moving front corresponds to the displacement of the bound monomer by the dimer. Assuming rectangular isotherms for both monomer and dimer and that both adsorption and displacement kinetics are completely diffusion controlled, the positions of the two fronts, $\rho_{s,M}$ and $\rho_{s,D}$, are described by the following equation (Martin *et al.*, 2005; Reck *et al.*, 2015)

$$2\rho_{s,D}^3 - 3\rho_{s,D}^2 + 1 = \frac{6C_D D_{e,D} t}{q_D^* r_p^2} \tag{3.5}$$

$$2\rho_{s,M}^3 - 3\rho_{s,M}^2 + 1 = \left(\frac{q_{m,M} - q_M^*}{q_{m,M}}\right)\left[1 + \frac{q_D^* D_{e,M} C_M}{\left(q_{m,M} - q_M^*\right)D_{e,D}C_D}\right]\frac{6C_D D_{e,D} t}{q_D^* r_p^2} \tag{3.6}$$

where $q_{m,M}$ is the adsorbed monomer concentration in equilibrium with pure monomer and q_M^* and q_D^* are the monomer and dimer adsorbed concentration in equilibrium with the mixture. The

lines in Figure 3.8 are calculated according to this equation using the values of q_M^* and q_D^* predicted from Eq. (3.3) with the parameter values determined for the mixture and the D_e-values determined from the single component CLSM data. The agreement with the data is only approximate, with average deviations between model and data of 12 and 19% for monomer and dimer, respectively, in the case of Type I, and -5.5 and 4.2% for monomer and dimer, respectively, in the case of Type II. These deviations occur in part because the model assumes a rectangular isotherm without kinetic resistance to binding and/or displacement, which may not be completely accurate. Moreover, the deviations also arise from inaccuracies associated with predicting the two-component binding capacity values q_M^* and q_D^*. The latter are affected by absolute relative errors estimated to be in the 11-14% range. An improved description of the two-component kinetic data could be obtained by adjusting these values within the estimated error range (seen in the Figure 7.4 of Appendix). Nevertheless, even without adjustment of parameters and considering the underlying assumptions, the key features and the overall rates of the binary adsorption process are captured well by the two-front SC model embodied in Eqs. (3.5) and (3.6). The substantial agreement between model predictions without parameter adjustment and experimental results suggest that the binary adsorption kinetics is also nearly completely diffusion controlled. As for the single component case, the overall kinetics is much slower for CHT Type I than for Type II as a result of the smaller pore size of the former.
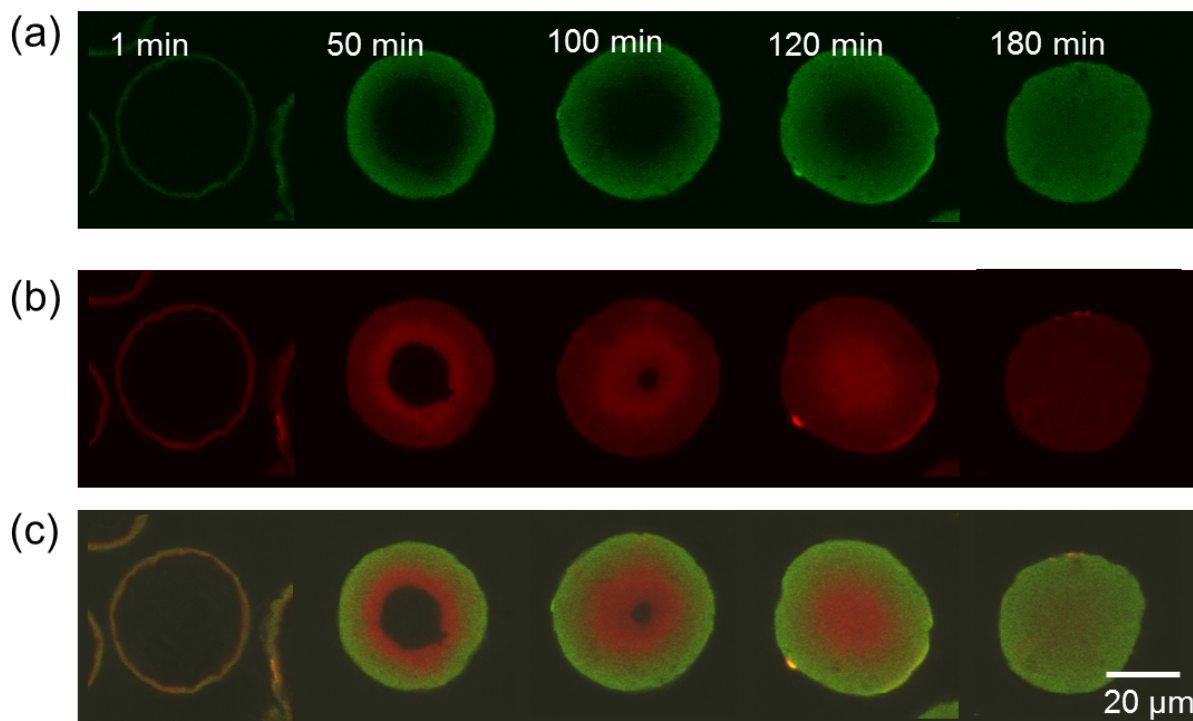
Figure 3.6. CLSM images for binary adsorption of the mAb monomer-dimer in 10 mM Na_2HPO_4 on CHT Type I particles. Monomer and dimer concentrations were each 0.5 mg/mL. (a) monomer, (b) dimer, (c) composite image.
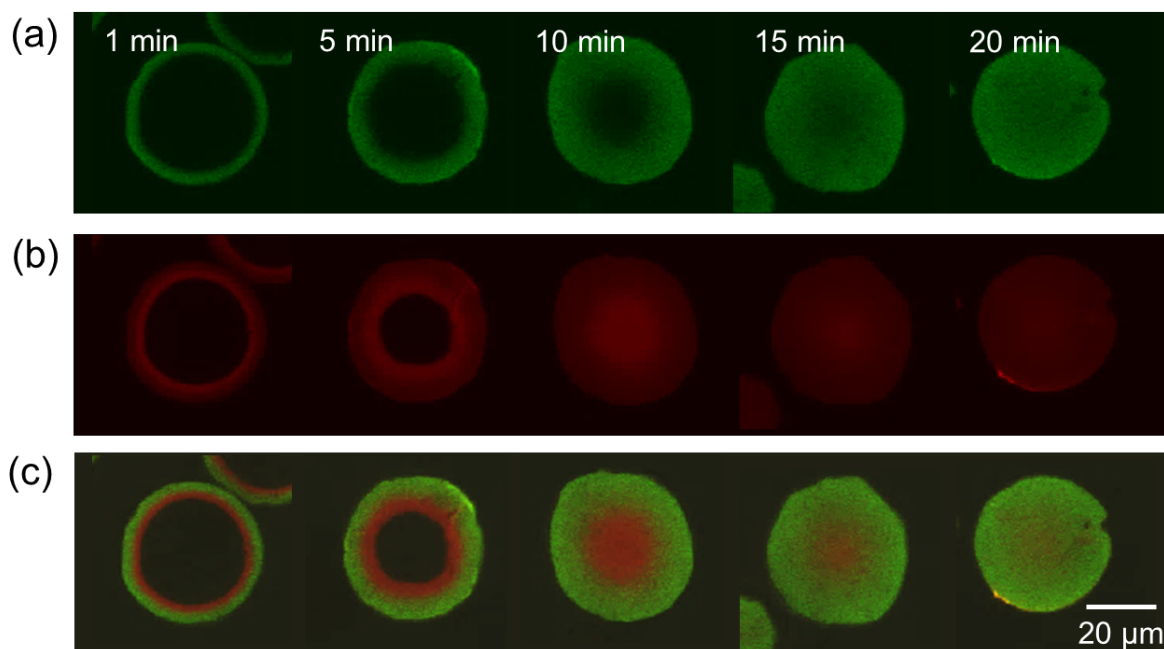
Figure 3.7. CLSM images for binary adsorption of the mAb monomer-dimer in 10 mM Na_2HPO_4 on CHT Type II particles. Monomer and dimer concentrations were each 0.5 mg/mL. (a) monomer, (b) dimer, (c) composite image.
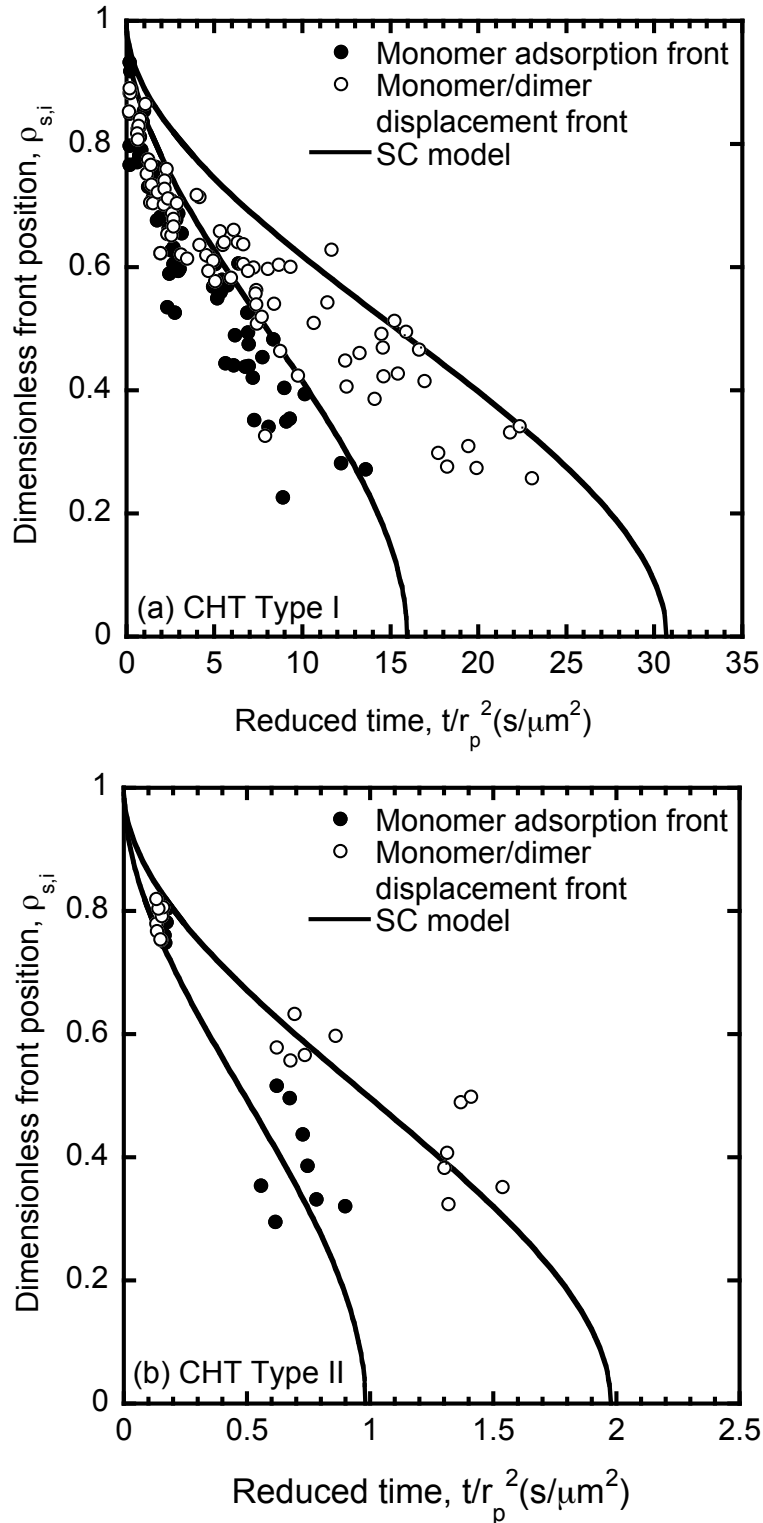
Figure 3.8. Dimensionless position of the monomer adsorption front and the monomer-dime displacement front during binary adsorption of the mAb monomer-dimer mixture on (a) CHT Type I particles and (b) CHT Type II particles for the conditions of Figure 3.6 and Figure 3.7. Lines are based on Eqs.(3.5) and (3.6).

3.3.3 Comparison with cation exchange behavior

In a previous study, Reck *et al.* (2015) reported the adsorption behavior of the same mAb monomer-dimer system at pH 7 on the cation exchange resin Nuvia HR-S from Bio-Rad Laboratories (Hercules, CA, USA). This resin has a hydrophilic polymer backbone and sulfopropyl functionality, particle diameter of 52 μm, and pore radius around 50 nm, the latter being fairly comparable to CHT Type II. The monomer and dimer maximum binding capacities were 130 and 140 mg/mL, respectively, at low ionic strength (20 mM Na^+) and decreased to about 50 and 70 mg/mL for the monomer and dimer, respectively, with (120 mM Na^+). These capacities are also comparable to those observed for CHT Type I, but higher, as expected, than those obtained for CHT Type II, because of the lower surface area of this material. In terms of dimer/monomer selectivity, very low selectivity (around 1) was observed for Nuvia HR-S at low ionic strength (20 mM Na^+). Higher selectivities (up to about 8-13) than those observed for CHT were only observed for Nuvia HR-S at higher Na^+ concentrations but the expense of lower binding capacities. Finally, in terms of mass transfer rates, the monomer and dimer D_e-values for Nuvia HR-S were $0.80x10^{-7}$ and $0.41x10^{-7}$ cm^2/s, respectively. These values are much higher than those observed in this work for CHT Type I ($0.12x10^{-7}$ and $0.08x10^{-7}$ cm^2/s, respectively), but significantly lower than for CHT Type II ($1.03x10^{-7}$ and $0.73x10^{-7}$ cm^2/s, respectively), especially for the dimer.

Chapter 4 Frontal Chromatography for the Monoclonal Antibody Monomer-dimer Separation on Ceramic Hydroxyapatite

4.1 Introduction

As shown in Chapter 1, many practical applications of hydroxyapatite (HAP) as a chromatographic medium have been developed over the years based on these unique selectivities along with the absence of hydrophobic interaction, including the purification of DNA, enzymes, virus-like particles, and immunoglobulins (Cook *et al.*, 1999; Giovannini and Freitag, 2000; Saito *et al.*, 2016; Schmoeger *et al.*, 2010; Shi *et al.*, 2007). Industrially, one of the major applications of HAP is the removal of aggregates in monoclonal antibody (mAb) purification (Gagnon, 2008; Sun *et al.*, 2016; Vázquez-Rey and Lang, 2011).

Yet, despite the popularity of HAP in practical applications, few studies have been published addressing protein adsorption kinetics, especially, for multicomponent systems at high loadings. An exception is our recent work presented in Chapter 3 aimed at characterizing the competitive binding of monoclonal antibody monomer-dimer mixtures. We observed that both monomer and dimer adsorption kinetics are affected by intraparticle diffusion for both ceramic hydroxyapatite (CHT) Type I and Type II, although the effect was much more pronounced for the dimer compared to the monomer on both types, because of the larger size of the dimer, and much more pronounced for both monomer and dimer for Type I compared to Type II, because of the smaller pore size of the latter. One of the key results of our prior work was that despite the presence of significant mass transfer limitations, especially in Type I, displacement of the monomer by the dimer still occurred over relatively short time scales during mixture adsorption resulting a selective binding of the dimer relative to the monomer at equilibrium. This result suggests that

separation of antibody monomer-dimer mixtures could be carried by frontal analysis (or frontal loading) in CHT columns at reasonable flow rates.

The objectives of this chapter are twofold. The first is to establish experimentally the feasibility of implementing frontal analysis-based separations of antibody monomer-dimer mixtures at reasonable residence times. The second is to develop a mechanistic model to predict the separation. We expected the process to be influenced by mass transfer and, thus, dependent on residence time. However, additional factors related to the kinetics of displacement of the monomer by the dimer could also play a role while diffusional mass transfer kinetics is the starting point, we consider models that also account for potential kinetics limitations affecting the exchange of monomer for dimer molecules on the adsorbent surface. Such a model can then be used to predict separation as a function of residence time, protein concentration, and the monomer/dimer ratio in the feed. As in Chapter 3, we consider both CHT Type I and Type II. Based on our previous observations in batch mode, we expect smaller rates and greater impact of intraparticle diffusion on the column behavior of Type I, but faster rates, with a greater possibility of exchange kinetics effects for Type II. Experimental measurements and modeling are used synergistically to understand the controlling factors in both cases.

4.2 Materials and methods

4.2.1 Materials

The CHT samples Type I and Type II used in this work were as same as those used previously. Intraparticle porosities accessible by antibody monomer and dimer molecules under non-binding conditions, ε'_p, were 0.52 and 0.47, respectively, for Type I and 0.61 and 0.58, respectively, for Type II. The monoclonal antibody samples used in this work as same as those used in Chapter 3 with same preparation steps. All other chemicals used in buffer preparations were purchased

52

from Thermo Fisher Scientific (Waltham, MA, USA) and MilliporeSigma (St. Louis, MO, USA).

4.2.2 Adsorption equilibrium and kinetics measurements

Some additional adsorption equilibrium and kinetics measurements were conducted in this work to supplement the data in Chapter 3 by extending the number of experimental measurements and the range of salt concentrations. Additional co-adsorption kinetics measurements were also conducted by confocal laser scanning microscopy (CLSM) for a monomer-dimer mixture in 10 mM Na$_2$HPO$_4$ with additional 50 mM NaCl at pH 7 to supplement data obtained previously in Chapter 3 in the same buffer but without the addition of NaCl. Images from these measurements and the procedure used to determine the D_e are provided in Appendix.

4.2.3 Column experiments

Frontal analysis experiments were conducted using 5 mm diameter x 50 mm long Tricorn 5/50 columns from GE Healthcare packed with CHT Type I or Type II. Following the CHT supplier instructions, both columns were flow-packed in a 10 mM Na$_2$HPO$_4$ buffer at pH 7.0 containing 1 M NaCl at a flow rate of 2 mL/min while mechanically tapping the column sharply until the bed height stabilized. Actual bed heights were 2.3 and 2.5 cm, for CHT Type I and Type II, respectively, with corresponding bed volumes of 0.45 and 0.49 mL. Although these columns are short in order to conserve materials, we operated them at flow rates sufficiently low to obtain reasonable residence times (see below). Since we expect mass transfer effects to be dominant, residence time, rather than bed height alone, is the relevant criterion for the choice of experimental conditions (Carta and Jungbauer, 2010; Ruthven, 1984). The packing quality was determined from NaCl pulse injections, which gave reduced HETP ($h = \text{HETP} / d_p$, where d_p is

the average particle diameter) of 8.6 and 9.0, and asymmetry factors of 1.68 and 1.52 for Type I and II, respectively. For the frontal analysis runs the load flow rate was varied between 0.08 and 0.2 mL/min corresponding to residence times between 2.5 and 5.6 min. The total protein concentration in the feed mixture was 2.0±0.2 mg/mL with dimer content varying between 17 and 32%. The effluent from the column was collected in 1 mL increments into 2 mL polystyrene round-bottom tubes (Becton Dickinson, Lincoln Park, NJ, USA) using a Model F9-R fraction collector from GE Healthcare (Piscataway, NJ, USA). Monomer and dimer concentrations were then determined using analytical SEC with a Waters Acquity BEH SEC 200 column (4.6x150 mm, 1.7 μm particle size) and a Waters Acquity H-Class UPLC system (Milford, MA, USA) as described in Chapter 3. Single component breakthrough curves were also obtained for the monomer with just UV detection of the effluent profile. Following each experiment, the columns were stripped with 500 mM Na_2HPO_4 at pH 7.0 and cleaned with 1 M NaOH.

Isocratic elution experiments were carried out with the isolated monomer and dimer samples at relatively high salt concentrations where binding is weak and follows a linear isotherm. For these experiments, CHT was packed into 10 mm diameter x 100 mm long Tricorn 10/100 columns (GE Healthcare) at 5 mL/min to a final bed volume of 6.7±0.1 mL, corresponding to a bed height of 8.5±0.1 cm. The packing quality was again determined from NaCl pulse injections, which gave reduced HETP values of 3.9 and 2.5 and asymmetry factors of 1.2 and 1.1 for Type I and II, respectively. The extraparticle porosity in these columns was 0.29 and 0.30 for Type I and Type II, respectively. For the isocratic elution experiments, the isolated monomer and dimer samples were buffer-exchanged into the running buffer injected individually into the column in 100 μL volume and eluted at 1 mL/min. The columns were stripped with 500 mM Na_2HPO_4 and re-equilibrated in the running buffer after each chromatographic run.

4.3 Experimental results

4.3.1 Protein adsorption equilibrium

Figure 4.1 shows the isotherm data for monomer and dimer as single components and as mixture in the concentration range of 0-8 mg/mL for the monomer and 0-3 mg/mL for the dimer in 10 mM Na_2HPO_4 buffers at pH 7 containing 0, 50, 80, and 160 mM NaCl, corresponding to 20, 70, 100, and 180 mM Na^+. As shown in Chapter 3, the sodium ion concentration determines both monomer and dimer binding regardless of the specific phosphate concentration at these relatively high phosphate concentrations. Preferential binding of the dimer relative to the monomer is evident from Figure 4.1 at each Na^+ concentration as seen from the steep drop of monomer binding, q_M, along the C_D axis, compared to the much shallower drop of dimer binding, q_D, along the C_M axis. The data set was fitted to the two-component Langmuir isotherm:

$$q_i = \frac{q_{m,i} K_i C_i}{1 + K_M C_M + K_D C_D} \tag{4.1}$$

with parameters $q_{m,i}$ and K_i regressed to the data individually at each Na^+ concentration. These parameters are summarized in Table 4.1 and calculated surfaces are shown in Figure 4.1. Both the experimental results and the fitted parameters agree with our previous measurements. Although, as seen in this table, the regression error of the fitted parameters K_M and K_D is large due to the steepness of the pure-component isotherms especially at low Na^+ concentrations, predictions of the mixture binding capacities based on Eq. (4.1) using the mean value of the regressed coefficients were fairly accurate giving an average absolute error of 6-12% for the monomer and 3-6% for the dimer on Type I and 10-19% for the monomer and 2-7% for the dimer on Type II.
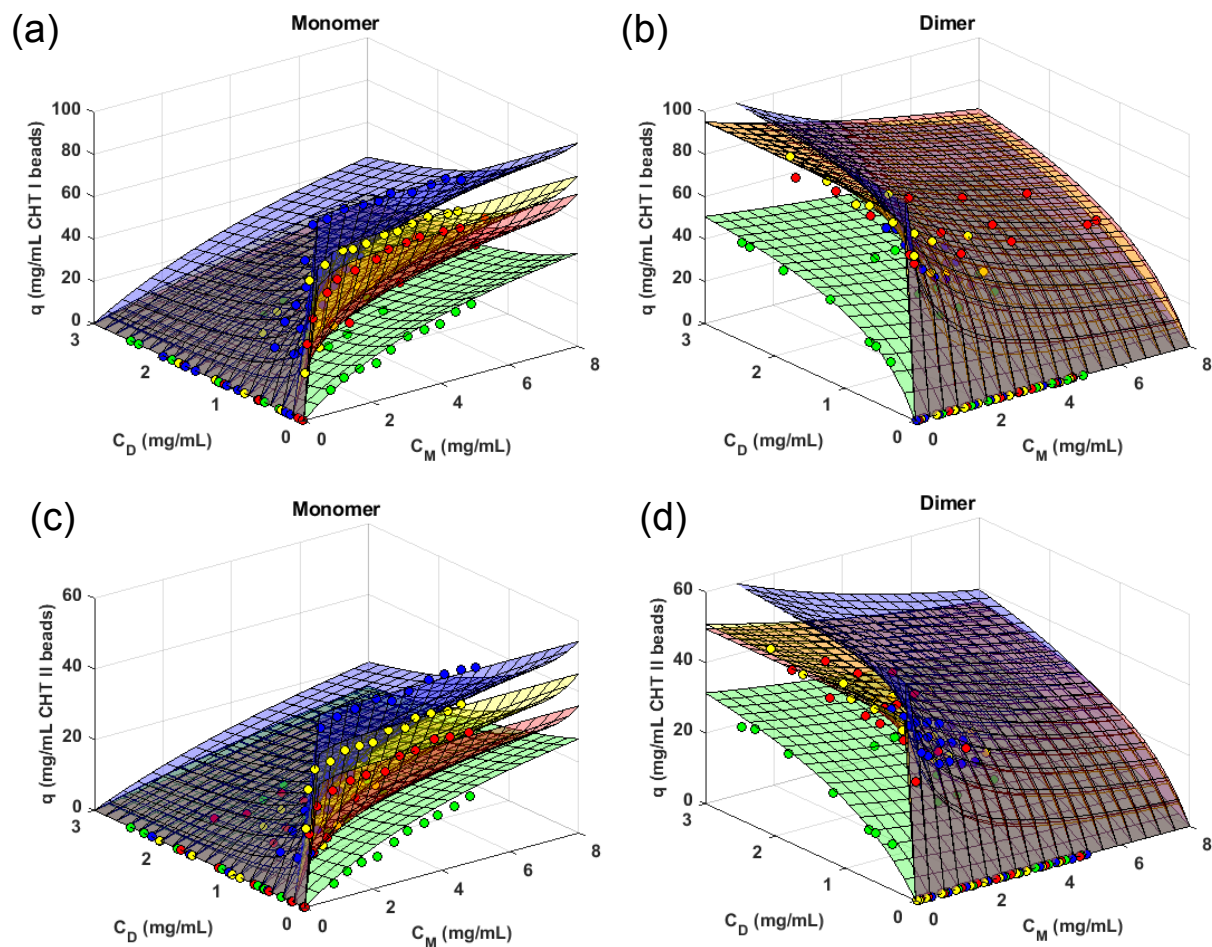
Figure 4.1. Multi-component adsorption isotherms on CHT Type I (a, b) and CHT Type II (c, d) for the monomer (a, c) and for the dimer (b, d) in 10 mM Na_2HPO_4 buffers containing different NaCl concentrations at pH 7. The dots in blue, yellow, red and green represent 20, 70, 100 and 180 mM Na^+ concentrations, respectively. The surface lines are calculated with the two-component Langmuir isotherm model Eq. (4.1) using the best-fit parameters given in Table 4.1.

Table 4.1. Langmuir isotherm parameters fitted to the data in Figure 4.1 according to Eq. (4.1). $q_{m,i}$ values are in mg/mL of CHT bead volume and K_i values are in mL/mg.

[Na$^+$] (mM)	CHT Type I				CHT Type II			
	$q_{m,M}$	K_M	$q_{m,D}$	K_D	$q_{m,M}$	K_M	$q_{m,D}$	K_D
20	96±2	140±55	110±2	460±180	52±2	170±260	64±2	710±120
70	81±3	17±4	96±3	934±25	45±1	35±9	51±1	220±59
100	73±3	13±4	96±5	80±26	36±2	35±17	50±2	250±110
180	70±7	0.2±0.0	64±3	1.3±0.2	47±8	0.2±0.0	47±4	0.7±0.1

In prior work, we have shown that while double in molecular mass, the dimer is only about 30% larger than the monomer in terms of hydrodynamic radius, indicating that both monomer and dimer are in a globular form. Nevertheless, we have shown previously that despite being relatively close in physical size, the effective binding charge of the dimer on a cation exchange resin is much higher than that of the monomer (14.8 vs. 10.2), which resulted in stronger binding of the dimer. We hypothesize that the mechanism leading to selectivity for the dimer is similar in CHT and that it is driven by the larger footprint of the dimer allowing stronger interactions with the phosphate groups on the hydroxyapatite crystals. As a result, it is likely that selective binding of the dimer and displacement of the monomer by the dimer results from a cation exchange mechanism where the species with the higher binding charge is preferred.

4.3.2 Separation by frontal analysis

Figure 4.2 shows the binary breakthrough curves and the monomer purity obtained during frontal loading of monomer-dimer mixtures containing approximately 32% dimer obtained at a residence time of 5.0 min with the CHT Type I column (top panels) in comparison with those obtained at a residence time of 5.6 min with the Type II columns (bottom panels) in buffers containing either 20 mM Na$^+$ (left panels) or 70 mM Na$^+$ (right panels). Figure 4.3 shows additional results for the CHT Type II column with (a) a load buffer containing 100 mM Na$^+$ and (b) with a load buffer containing 70 mM Na$^+$ as in Figure 4.2d, but with a lower dimer content of 17% and a shorter residence time of 2.5 min. In each case, two-component breakthrough profiles calculated assuming local equilibrium conditions and no axial dispersion are also shown. These profiles were calculated according to the following equations (Carta and Jungbauer, 2010; Ruthven, 1984):

$$CV_I = \varepsilon + (1-\varepsilon)\frac{q_M(C_M',0)}{C_M'} \tag{4.2}$$

$$CV_{II} = \varepsilon + (1-\varepsilon)\frac{q_M(C_M',0)-q_M(C_{M,F},C_{D,F})}{C_M'-C_{M,F}} = \varepsilon + (1-\varepsilon)\frac{q_D(C_{M,F},C_{D,F})}{C_{D,F}} \tag{4.3}$$

where CV_I and CV_{II} are indicate the pure monomer breakthrough front and the monomer-dimer displacement front, respectively, both in column volume units, C_M' is the pure monomer plateau concentration, and $C_{M,F}$ and $C_{D,F}$ are the feed monomer and dimer concentrations. Binding capacities $q_M(C_M,C_D)$ and $q_D(C_M,C_D)$ are given by the two-component isotherms and are calculated for pure monomer at equilibrium with C_M' and for the monomer and dimer at equilibrium with the feed mixture using the isotherm parameter values in Table 4.1. As seen in these figures, the two-component breakthrough curves conform qualitatively with the local

58

equilibrium predictions based on Eqs. (4.2) and (4.3) for both Type I and Type II. This qualitative agreement is indicated by (a) the overshoot of the monomer breakthrough curve above its feed concentration, which indicates displacement of the monomer by the dimer, and (b) the positions of the pure monomer breakthrough front and of the monomer-dimer displacement front relative to the solid and dashed lines in this figure that were calculated directly from the binding isotherms. The actual profiles are, of course, broader than those predicted under ideal conditions, but the transitions and the qualitative trends are similar to those predicted by the equilibrium model.

Despite the qualitative agreement with the local equilibrium relationships, the experimental profiles and the corresponding monomer purity are strongly dependent on the CHT type, on the Na^+ concentration, and on the residence time. In all cases, while the pure monomer breakthrough profile remains very sharp, the displacement front is much broader than predicted under local equilibrium conditions. This discrepancy is especially pronounced for CHT Type I (Figure 4.2a, b), at low Na^+ concentrations (Figure 4.2a, c), and at low residence times (Figure 4.3b). The monomer purity is also affected, of course. While it is predicted to be 100% purity between the pure monomer front and the displacement front, the data show monomer purity values below the prediction.

From a practical viewpoint, selection of conditions that could be used to optimize monomer-dimer separations by frontal analysis with CHT, could be done, in principle just based on the experimental observations. For example, it is obvious that while CHT Type I has greater binding capacity than Type II leading to a greater separation between the pure monomer front and the mixture front, it also exhibits broader breakthrough profiles. As a result, at these relatively short residence times, much of the advantage of the greater binding capacity of Type I is lost.

59

Operating at higher Na^+ concentrations (e.g. 70 mM Na^+ vs. 20 mM Na^+) also reduces binding capacity and, thus, reduces the distance between the pure monomer front and the monomer-dimer displacement front, but also results in a sharper displacement front and, thus, better separation. This effect is especially evident for CHT Type II and can be seen comparing Figure 4.3c and d, with 20 and 70 mM Na^+, respectively. Going further up in Na^+ concentration to, for example, 100 mM Na^+, as seen in Figure 4.3a, does result in a slightly sharper displacement front, but further reduces the binding capacity actually resulting in a net decrease in separation performance.

A mechanistic model capable of describing the separation would help select conditions and reduce the extent of experimentation. For example, such a model could be used to find an optimum residence time that will provide a suitable compromise of capacity utilization, which is higher at lower flow rates, and process speed, which is faster at higher flow rates, or to predict the effects of varying the percentage of dimer in the feed mixture. Such a model can also help explain the relative importance of mass transfer and binding kinetics and help understand the root causes of the behaviors observed experimentally.
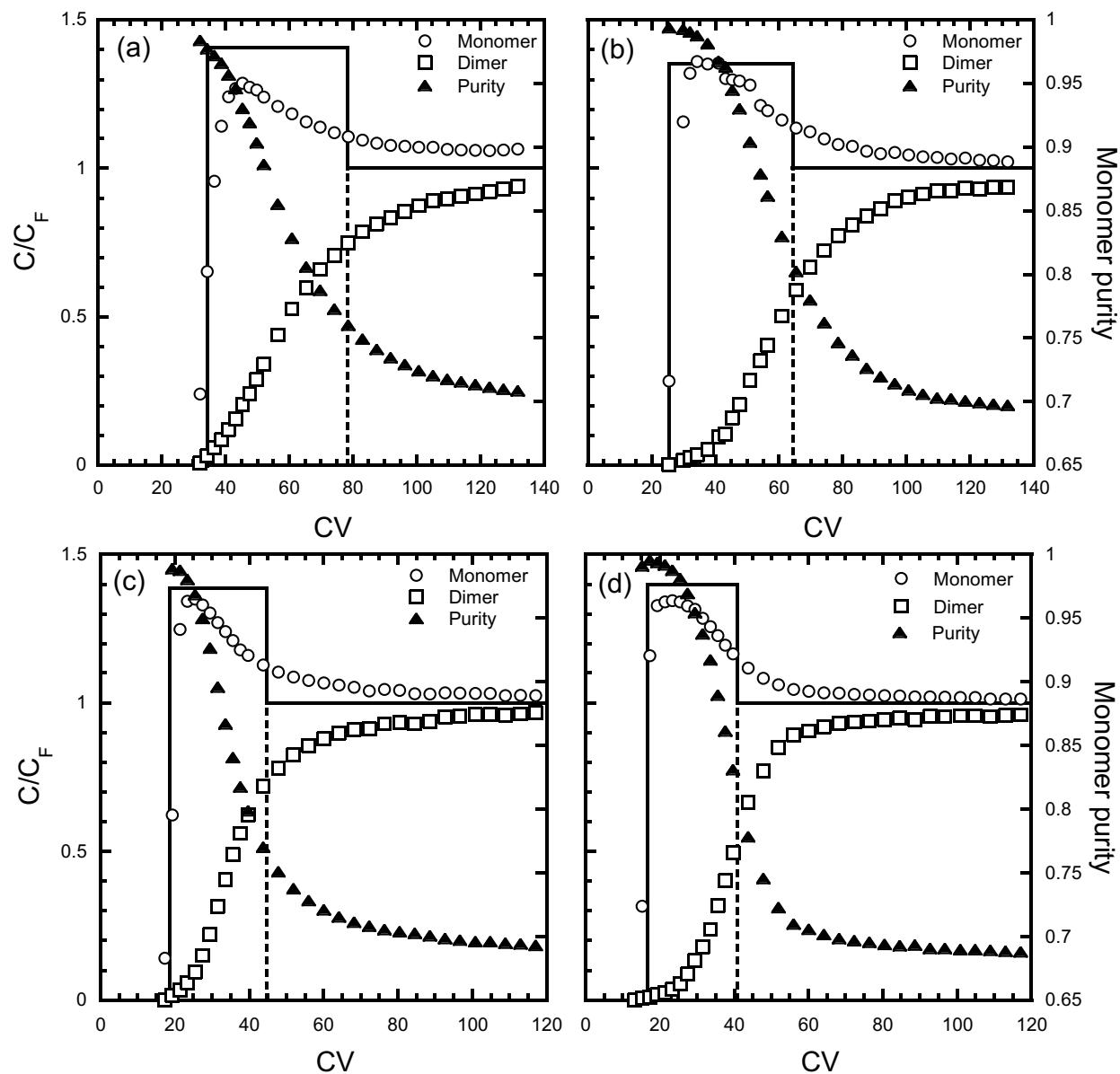
Figure 4.2. Binary breakthrough curves of monomer-dimer mixtures containing approximately 30% dimer on CHT Type I (a, b) and CHT Type II (c, d) in 10 mM Na_2HPO_4 load buffers containing different NaCl concentrations at pH 7. (a, c) 20 mM Na^+, (b, d) 70 mM Na^+. The solid and dashed lines are model prediction based on Eqs. (4.2) and (4.3) using the parameters listed in Table 4.1. The residence time was 5.0 min in (a) and (b) and 5.6 min in (c) and (d).

61
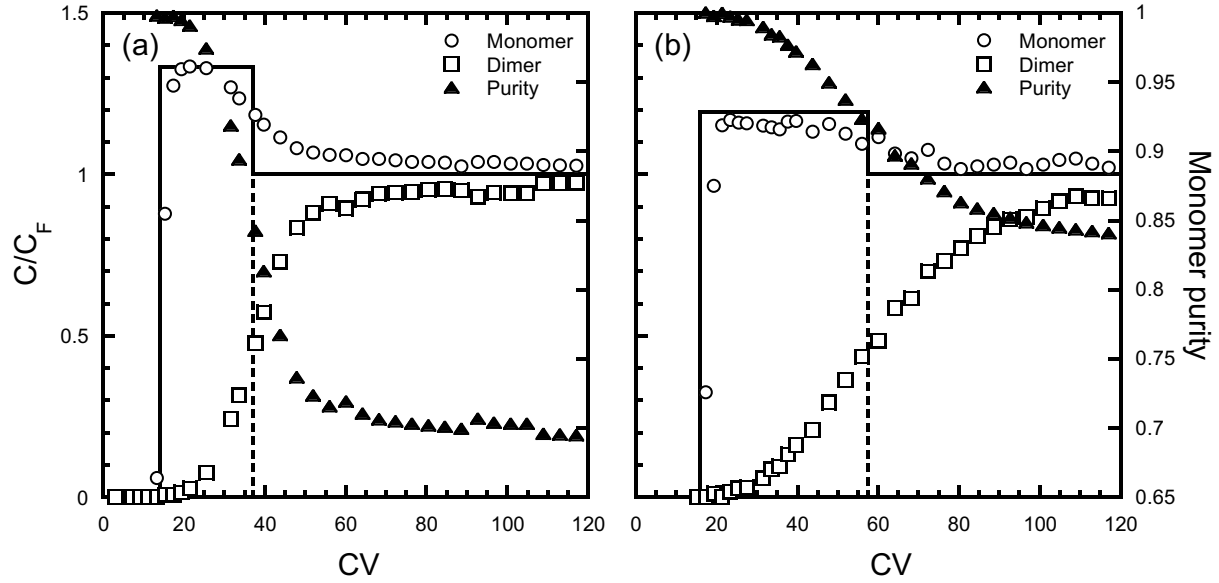
Figure 4.3. Binary breakthrough curves of monomer-dimer mixtures on CHT Type II containing approximately 30% dimer (a) and 17% dimer (b). The load buffers were 10 mM Na_2HPO_4 with different NaCl concentrations at pH 7 corresponding to 100 mM Na^+ (a) and 70 mM Na^+ (b). The solid and dashed lines are model predictions based Eqs. (4.2) and (4.3) using the parameters listed in Table 4.1. The residence time was 5.6 min in (a) and 2.5 min in (b).

4.4 Model development

In order to successfully describe frontal analysis, a mechanistic model must take into account both mass transfer effects as well as any relevant kinetic resistance occurring during binding and displacement of one species by the other. Axial dispersion and flow non-uniformity may also have to be considered to model actual large-scale columns. Our analysis is, however, limited to well-packed columns with nearly uniform velocity, such as those used in our laboratory experiments. For these conditions, the continuity equation and boundary conditions for the column are written as follows:

$$\varepsilon D_L \frac{\partial^2 C_i}{\partial x^2} = u\frac{\partial C_i}{\partial x} + \varepsilon\frac{\partial C_i}{\partial t} + (1-\varepsilon)\frac{\partial \langle \hat{q}_i \rangle}{\partial t} \tag{4.4}$$

$$x = 0, \;\; C_i = C_{i,F} \tag{4.5}$$

$$x = L, \frac{\partial C_i}{\partial x} = 0 \tag{4.6}$$

where subscript i refers to either monomer (M) or dimer (D), D_L is the axial dispersion

coefficient, u is the superficial velocity, L is the column length, and $\langle \hat{q}_i \rangle$ is the average protein

concentration in the adsorbent particles. The expression used for the term $\partial \langle \hat{q}_i \rangle / \partial t$ in Eq. (4.4)

depends on transport and kinetic resistances within the adsorbent particles. Once these

intraparticle resistances are identified, extensions to account for non-uniform flow effects are

easily implemented via, for example, computational fluid dynamics packages (Gzil *et al.*, 2003).

Accordingly, the term $\partial \langle \hat{q}_i \rangle / \partial t$ can be written as:

$$\frac{\partial \langle \hat{q}_i \rangle}{\partial t} = \frac{3 D_{e,i}}{r_p} \left. \frac{\partial c_i}{\partial r} \right|_{r=r_p} \tag{4.7}$$

where r_p is the particle radius and c_i is the protein concentration in the adsorbent particle pores.

Note that these equations neglect the external boundary layer resistance since the Biot number

($Bi = k_f r_p / D_e$) is estimated to be in the range 40-100 based on established Sherwood number

correlations for mass transfer in packed beds to estimate k_f (Wilson and Geankoplis, 1966).

4.4.1 Model for pore diffusion control

For conditions where the adsorption and displacement kinetics are completely controlled by

intraparticle diffusion, adsorption equilibrium prevails at each point and time within the particles

and is described by Eq. (4.1). Accordingly, the continuity equations and boundary conditions for

the particles are written as follows:

$$\varepsilon_p' \frac{\partial c_M}{\partial t} + \frac{\partial q_M}{\partial t} = \frac{D_{e,M}}{r^2} \frac{\partial}{\partial r} \left(r^2 \frac{\partial c_M}{\partial r} \right) \tag{4.8}$$

$$\varepsilon'_p \frac{\partial c_D}{\partial t} + \frac{\partial q_D}{\partial t} = \frac{D_{e,D}}{r^2} \frac{\partial}{\partial r}\left(r^2 \frac{\partial c_D}{\partial r} \right) \tag{4.9}$$

$$r = 0, \frac{\partial c_M}{\partial t} = \frac{\partial c_D}{\partial t} = 0 \tag{4.10}$$

$$r = r_p, c_M = C_M, c_D = C_D \tag{4.11}$$

In these equations,

$$\frac{\partial q_M}{\partial t} = \frac{\partial q_M}{\partial c_M} \frac{\partial c_M}{\partial t} + \frac{\partial q_M}{\partial c_D} \frac{\partial c_D}{\partial t} \tag{4.12}$$

$$\frac{\partial q_D}{\partial t} = \frac{\partial q_D}{\partial c_M} \frac{\partial c_M}{\partial t} + \frac{\partial q_D}{\partial c_D} \frac{\partial c_D}{\partial t} \tag{4.13}$$

where the partial derivatives are taken from the isotherm, Eq. (4.1).

4.4.2 Models incorporating adsorption kinetics resistances

As extensively reviewed, for example, by Rabe *et al.* (2011), the kinetics of protein adsorption on solid surfaces is complex, potentially involving a variety of primary and secondary effects including structural rearrangements on the surface, cooperative adsorption, overshooting adsorption kinetics, and protein aggregation. The occurrence of protein conformational changes has been shown to occur both on ion exchange chromatography surfaces and on hydrophobic interaction chromatography media and has been found to be responsible for on-column aggregate formation (Guo *et al.*, 2014; Guo and Carta, 2014), multiple peak elution (Guo *et al.*, 2016), and partially irreversible binding (Jungbauer *et al.*, 2005). In this work we did not observe aggregate formation or multiple peak elution, in part because of the lack of hydrophobicity on the CHT surface, which has been shown to play a major role on these effects. We also observed essentially stoichiometric recoveries of our antibody monomer and dimer samples upon elution from either CHT Type I or Type II using, for example 500 mM phosphate as the eluent, either

individually or in mixtures. Nevertheless, as demonstrated below, the experimental results exhibited displacement profiles that were much broader than those predicted assuming complete diffusion control. Moreover, as seen in Figure 4.2 and Figure 4.3, these profiles are asymmetrical suggesting that kinetic effects are at play in addition to diffusional transport limitation. Lundstrom and Elwing (1990) have provided a general framework for the description of these effects using simple kinetic expressions to model the exchange of protein molecules in solution against adsorbed molecules. The key assumption in their framework is that the protein can exist in multiple bound states, which exchange with species in solution at different rates. The physical interpretation of these states varies and is often unknown, although the assumption is often made that the protein unfolds and spreads on the chromatographic surface resulting in strongly or irreversibly bound forms. This type of model, often referred to as "spreading kinetics", has been used previously by several authors to describe protein-surface interactions in different types of systems. For example, Yang and Etzel (2003) modeled the kinetics of single component adsorption of proteins on an anion exchange adsorptive membrane and found that spreading kinetics provided the best fit of asymmetrically skewed breakthrough curves. Because of the membrane format used, mass transfer effects were neglected. Haimer *et al.* (2007) used a spreading model including an irreversibly bound state similar to that of Yang and Etzel to explain the two-peak elution behavior observed for certain proteins in hydrophobic interaction chromatography (HIC). Despite the relatively large size of the chromatographic particles used, these authors also neglected mass transfer effects, suggesting that the overall process was dominated by kinetics and unaffected by mass transfer. McCue *et al.* (2008) developed a model including both mass transfer spreading kinetics to describe the adsorption and elution of antibody monomer and aggregated species on an agarose-based HIC resin. The model used by these

65

authors to describe mass transfer was based on homogeneous diffusion with a driving force written in terms of the adsorbed phase protein concentration. Finally, Diedrich *et al.* (2017) developed a multi-state model which combines a spreading kinetics model with the steric mass action (SMA) model to describe the adsorption of a mAb on ion exchange tentacle resins. The mechanistic basis of such a model is doubtful for these types of resin because of the complex protein-tentacle interactions, but is likely applicable for adsorption on CHT, which is characterized by relatively large pores with a rigid structure.

The kinetic model used in this work, also based on the Lundstrom and Elwing formalism, is illustrated in Figure 4.4 With reference to this figure, we consider two bound states for each protein. The first bound state (shown by white circles and ovals for the monomer and dimer, respectively) is assumed to allow direct exchange with molecules in solution following a second order, competitive Langmuir kinetics. The second bound state (shown by gray circles and ovals for the monomer and dimer, respectively) is assumed to ensue from the first bound state following a reversible first order "spreading" kinetics. We assume that this new bound state is altered in a way that renders it not amenable to direct exchange with molecules in solution. This mechanism is assumed to occur at each point within the particles and is considered along with a description of diffusional transport in the particle pores. A key feature of this model is that, for conditions where adsorption is highly favorable, the spreading step does not affect the overall kinetics, which becomes dependent only on diffusion and Langmuir adsorption kinetics. On the other hand, the spreading kinetics included in this model affects both elution and frontal analysis since both molecules need to pass through the exchangeable bound state in order to desorb or undergo displacement. Intuitively, this mechanism can lead to the reversible, tailing

displacement fronts observed during frontal analysis and, as will be shown later, tailing isocratic

elution peaks
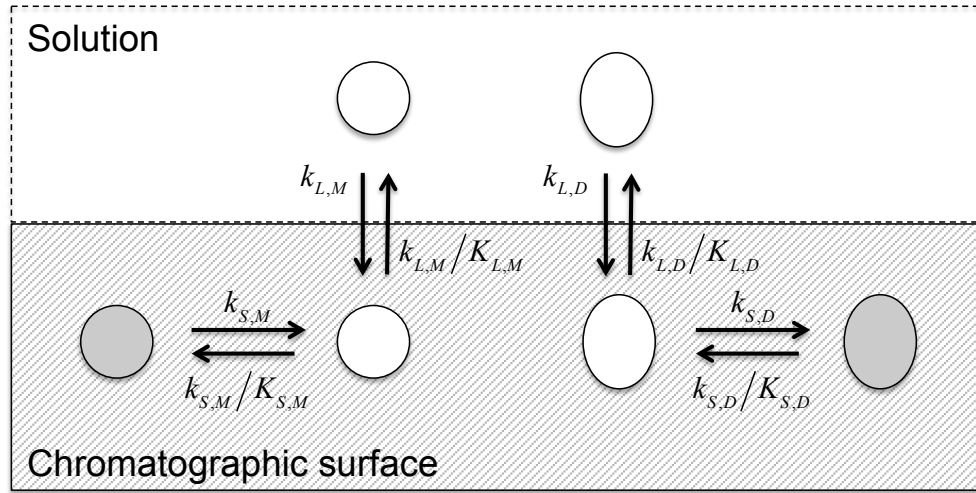
Figure 4.4. Schematic representation of the spreading kinetics model for a two-component system. Circles and ovals represent monomer and dimer, respectively.

The equations describing the kinetic scheme of Figure 4.4 for a monomer/dimer mixture,

including diffusional transport in the particle pores, are as follows:

$$\varepsilon'_p \frac{\partial c_M}{\partial t} + r_{L,M} = \frac{D_{e,M}}{r^2} \frac{\partial}{\partial r}\left(r^2 \frac{\partial c_M}{\partial r}\right) \tag{4.14}$$

$$\varepsilon'_p \frac{\partial c_D}{\partial t} + r_{L,D} = \frac{D_{e,D}}{r^2} \frac{\partial}{\partial r}\left(r^2 \frac{\partial c_D}{\partial r}\right) \tag{4.15}$$

$$\frac{\partial q_{L,M}}{\partial t} = r_{L,M} - k_{S,M}\left(q_{L,M} - \frac{q_{S,M}}{K_{S,M}}\right) \tag{4.16}$$

$$\frac{\partial q_{L,D}}{\partial t} = r_{L,D} - k_{S,D}\left(q_{L,D} - \frac{q_{S,D}}{K_{S,D}}\right) \tag{4.17}$$

$$\frac{\partial q_{S,M}}{\partial t} = k_{S,M}\left(q_{L,M} - \frac{q_{S,M}}{K_{S,M}}\right) \tag{4.18}$$

$$\frac{\partial q_{S,D}}{\partial t} = k_{S,D}\left(q_{L,D} - \frac{q_{S,D}}{K_{S,D}}\right) \tag{4.19}$$

with:

$$r_{L,M} = k_{L,M}\left\{c_M\left[q_{m,M} - \left(q_{L,M} + q_{S,M}\right) - \frac{q_{m,M}}{q_{m,D}}\left(q_{L,D} + q_{S,D}\right)\right] - \frac{q_{L,M}}{K_{L,M}}\right\} \tag{4.20}$$

$$r_{L,D} = k_{L,D}\left\{c_D\left[q_{m,D} - \left(q_{L,D} + q_{S,D}\right) - \frac{q_{m,D}}{q_{m,M}}\left(q_{L,M} + q_{S,M}\right)\right] - \frac{q_{L,D}}{K_{L,D}}\right\} \tag{4.21}$$

In these equations, $q_{L,i}$ and $q_{S,i}$ represent the concentrations of protein that are, respectively, in the bound state that is directly exchangeable with molecules in solution and in the bound state that is not directly exchangeable, $r_{L,i}$ represents the rate of exchange with molecules in solution according to the Langmuir model, and $k_{S,i}$ and $K_{S,i}$ are, respectively, the rate and equilibrium constants for the reversible conversion between the two bound states. Note that these equations assume that the two bound states occupy the same surface area, but this assumption can be relaxed with a minor modification of the model equations to describe other cases (Lundström and Elwing, 1990).

According to this model, adsorption equilibrium is described by the following equations:

$$q_{L,M} = \frac{q_{m,M}K_{L,M}C_M}{1 + K_{L,M}\left(1 + K_{S,M}\right)C_M + K_{L,D}\left(1 + K_{S,D}\right)C_D} \tag{4.22}$$

$$q_{L,D} = \frac{q_{m,D}K_{L,D}C_D}{1 + K_{L,M}\left(1 + K_{S,M}\right)C_M + K_{L,D}\left(1 + K_{S,D}\right)C_D} \tag{4.23}$$

68

$$q_M = q_{L,M} + q_{S,M} = \frac{q_{m,M} K_{L,M} \left(1 + K_{S,M}\right) C_M}{1 + K_{L,M} \left(1 + K_{S,M}\right) C_M + K_{L,D} \left(1 + K_{S,D}\right) C_D} \tag{4.24}$$

$$q_D = q_{L,D} + q_{S,D} = \frac{q_{m,D} K_{L,D} \left(1 + K_{S,D}\right) C_D}{1 + K_{L,M} \left(1 + K_{S,M}\right) C_M + K_{L,D} \left(1 + K_{S,D}\right) C_D} \tag{4.25}$$

where q_M and q_D are the total concentration of bound monomer and bound dimer, respectively, including both bound states.

Since the full model including both Langmuir kinetics and spreading kinetics would involve the simultaneous determination of many parameters, only two limiting cases are considered in this work, namely pore diffusion combined with Langmuir kinetics only, and pore diffusion combined with spreading kinetics only. The latter is obtained when $q_{L,M}$ and $q_{L,D}$ are in equilibrium with the local composition in the pore liquid, c_M and c_D. The model equations for the first of these two cases are obtained by setting $k_{S,i} = K_{S,i} = 0$ for $i =$ M, D in Eqs. (4.14)-(4.21), while the model equations for the second case are as follows:

$$\varepsilon_p' \frac{\partial c_M}{\partial t} + \frac{\partial q_{L,M}}{\partial t} + r_{S,M} = \frac{D_{e,M}}{r^2} \frac{\partial}{\partial r} \left(r^2 \frac{\partial c_M}{\partial r} \right) \tag{4.26}$$

$$\varepsilon_p' \frac{\partial c_D}{\partial t} + \frac{\partial q_{L,D}}{\partial t} + r_{S,D} = \frac{D_{e,D}}{r^2} \frac{\partial}{\partial r} \left(r^2 \frac{\partial c_D}{\partial r} \right) \tag{4.27}$$

$$\frac{\partial q_{S,M}}{\partial t} = r_{S,M} \tag{4.28}$$

$$\frac{\partial q_{S,D}}{\partial t} = r_{S,D} \tag{4.29}$$

With

$$r_{S,M} = k_{S,M} \left(q_{L,M} - \frac{q_{S,M}}{K_{S,M}} \right) \tag{4.30}$$

$$r_{S,D} = k_{S,D}\left(q_{L,D} - \frac{q_{S,D}}{K_{S,D}}\right) \tag{4.31}$$

and

$$\frac{\partial q_{L,M}}{\partial t} = \frac{\partial q_{L,M}}{\partial c_M}\frac{\partial c_M}{\partial t} + \frac{\partial q_{L,M}}{\partial c_D}\frac{\partial c_D}{\partial t} \tag{4.32}$$

$$\frac{\partial q_{L,D}}{\partial t} = \frac{\partial q_{L,D}}{\partial c_M}\frac{\partial c_M}{\partial t} + \frac{\partial q_{L,D}}{\partial c_D}\frac{\partial c_D}{\partial t} \tag{4.33}$$

where the partial derivatives in Eqs. (4.32) and (4.33)are evaluated from Eq. (4.22) and (4.23).

Analytical solutions of these equations are only possible for the linear isotherm case. For the

general case, a numerical solution was obtained for Eqs. (4.4)-(4.7) combined with: (a) Eqs.

(4.8)-(4.13) for the case pore diffusion without kinetic resistance; (b) Eqs. (4.14)-(4.21) with

$k_{S,i} = K_{S,i} = 0$ with i = M, D for the case of pore diffusion combined with Langmuir kinetics; and

(c) Eqs. (4.26)-(4.33) for the case of pore diffusion combined with spreading kinetics. In all three

cases, the axial dispersion term was set to zero and the spatial derivative $\partial C_i / \partial x$ was

approximated by Euler backwards finite differences method. This method introduces numerical

dispersion, which was used to simulate axial dispersion by using a number of discretization

points equal to the number of plates, $N=L$/HETP, determined from a pulse injection of the

protein under non-binding conditions extrapolated to zero velocity according to the van

Deemeter equation according to our previous data (Figure 3.3). Radial derivatives were also

discretized by finite differences resulting in a system of ordinary differential equations that, in

turn, was solved using *ode15s* in MATLAB R2017b (The Mathworks, Natick, MA, USA). The

number of radial discretization points was set sufficiently large that increasing it further did not

significantly affect the numerical results.

The model equations above are greatly simplified if the isotherms are assumed to be linear and non-competitive, with the following equations replacing Eqs. (4.24) and (4.25):

$$q_M = q_{m,M}K_{L,M}\left(1+K_{S,M}\right)C_M \tag{4.34}$$

$$q_D = q_{m,D}K_{L,D}\left(1+K_{S,D}\right)C_D \tag{4.35}$$

This result is approximated at relatively high Na^+ concentrations, when protein binding to the CHT surface is weak. Analytical solutions for this case are easily found in the Laplace domain and expressions for the moments of the isocratic elution peak obtained from a pulse injection are given in the Appendix. The corresponding first moment, HETP, and peak skew including pore diffusion and first order reversible spreading kinetics are found from the moments and are as follows:

$$\mu_1 = \frac{L}{v}\left(1+k'\right) \tag{4.36}$$

$$H = \frac{2D_L}{v} + \frac{2v}{\phi}\left\{\left(\frac{k'}{1+k'}\right)^2\frac{r_p^2}{15D_e} + \left(\frac{\phi q_m K_L K_S}{1+k'}\right)^2\frac{1}{q_m K_L}\frac{1}{k_S}\right\} \tag{4.37}$$

Peak skew =

$$\frac{\dfrac{2L}{105v^5}\left\{\begin{array}{c}\dfrac{2r_p^4 v^4 k'^3}{D_e^2\phi^2} + \dfrac{42r_p^2 v^2 k'\left[v^2 K_L K_S^2 q_m + D_L k_S k'\left(1+k'\right)/\phi\right]}{D_e k_S} \\[4mm] + \dfrac{315\left[v^4\phi K_L K_S^3 q_m + 2v^2\phi D_L k_S K_L K_S^2 q_m\left(1+k'\right) + 2D_L^2 k_S^2(1+k')^3\right]}{k_S^2}\end{array}\right\}}{\left\{\dfrac{2Lr_p^2 k'^2}{15D_e v\phi} + \dfrac{2L}{k_S v^3}\left[v^2\phi K_L K_S^2 q_m + D_L k_S\left(1+k'\right)^2\right]\right\}^{\frac{3}{2}}} \tag{4.38}$$

where, for simplicity, the subscript i, identifying the component, has been dropped. In these expressions μ_1 is the first moment of the eluted peak, μ_2' and μ_3' are the second and third central

moments (Eqs. (7.22)-(7.24)), $\phi = (1-\varepsilon)/\varepsilon$, and $k' = \phi\left[\varepsilon'_p + q_m K_L\left(1+K_S\right)\right]$ is the retention factor.

The limiting case of these equations for pore diffusion only is found by setting $k_S = \infty$ or $K_S = 0$.

Table 4.2. Rate parameters used in frontal analysis calculations. Effective pore diffusivities, D_e, are in 10^{-7} cm^2/s. Rate constants for the Langmuir kinetics model, $k_{L,i}$, are in mL mg^{-1} s^{-1}. Rate constants for the spreading kinetics model, $k_{S,i}$, are in s^{-1}.

CHT Type I		
	20 mM Na$^+$	70 mM Na$^+$
$D_{e,M}$	0.13*	0.58
$D_{e,D}$	0.08*	0.10
$k_{L,M}$	5.52	1.27
$k_{L,D}$	1.40	9.32
$K_{S,M}$	1.3	0.5
$K_{S,D}$	1.2	0.5
$k_{S,M}$	1.8×10^{-4}	1.2×10^{-4}
$k_{S,D}$	4.5×10^{-3}	1.8×10^{-3}

CHT Type II			
	20 mM Na$^+$	70 mM Na$^+$	100 mM Na$^+$
$D_{e,M}$	1.1*	1.2	1.2
$D_{e,D}$	0.78*	0.78	0.78
$k_{L,M}$	0.03	0.05	0.02
$k_{L,D}$	1.30	0.10	0.17
$K_{S,M}$	2.7	0.2	0.1
$K_{S,D}$	11.3	4.5	2.9
$k_{S,M}$	1.5×10^{-4}	3.7×10^{-3}	1.8×10^{-5}
$k_{S,D}$	7.8×10^{-4}	1.3×10^{-3}	7.5×10^{-4}

*Data from Chapter 3

4.5 Modeling results

4.5.1 Frontal analysis

Three different cases were considered to model the frontal analysis results – pore diffusion only without kinetic resistances, pore diffusion with Langmuir kinetics only, and pore diffusion with spreading kinetics only. For the first of these three cases, the calculations were done without adjusting any parameters using the experimentally determined isotherm parameters and the effective pore diffusivities from our prior work summarized in Table 4.1 and Table 4.2. For the other two cases, we used the same isotherm and effective pore diffusivities but determined best-fit values of the rate parameters $k_{L,M}$ and $k_{L,D}$ for the Langmuir kinetics model as well as $K_{S,M}$, $K_{S,D}$, $k_{S,M}$ and $k_{S,D}$ for the spreading kinetics model at each Na$^+$ concentration. In each case, optimization of parameter values was done with the MATLAB nonlinear least squares function, *lsqnonlin*, which uses a steepest descent algorithm. Fitting the monomer/dimer displacement profiles only (instead of both pure monomer and monomer/dimer displacement fronts) proved easier to implement since the pure monomer front is very steep and even small horizontal deviations between experimental and predicted fronts resulted in unreasonable error estimates. A few test calculations considering both monomer and dimer profiles resulted in similar overall fits. Table 4.2 provides a summary of the parameters determined in this manner. Figure 4.5 compares the experimental results with calculates profiles based on the pore diffusion model without kinetic resistances, the pore diffusion combined with Langmuir kinetics, and the pore diffusion combined with spreading kinetics for CHT Type I and Type II at 20 and 70 mM Na$^+$. For these calculations the effective diffusivities were, in all three cases, those obtained from single component adsorption experiments while the constants in the kinetics expressions were regressed to the data. As seen in Figure 4.5a and b, the experimental CHT Type I curves are very

73

close to those predicted by the pore diffusion model without any kinetics resistance. This occurs because of the small pore size of this material which results in relatively small effective pore diffusivities and, thus, a dominance of mass transfer effects. Slightly better agreement is found in this case with either the fitted Langmuir kinetics model or the spreading kinetics model, but it is evident that the additional resistance associated with these kinetics effects is small. On the other hand, as seen in Figure 4.5c and d, the difference between the CHT Type II experimental results and those predicted assuming pore diffusion only is quite large, especially at 20 mM Na^+. In this case, both kinetic models provide a description that is much closer to the experimental data. This is especially true for the spreading kinetics model that is able to describe the asymmetrically tailing displacement front observed at this low Na^+ concentration. For these conditions, the best-fit Langmuir kinetics model predicts a more monotonically curved displacement than is seen experimentally. On the other hand, the spreading kinetics model correctly describes the initially sharp displacement front followed by a long tail. The difference between the two kinetics models disappears, however, at the higher Na^+ concentration of 70 mM, which resulted in a steeper and more symmetrical displacement front. It should be noted that despite the added kinetics resistances, the CHT Type II curves are still, on the whole, considerably steeper than those observed for Type I because the diffusional resistance in the former material is smaller as a result of its larger pore size.

Figure 4.6a shows experimental results for CHT Type II at 100 mM Na^+ along with model calculations using fitted rate parameters. For these conditions, the displacement front becomes much more symmetrical and even closer to the diffusion-controlled case making Langmuir and spreading kinetics models essentially indistinguishable from each other. Figure 4.6b shows model predictions compared to experimental results at 70 mM Na^+ with a shorter residence time

74

and a lower aggregate feed content using the rate parameters fitted to the data in Figure 4.5d. These data are used as a test case to illustrate the ability of the model to predict the separation for conditions outside those used to determine the model parameters. In this case, both Langmuir and spreading kinetics models, using the same parameters determined for the conditions of Figure 4.5d, are able to predict quantitatively the experimental profiles. However, as shown below, only the spreading model can also simultaneous predict the intraparticle profiles and is, thus, more physically realistic. In this respect, we also attempted to describe the frontal analysis data with the pore diffusion model without kinetic resistances using the fitted effective diffusivities instead of the independently determined ones. In this case, although a good agreement could be found with the Type I results, only a rough agreement could be found for Type II especially at 20 mM Na^+ as seen in Figure 4.7. In this case, not only was the predicted shape of the displacement front inaccurate, but the D_e-values needed to fit the experimental profiles were 4 to 10 times smaller than those determined independently for the pure components.
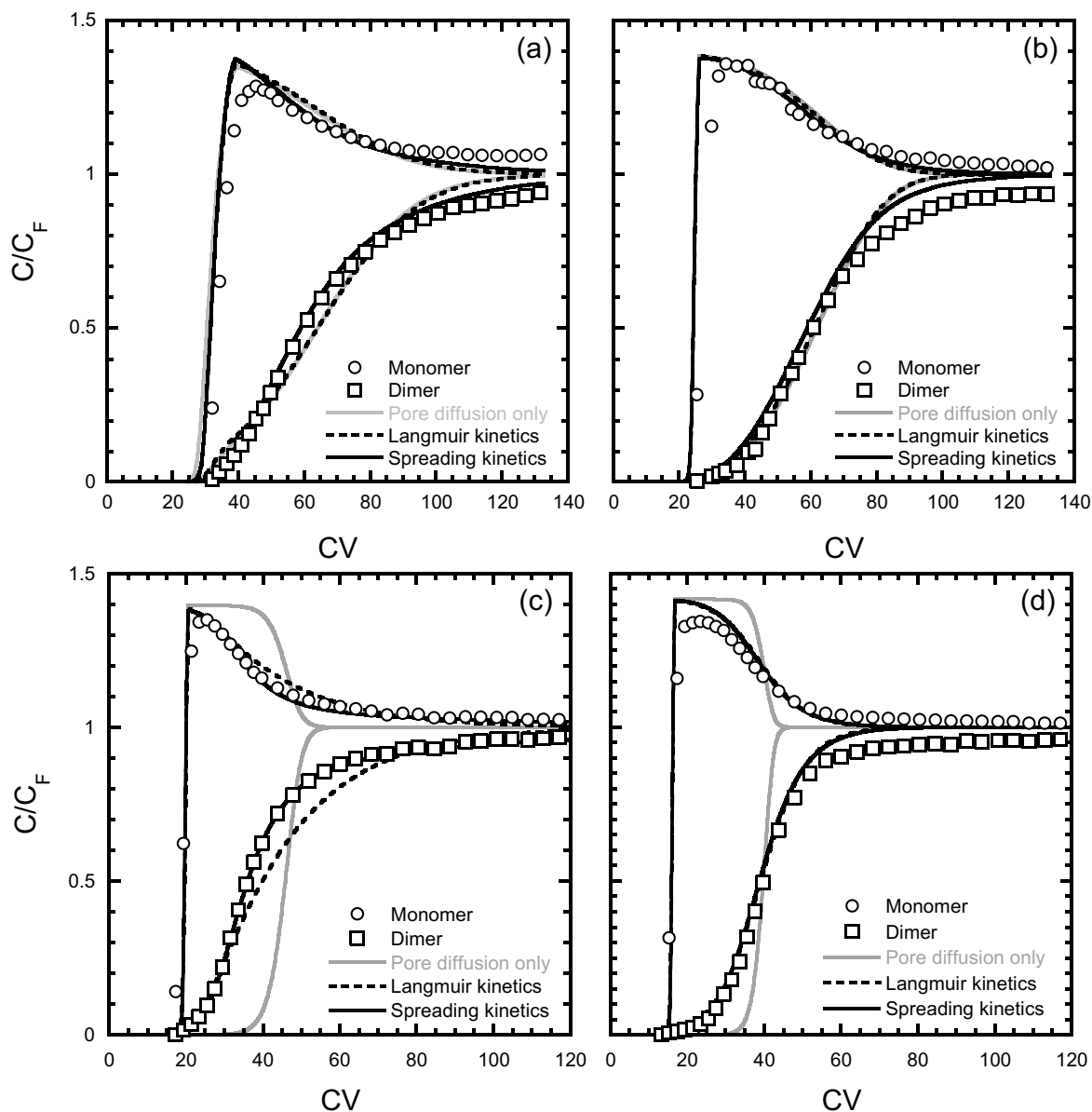
Figure 4.5. Comparison of monomer-dimer binary breakthrough curves with calculations based on the pore diffusion model (solid grey lines), the pore diffusion model with Langmuir kinetics (dashed lines), and the pore diffusion model with spreading kinetics (solid black lines) using the two-component Langmuir isotherm (Eqs. (4.1)-(4.33)) to describe competitive binding. Experimental conditions are the same as in Figure 4.2. The rate constants and effective diffusivities used in the numerical calculations are listed in Table 4.2.
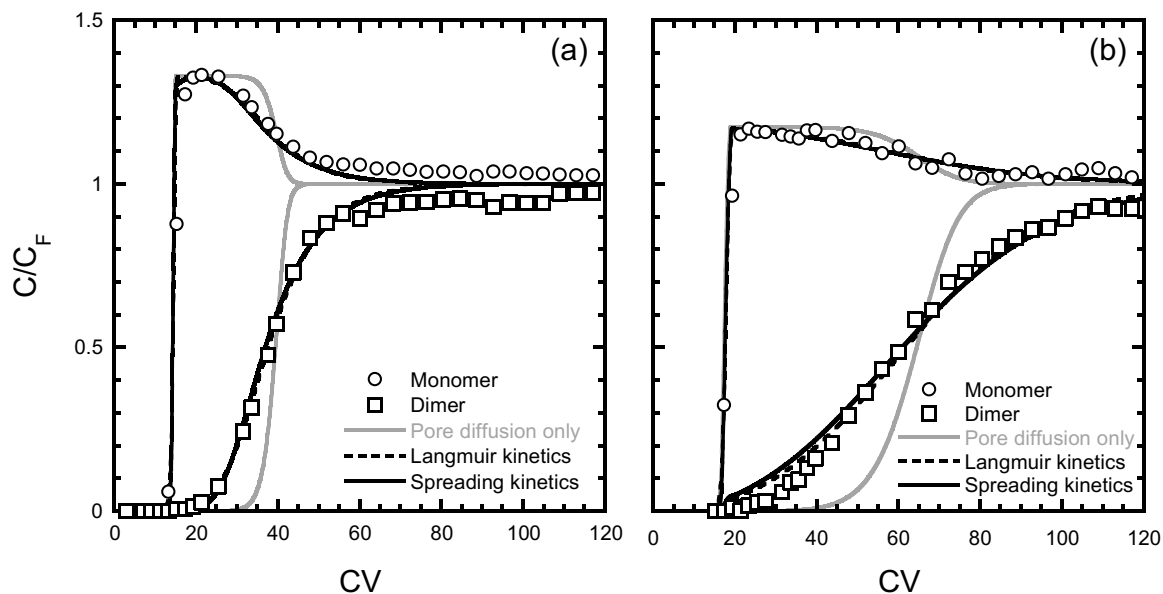
Figure 4.6. Comparison of monomer-dimer binary breakthrough curves with predictions based on pore diffusion model (solid grey lines), the pore diffusion model with Langmuir kinetics mode (dashed lines), and the pore diffusion model with spreading kinetics model (solid black lines) using the two-component Langmuir isotherm (Eqs. (4.1)-(4.33)) to describe competitive binding of monomer and dimer. Experimental conditions are the same as in Figure 4.3. The rate constants and effective diffusivities are listed in Table 4.2.
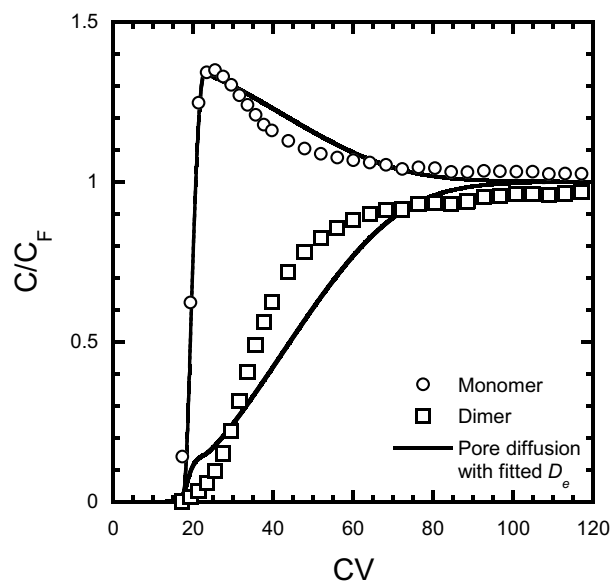
Figure 4.7. Comparison of monomer-dimer binary breakthrough curves with model calculations based on the pore diffusion model without kinetic resistances using the two-component Langmuir isotherm and fitted effective diffusivity values. The fitted D_e values are 2.8×10^{-8} and 6.7×10^{-9} cm^2/s for monomer and dimer, respectively. Experimental conditions are the same as in Figure 4.2c.

The fitted kinetic rate parameters values are summarized in Table 4.2. For CHT Type I, essentially identical numerical results are obtained with or without a kinetic resistance since pore diffusion is dominant. For CHT Type II, on the other hand, where pore diffusion is faster, including a kinetic resistance is needed to describe the experimental behavior. In this case, a much better fit of the experimental results is obtained with the spreading kinetics model, particularly at low Na^+ concentration where binding is stronger. Increasing the salt concentration and, thus, reducing the binding strength, reduces the difference between the two kinetic models. As seen in Table 4.2, no particular trend relative to Na^+ concentration is seen for the rate parameters $k_{L,M}$ and $k_{L,D}$ in the Langmuir kinetics model. On the other hand, the equilibrium constants $K_{S,M}$ and $K_{S,D}$ in the spreading kinetics model decrease steadily with Na^+ concentration suggesting that the tendency for the protein to spread on the CHT surface becomes less pronounced when binding becomes weaker. As indicated by the numerical values, this effect appears to be especially pronounced for the dimer.

4.5.2 Isocratic elution

These experiments had two principal goals. The first was to help determine whether the kinetic resistance is caused exclusively associated with the monomer-dimer displacement or it can also affect the elution behavior of each individual species. The second goal was to determine if the same model that best describes the frontal analysis behavior could also be used to describe the isocratic elution behavior in the linear region of the isotherm attained at relatively high Na^+ concentrations. For these conditions the analytical solution of the equations describing the case of pore diffusion with spreading kinetics could be used directly to determine the model parameters by matching the experimental first moment, the HETP, and the peak skew values with those predicted by Eqs.(4.35)-(4.37), independently for the monomer and for the dimer.

Since the D_e-values are known, the model parameters for each component are q_mK_L, k_S, and K_S. In order to circumvent the difficulties encountered with the direct computation of moments, HETP, and peak skew, they were obtained for each condition by fitting the exponentially modified Gaussian (EMG) function to the eluted peaks and using the expressions provided in ref. (Grushka, 1972) to calculate the moments. An example is shown in the section 7.3 in Appendix. q_mK_L, k_S, and K_S were then calculated based on Eqs. (4.35)-(4.37) using the known D_e-values. Figure 4.8 compares the isocratic elution model and data. The corresponding first moment, HETP, and peak skew values are given in Table 4.3 along with the model parameters based on the experimental values. Linear isotherm conditions were checked by injecting different amounts of protein and verifying that there was no effect on the peak shape (results not shown for brevity). As seen in Figure 4.8a and in Table 4.3, the HETP increases only slightly when the Na^+ concentration is decreased for the monomer on CHT Type I. In this case, the experimental peaks are in very close agreement with predictions based on pore diffusion only suggesting that kinetics effects are insignificant. A larger contribution of kinetic effects can be seen for the dimer on CHT Type I (Figure 4.8b), for the monomer of CHT Type II (Figure 4.8c), and, especially, for the dimer on CHT Type II (Figure 4.8d). These effects become more important as the Na^+ concentration is reduced and the binding strength increases. As seen in Figure 4.8d for the dimer on CHT Type II, the elution peak becomes highly asymmetrical and very broad compared to predictions based on pore diffusion alone. The values of parameters of the spreading kinetics model (including pore diffusion) provide some useful clues. Retention, of course, increases at the Na^+ concentration is reduced, which is reflected in the increasing values of q_mK_L. However, K_S, also increases substantially as the Na^+ concentration is reduced and binding becomes stronger. In agreement with the results obtained by fitting the full model to the frontal analysis data, this

result suggests again that the tendency to spread on the CHT surface increases as binding becomes stronger especially for the dimer. k_S remains, however, relatively constant with Na^+ concentration, indicating that the equilibrium distribution of the different bound states is the principal driver of the experimentally observed peak skewness at low Na^+ concentrations. As seen in Figure 4.8, peak shapes calculated using the parameters in Table 4.3 and the numerical solution of the model equations are in good agreement with the experimental peaks, further corroborating the validity of the model.
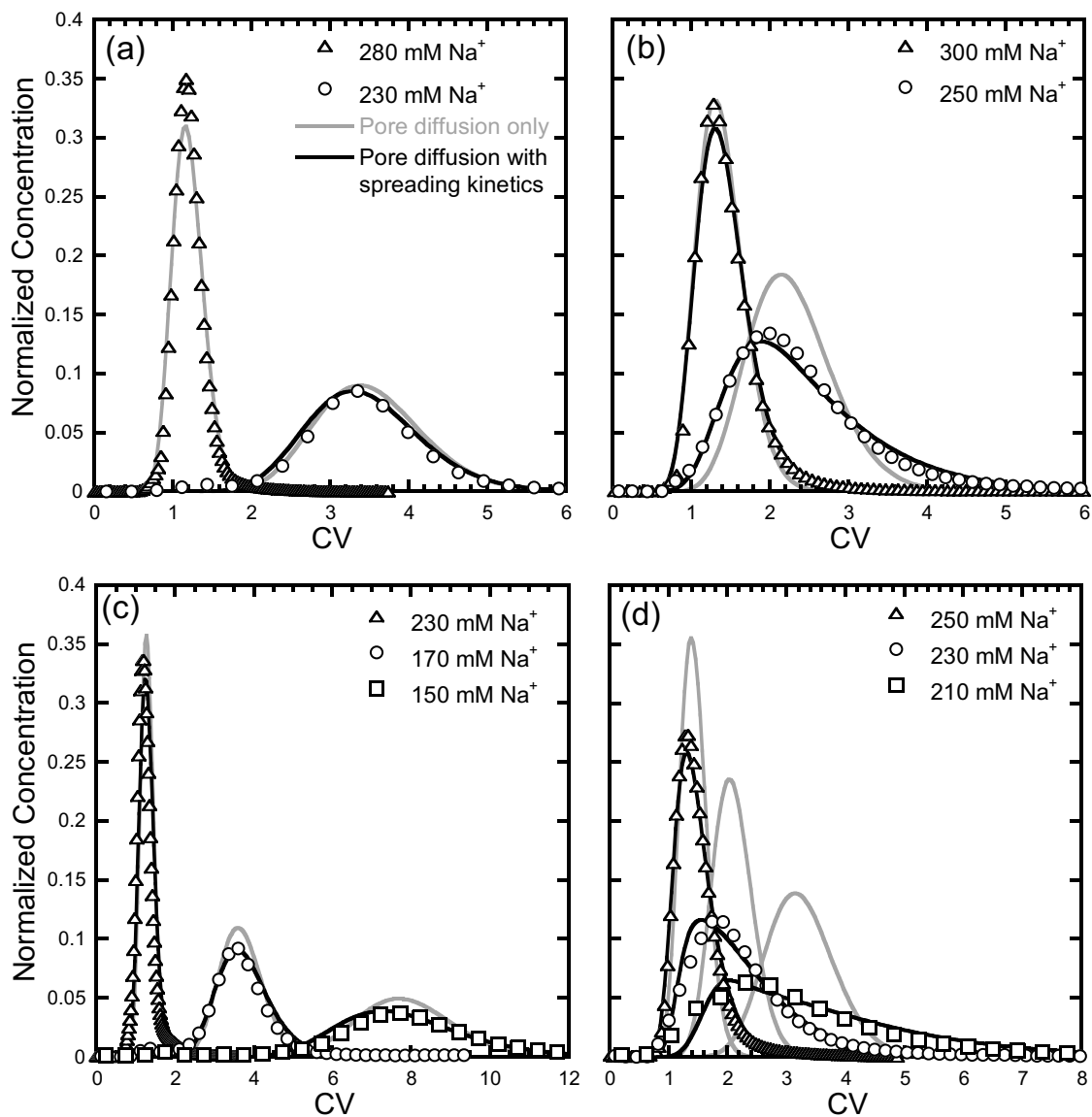
Figure 4.8. Isocratic elution profiles on CHT Type I (a, b) and CHT Type II (c, d) for the mAb monomer (a, c) and dimer (b, d) obtained at different Na$^+$ concentrations in sodium phosphate buffers containing different Na$^+$ concentrations at pH 7.

Table 4.3. Parameters for pore diffusion plus spreading kinetics model based on the moments of the isocratic elution peaks. Effective pore diffusivities used in these calculations were 5.4×10^{-8} and 9.4×10^{-8} cm^2/s for the monomer in CHT Type I and Type II, respectively, and 3.3×10^{-8} and 6.6×10^{-8} cm^2/s for the dimer in CHT Type I and Type II, respectively based on the data in Chapter 3. The axial dispersion contribution to HETP was $2D_L/v = 0.037$ cm for both columns (Wang and Carta, 2019).

CHT Type I							
	Na$^+$ (mM)	Exp. μ_1 (s)	Exp. HETP (cm)	Exp. Peak skew	$q_m K_L$	k_S (s^{-1})	K_S
Monomer	280	480	0.16	0.39	0.77	ND[*]	ND[*]
	230	1410	0.34	0.79	3.99	5.4×10^{-5}	0.015
Dimer	300	550	0.52	1.26	1.00	6.3×10^{-4}	0.076
	250	920	1.17	1.32	1.59	3.0×10^{-3}	0.49
CHT Type II							
	Na$^+$ (mM)	Exp. μ_1 (s)	Exp. HETP (cm)	Exp. Peak skew	$q_m K_L$	k_S (s^{-1})	K_S
Monomer	230	520	0.17	0.79	0.79	6.3×10^{-4}	0.039
	170	1470	0.27	0.78	3.88	6.8×10^{-4}	0.083
	150	3200	0.35	0.80	9.02	5.7×10^{-4}	0.15
Dimer	250	580	0.48	1.23	0.77	5.2×10^{-3}	0.37
	230	850	1.38	1.40	0.93	7.1×10^{-3}	1.16
	210	1320	1.98	1.43	1.57	4.4×10^{-3}	1.32

[*] Experimental HETP was consistent with pore diffusion only.

4.5.3 Intraparticle concentration profiles for batch adsorption

The goal of these experiments was to determine whether the same models used to fit the frontal analysis results could predict the intraparticle concentration profiles determined during batch co-adsorption by CLSM. As noted, for example, in Chapter 3, for favorable adsorption isotherms, intraparticle concentration profiles are usually more sensitive to the nature of the assumed rate model compared to the breakthrough curves obtained from a column. This occurs because the batch measurements are not influenced by column dynamics or axial dispersion. Thus, they are essentially exclusively representative of equilibrium and rate effects.

In order to compare experimental and predicted profiles for these conditions, our previously obtained CLSM images for co-adsorption of monomer-dimer mixtures shown in Figure 3.6 and Figure 3.7 were digitized and converted to the individual monomer and dimer concentration profiles at representative time points. Since the experiments were done with a relatively low protein concentration (0.5 mg/mL each for monomer and dimer), the ensuing profiles reflect almost exclusively the bound protein concentration. Predicted profiles were obtained from the numerical solution of the same three models considered for the description of frontal analysis – pore diffusion only, pore diffusion with Langmuir kinetics, and pore diffusion with spreading kinetics – using the same equilibrium and rate parameters used to model the frontal analysis results as summarized in Table 4.1 and Table 4.2. Figure 4.9 shows the results for CHT Type I and Type II. We focused on the 20 mM Na^+ case since this gave the largest differences between the different models in the frontal analysis experiments. As seen in this figure, the experimental CHT Type I concentration profiles are relatively sharp and in close agreement with those predicted by all of the three models. This result is expected because of the small effective diffusivity in this small pore material which results in a nearly completely mass transfer-

83

controlled process. On the other hand, the experimental profiles observed for CHT Type II are comparatively smoother and deviate substantially from those predicted without accounting for any kinetic resistance. As seen in this figure, the Langmuir kinetics model cannot predict the intraparticle behavior for these conditions. Much closer agreement is seen between the experimental profiles and those predicted by combining pore diffusion and spreading kinetics. Since the rate parameters used were the same that matched the frontal analysis data, this result supports the mechanistic validity of this model.
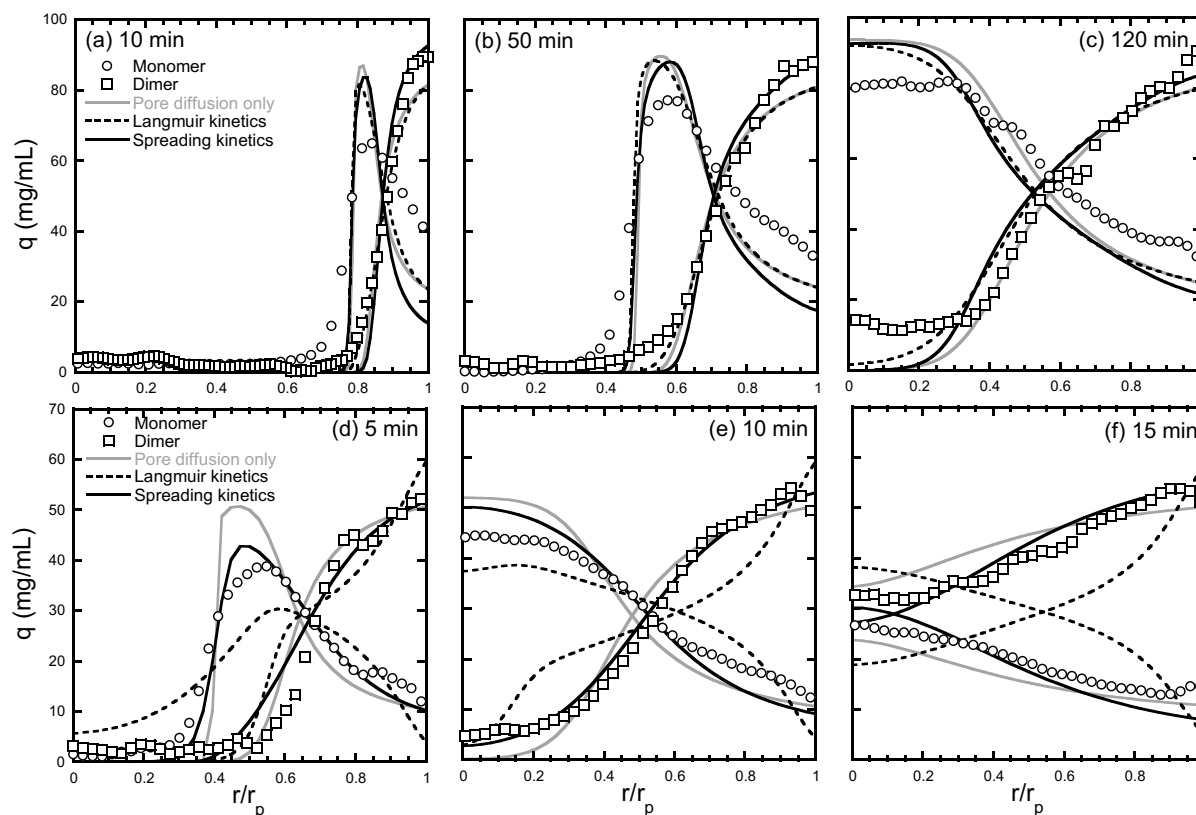
Figure 4.9. Comparison of experimental and predicted intraparticle concentration profiles during co-adsorption of a 1 mg/mL monomer-dimer mixture containing 50% dimer in a 10 mM Na_2HPO_4 buffer at pH 7. Confocal microscopy images are from Figure 3.6 and Figure 3.7. Circles and squares are the normalized fluorescence intensity profiles of the monomer and dimer, respectively. Lines are model predictions based on the pore diffusion model (solid grey lines), the pore diffusion model with Langmuir kinetics (dashed lines), and the pore diffusion model with spreading kinetics (solid black lines) using the parameters listed in Table 4.2.

Chapter 5 Gradient Separation for the Monoclonal Antibody Monomer-dimer on Ceramic Hydroxyapatite

5.1 Introduction

As discussed in Chapter 1, hydroxyapatite (HAP) is a multimodal adsorbent that contains positively charge binding sites as well as negatively charged binding sites. Due to this unique surface chemistry, HAP is considered as one of the most effective chromatographic purification materials for complex biopharmaceuticals, such as monoclonal antibodies (mAbs). As shown in Chapter 4, CHT is effective for aggregate removal from mAbs when operated in a frontal analysis mode.

Aggregate removal with CHT has also been reported when operating in a bind-elute mode, especially with gradient elution separation, by several authors. For example, Sun *et al.* (2016) used both sodium chloride gradients and sodium phosphate gradients to remove high molecular weight (HMW) molecules from a mAb monomer. Morrison *et al.* (2011) used NaCl gradients with CHT columns in combination with selective desorbents, such as bekanamycin sulfate and spermine, to improve yield from 61-79% to 100%. Among these examples, both sodium phosphate and sodium chloride gradients have been observed to be effective. However, using NaCl gradients with CHT columns in a process setting is problematical from a practical point of view. As discussed by Bankston *et al.* (2010), NaCl gradients generate pH transitions within CHT columns that results from the exchange of sodium ions and protons on the CHT surface. Increasing the Na^+ concentration releases protons and lowers the pH. In turn, this can lead to irreversible damage to the HAP particles since HAP becomes soluble at pH values below about 6.5. Special buffers, such as MES, which is a zwitterionic buffering agent and, thus, provides a high buffering capacity without greatly affecting ionic strength, can be used to modulate these

pH transitions but are expensive and not used in practice. For this reason, phosphate gradients are more commonly used with CHT columns.

Since mAb can be purified using CHT by frontal analysis and gradient elution, a remaining question is how to choose an appropriate modality. To answer that question, a comparison of mAb monomer-dimer separations using frontal analysis and those using a bind-elute process was conducted in this chapter. This comparison is made based on predictions with a mechanistic model validated through experimental measurements in order to be able to explore broad ranges of operating conditions. As discussed in Chapter 3, a detailed mechanistic model has already been developed for frontal analysis. A similar model is developed and validated in this chapter to predict the gradient elution behaviors.

The main difference between modeling frontal analysis and modeling gradient elution is that, for frontal analysis, one only needs to know the two-component isotherm at the particular salt concentration at which the separation occurs. On the other hand, for gradient elution, the isotherm needs to be known as a function of salt concentration. This is not always straightforward. For example, the commonly used Langmuir isotherm has coefficients that change with salt concentration. However, the dependence of these parameters on salt concentration is not known theoretically. The steric mass action (SMA) law (Brooks and Cramer, 1992) is also frequently used to describe protein ion exchange equilibrium. This model includes a theoretical dependence on salt concentration. However, this model does not always agree with experienced trends. For example, the SMA model predicts higher selectivity on cation exchangers for the dimer in a monomer-dimer mixture at low salt concentrations than at high salt concentration, but Reck et al. (2017) observed experimentally the opposite effect of salt concentration. Recently, Creasy et al. (2018) introduced an empirical interpolation (EI) method

to interpolate protein isotherm at different salt concentrations without using any specific isotherm model. This method requires a large set of data points at several protein and salt concentrations to interpolate the whole isotherm within a chosen salt range. This EI method has been used successfully to predict a mAb monomer-dimer separation for a bind-elute process on the cation exchanger, Nuvia HR-S.

The goals of this chapter are, thus, three-fold. The first goal is to compare experimentally the ability of CHT to separate mAb monomer-dimer mixtures using either a sodium chloride gradient or a sodium phosphate gradient. The second is to develop a model to describe the elution behavior based on the EI method. The final goal is to compare linear gradient elution with frontal analysis in terms of yield and productivity using model predictions.

5.2 Materials and methods

5.2.1 Materials

CHT samples used in this chapter were as same as those described in Chapters 2-4 and were obtained from Bio-Rad Laboratories (Hercules, CA, USA) with a 40 μm nominal particle diameter. The monoclonal antibody sample used in this work was a mixture of stable monomer (~68%) and dimer (~32%) described in Chapter 3-4 and were provided by MedImmune (Gaithersburg, MD, USA). All other chemicals were purchased from Thermo Fisher Scientific (Waltham, MA, USA) and MilliporeSigma (St. Louis, MO, USA). Isolated monomer or dimer samples were prepared as described in Chapter 3 and 4 and also as described in Reck *et al.* (2015).

5.2.2 Adsorption measurements

Some additional adsorption equilibrium isotherm measurement were conducted to supplement the data presented in Chapter 3 and 4 by extending the range of salt concentrations used. Adsorption isotherms were obtained by mixing weighed amounts of CHT with precisely measured volumes of solutions containing different initial protein concentrations for a period of 24 hours and then measuring the final protein concentration in solution. The amount adsorbed was obtained by material balance and normalized by the volume of CHT particles. For two-component adsorption, the residual monomer and dimer concentration ratios were determined by size exclusion chromatography using same method described in Chapter 3.

5.2.3 Column experiments

All the column experiments were conducted with 10 ×100 mm Tricorn columns from GE Healthcare (Pittsburgh, PA, USA) using an AKTA Pure system also from GE Healthcare (Pittsburgh, PA, USA). The columns were flow packed while laterally tapping them sharply until a stable bed height was observed. Column volumes were 6.60 mL and 6.68 mL for CHT Type I and Type II, respectively.

For low protein load single component linear gradient elution (LGE) experiments, 100 μL of solution containing 5 mg/mL mAb were injected into the column and eluted with 5, 10, 15, 25 and 40 CV gradients from 10 to 500 mM Na_2HPO_4 at pH 7.0. The salt concentration at elution, $C_{Na^+}^E$ was determined from the conductivity at the maximum of the eluted peak. A calibration curve was generated to convert the conductivity to Na_2HPO_4 concentration.

For the two-component LGE experiments, protein sample volumes ranging from 1 to 26 mL were loaded using either a 1 mL loop or a 50 mL superloop (GE Healthcare) to obtain total protein

loadings ranging from 0.8 to 30 mg per mL of column volume. In each case, the feed contained approximately 30% dimer. The column effluent was collected in 0.5 mL fractions, which were analyzed by analytical SEC as described in previous chapters. For both low protein load and high protein load experiments, the flow rate was 1 mL/min, corresponding to a residence time of about 6.6 min. After elution, the column was stripped with 500 mM Na_2HPO_4 and regenerated with 10 mM Na_2HPO_4 at pH 7.0.

The adsorption of sodium phosphate on the CHT particles was measured through injections of 100 μl of solutions containing 500 mM Na_2HPO_4 in running buffers containing different phosphate concentrations between 40 to 300 mM Na_2HPO_4. These experiments were also operated at 1 mL/min flow rate.

5.3 Model development

5.3.1 Adsorption equilibria

Several isotherm models are available including the Langmuir isotherm, the stoichiometric displacement (SD) model and the steric mass action (SMA) law model (Brooks and Cramer, 1992). In all these cases, the accuracy of the model is limited by the underlying assumptions. An alternative to using such a thermodynamics-based model is to use adsorption isotherm data directly through a statistical correlation of a suitably grained and extensive data base. While this approach requires a large amount of equilibrium data, it avoids any pitfall associated with the simplifying assumptions that are inherent in thermodynamics-based models. Once adsorption equilibrium data are obtained and correlated with suitable interpolation functions, these empirically based predictions of competitive binding as a function of salt concentration can be combined with a mechanistic description of adsorption/desorption kinetics and of column dynamics to arrive at an overall prediction of column behaviors. This approach is, thus, a

"hybrid" of empirical functions to correlate adsorption equilibrium and mechanistically-based functions to prediction transport and column dynamics.

In this work, we use the empirical interpolation (EI) method developed by Creasy *et al.* (2018) to interpolate adsorption equilibrium data obtained over a broad range of conditions. In particular, this method applies interpolating polynomials to predict competitive binding as a function of salt concentration. The first step of the EI method is to fit binary adsorption isotherm data at different salt concentrations with a multicomponent Langmuir isotherm model according to the following equation:

$$q_i = \frac{q_{m,i} K_i C_i}{1 + K_M C_M + K_D C_D} \tag{5.1}$$

The fitted isotherms can be used to calculated values of q'_M and q'_D at values of C_M and C_D at each salt concentration. This calculation is done for different salt concentrations where experimental data are available. Interpolation polynomials are then used to correlate the q'_M and q'_D values as a function of salt concentration. Finally, q^*_M and q^*_D values corresponding to an arbitrary salt concentration can be predicted using the interpolating functions. Figure 5.1 illustrate these steps graphically.
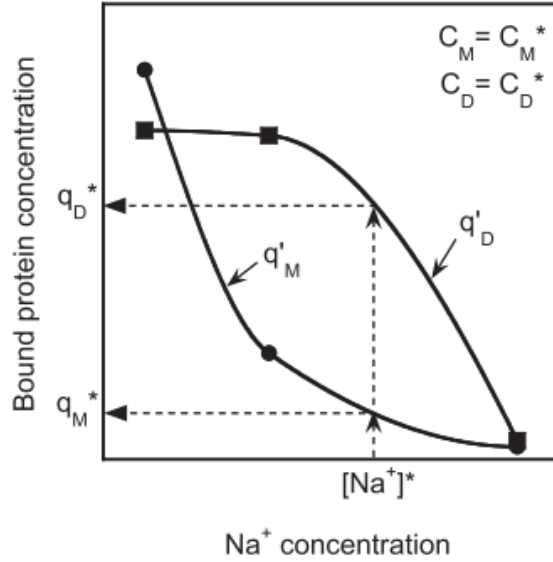
Figure 5.1. Illustration of the PCHIP interpolation method to calculate unknown q_M^* and q_D^*. The experimental data q_M and q_D at values of C_M and C_D are circles and squares, respectively. The two solid lines are the PCHIP curves (Creasy *et al.*, 2018).

In this work, the effect of sodium concentration is interpolated using MATLAB *pchip* function that uses piecewise continuous Hermite interpolation polynomials. If the queried isotherm point is outside of the range of lookup table, a linear extrapolation method is used to estimate the q value.

At low protein loading, the isotherm is expected to become linear and multicomponent binding becomes non-competitive. This is expected to occur at high salt concentrations. In this case, we have

$$q_i = f\left(C_{Na^+}\right)C_i \tag{5.2}$$

where $f\left(C_{Na^+}\right)$ is a function of the Na$^+$ concentration. If protein binding is dominated by electrostatic interactions, the function $f\left(C_{Na^+}\right)$ can be expressed by the following relationship based on the stoichiometric displacement model (Kopaciewicz *et al.*, 1983):

91

$$f\left(C_{Na^+}\right) = A C_{Na^+}^{-z} \tag{5.3}$$

where z is the effective charge. In this limit, the model parameters can be determined empirically from gradient elution experiments according to the method of Yamamoto (1995). The method is based on the relationship between the sodium concentration at elution, $C_{Na^+}^E$ and the normalized gradient slope, γ, defined as follows:

$$\gamma = \frac{\varepsilon\left(C_{Na^+}^{final} - C_{Na^+}^{initial}\right)}{CV_G} \tag{5.4}$$

where $C_{Na^+}^{initial}$ and $C_{Na^+}^{final}$ are the initial and final Na$^+$ concentrations in the gradient and CV_G is the duration of the gradient in CV units. The following integral relationship is obtained between $C_{Na^+}^E$ and γ (Yamamoto, 1995):

$$\gamma = \int_{C_{Na^+}^{initial}}^{C_{Na^+}^E} \frac{dC_{Na^+}}{A\left(C_{Na^+}\right)^{-z} + k'_\infty - k'_{Na^+}} \tag{5.5}$$

where k'_∞ is the protein retention factor for conditions of no binding (e.g. at high salt) and k'_{Na^+} is the salt retention factor.

Similar to protein adsorption, sodium phosphate adsorption isotherm is also described with Langmuir model, but in the form of single component adsorption isotherm written as:

$$q_i = \frac{q_{m,i} K_i C_i}{1 + K_i C_i} \tag{5.6}$$

5.3.2 Binding kinetics

As show previously, protein adsorption is nearly completely dominated by pore diffusion on CHT Type I and both pore diffusion and binding kinetics are important for CHT Type II.

Therefore, in both cases, we assume that intraparticle transport is controlled by a pore diffusion mechanism. Accordingly, the continuity equations and boundary conditions are written as follow:

$$\varepsilon'_p \frac{\partial c_i}{\partial t} + \frac{\partial q_i}{\partial t} = \frac{D_{e,i}}{r^2} \frac{\partial}{\partial r}\left(r^2 \frac{\partial c_i}{\partial r}\right) \tag{5.7}$$

$$r = 0, \frac{\partial c_i}{\partial t} = 0 \tag{5.8}$$

$$r = r_p, c_i = C_i \tag{5.9}$$

where i represents either monomer or dimer, r is the particle radial coordinate, and $D_{e,i}$ is the effective pore diffusivity of species i. To simplify the calculation, the so-called linear driving force (LDF) approximation is used instead of the detailed spreading kinetics model discussed in Chapter 4. Accordingly, we have:

$$\frac{\partial q_i}{\partial t} = k_i \left(c_i - c_i^*\right) \tag{5.10}$$

where c_i^* is the concentration of species i in equilibrium with q_i, k_i is the related to spreading kinetics. As discussed previously, adsorption on CHT Type I is dominated by the mass transfer resistance. Conversely, adsorption on CHT Type II is controlled by a combination of mass transfer and the spreading kinetics. Therefore, k_i for CHT Type I is set to a large value to simulate conditions where the kinetics resistance is negligible. For adsorption on CHT Type II, k_i represents the spreading kinetics. Although a theoretical relationship between the spreading kinetics and salt concentration is unknown, an empirical correlation was used in this work where k_i is defined as a function of sodium concentration as follows:

$$k_i = k_{des,i} \left(C_{Na^+} \right)^{\beta}$$ (5.11)

where $k_{des,i}$ is a desorption rate constant in mM$^{-\beta}$ s^{-1}, β is another constant describing the ion-exchange characteristics. This correlation comes from a mobile phase modulator modified Langmuir model developed by Melander *et al.* (1989). The assumption behind this equation is that the adsorption kinetic resistance is suppressed by a increasing sodium concentration, which has been seen in Chapter 4.

5.3.3 Column dynamics

The material balance for component i in the column is described by the following equation:

$$u \frac{\partial C_i}{\partial x} + \varepsilon \frac{\partial C_i}{\partial t} + (1 - \varepsilon) \frac{\partial \langle \hat{q}_i \rangle}{\partial t} = 0$$ (5.12)

where C_i is the protein concentrations in the mobile phase, respectively, $\langle \hat{q}_i \rangle$ is the average protein concentration in the adsorbent particles and, u is the superficial velocity. This equation is based on an assumption that axial dispersion is negligible. Boundary conditions are as follows:

$$x = 0, \quad C_i = C_{i,F}$$ (5.13)

$$x = L, \quad \frac{\partial C_i}{\partial x} = 0$$ (5.14)

where and $C_{i,F}$ is protein concentrations at the column entrance. In this work, we ignore the boundary layer mass transfer resistance because the Biot number is estimated to be well above 10, using values of the boundary layer mass transfer coefficient estimated from the Sherwood number.

Based on a material balance for the particle, $\partial \langle \hat{q}_i \rangle / \partial t$ can be written as follows:

$$\frac{\partial \langle \hat{q}_i \rangle}{\partial t} = \frac{3D_{e,i}}{r_p} \frac{\partial c_i}{\partial r}\bigg|_{r=r_p} \tag{5.15}$$

Combining Eq. (5.12) and (5.15), we obtain the following result:

$$u\frac{\partial C_i}{\partial x} + \varepsilon\frac{\partial C_i}{\partial t} + (1-\varepsilon)\frac{3D_{e,i}}{r_p}\frac{\partial c_i}{\partial r}\bigg|_{r=r_p} = 0 \tag{5.16}$$

In this work, for the numerical solution of these equations, the radial derivative $\partial c_i/\partial r$ in Eq.

(5.7) was approximated by finite differences while the spatial derivative $\partial C_i/\partial x$ in Eq. (5.16)

was approximated by the Euler backwards finite differences method. Numerical dispersion

caused by the latter approximation was minimized by using 100 discretization points.

The protein elution behavior can be predicted through combination of the discretized forms of

Eqs. (5.7), (5.10) and (5.16) and adsorption isotherm data obtained from the EI method. The

resulting set of ordinary differential equations are solve numerically using *ode15s* in MATLAB

R2017b (The Mahworks, Naick, MA, USA).

5.4 Results and discussion

5.4.1 Experimental linear gradient elution results

The first objective was to compare NaCl and Na_2HPO_4 gradient. Figure 5.2 shows the

experimental results for CHT Type II with either NaCl or Na_2HPO_4 gradients. As seen in this

figure, some separation of monomer and dimer is seen with the NaCl gradient. However, much

better results are obtained with the phosphate gradient. It is likely that this difference is related to

the significant pH drop generated when the sodium concentration is increased. The pH drop

increases the net charge of both the monomer and the dimer and apparently results in lower

selectivity. Although a slight pH drop is also observed with the phosphate gradient, the intensity

and duration are much smaller and shorter than those obtained with the chloride gradient.
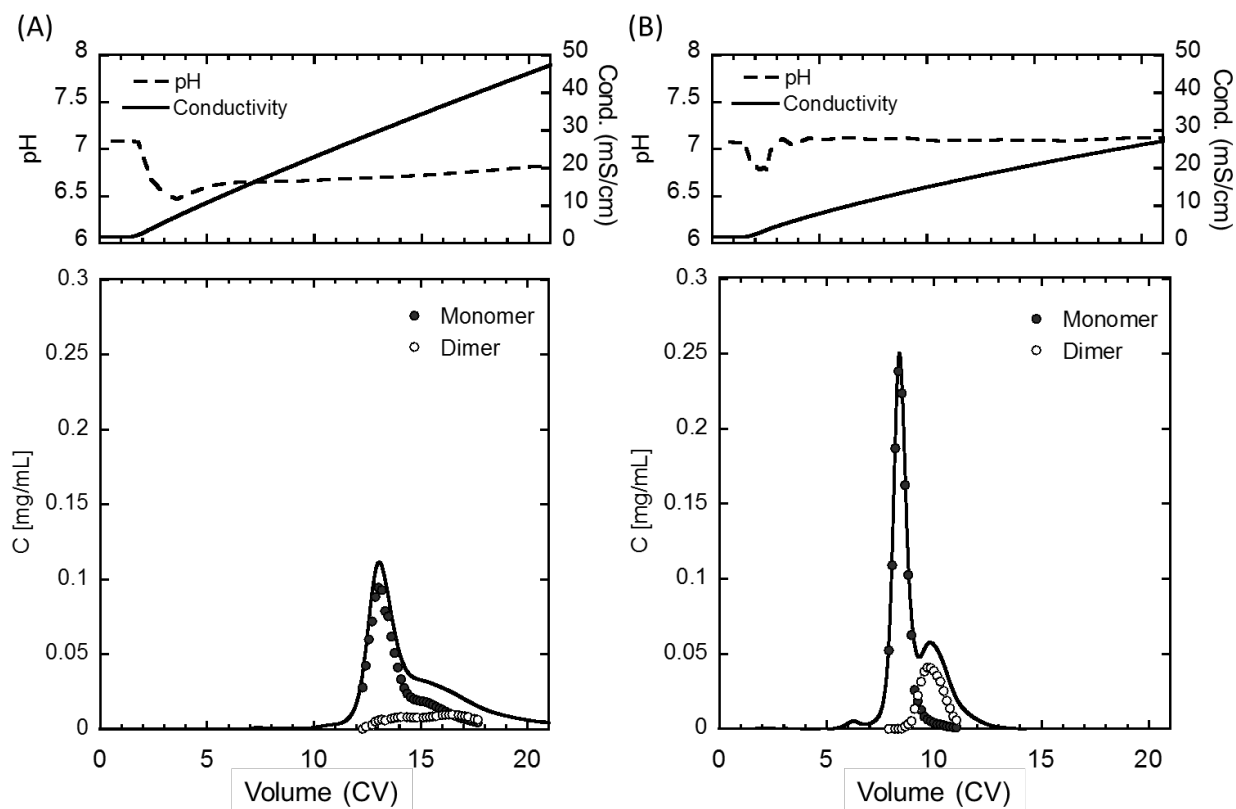
Figure 5.2. Linear gradient elution of mAb monomer-dimer mixture on CHT Type II. (A) 0 to 1000 mM NaCl gradient in 10 mM Na_2HPO_4 at pH 7.0 in 20 CV. (B) 10 to 500 mM Na_2HPO_4 gradient at pH 7.0 in 20 CV.

5.4.2 Sodium phosphate adsorption

It has been reported that CHT as well as cation exchange resins can adsorb cations during step or gradient elution (Bankston *et al.*, 2010; Ghose *et al.*, 2002; Pabst and Carta, 2007). In this work, a significant difference was observed between experiments and model predictions if sodium phosphate was assumed to be unbound. This discrepancy demonstrates that adsorption of sodium phosphate is not negligible. Thus, the correct prediction of sodium phosphate gradients in CHT column requires precise information about the sodium phosphate isotherm. The adsorption of sodium phosphate was, thus, characterized by pulse injection of a 100 μL 500 mM Na_2HPO_4 solution into a CHT column pre-equilibrated using buffers containing different Na_2HPO_4 concentrations. High salt peaks generally come out of the column later if the column was

equilibrated with a lower Na₂HPO₄ concentration buffer. This is due to slower interaction

between the P-sites of the stationary phase and sodium at lower Na₂HPO₄ concentration. The salt

retention behavior can be used to determine the adsorption isotherms. By definition, the

expression of salt retention factor k'_{Na^+} is as follow:

$$k'_{Na^+} = \frac{1-\varepsilon}{\varepsilon} K \qquad (5.17)$$

where ε is the extraparticle porosity in the column and K is the sodium phosphate partition

coefficient ($d\bar{q}/dc$) describing partitioning between the particle and the solution. The

experimentally obtained retention factors are listed in Table 5.1. The sodium phosphate binding

capacities and equilibrium constants can be calculated by combining Eq. (5.6) and (5.17) and

The regressed parameter values are $q_{m,Na_2HPO_4} = 180$ mmol/L and $q_{m,Na_2HPO_4} = 70$ mmol/L for

CHT Type I and Type II, respectively, and $K_{Na_2HPO_4} = 0.003$ L/mmol and $K_{Na_2HPO_4} = 0.010$

L/mmol for CHT Type I and Type II, respectively.

Table 5.1. Experimental obtained retention factor of Na₂HPO₄ pulse injection

Salt concentration in running buffer	Sodium phosphate retention factor, k'_{Na^+}	
[Na⁺] (mM)	CHT Type I	CHT Type II
40	2.80	2.25
60	2.45	1.84
80	2.42	1.79
100	2.17	1.71
200	1.84	1.57
300	1.77	1.56

5.4.3 Protein retention at low protein loads

Linear gradient elution (LGE) experiments were used to determine the effective binding charge and adsorption affinity constant of the mAb monomer and the mAb dimer in the linear isotherm region according to the method of Yamamoto (1995). The values of the effective binding charge and adsorption affinity constant for each mAb species are used in the EI method at low protein loads and high salt concentrations. Figure 5.3 shows the LGE chromatograms of the mAb monomer and dimer on CHT Type I and Type II columns with different gradients durations. As seen in these figures, the monomer peaks are narrower than dimer peaks, demonstrating less mass transfer resistance due to the smaller size of the monomer. As also seen in these figures, the monomer elutes at lower salt concentrations compared to these of the dimer, owing to the higher charge of the dimer molecules and stronger binding of the dimer.

The values of effective charge, z, and adsorption affinity constant, A, are obtained from the slope and the intercept of Eq.(5.5). The protein non-binding retention factor, k'_∞, that appears in this equation was obtained from pulse injections of monomer and dimer at 500 mM Na_2HPO_4. The salt retention factor, k'_{Na^+}, was estimated from pulse injections of Na_2HPO_4. Figure 5.4 shows a log-log plot of the normalized gradient slope, γ, vs. the Na^+ concentration at elution for the monomer and dimer on CHT Type I and Type II column. As expected, the salt concentration at elution is lower for smaller values of γ and, thus, for longer gradients. The regressed values of A and z are listed in Table 5.2. The values of the effective characteristic charge and of the equilibrium constant of the dimer are both higher than those of the monomer as expected.
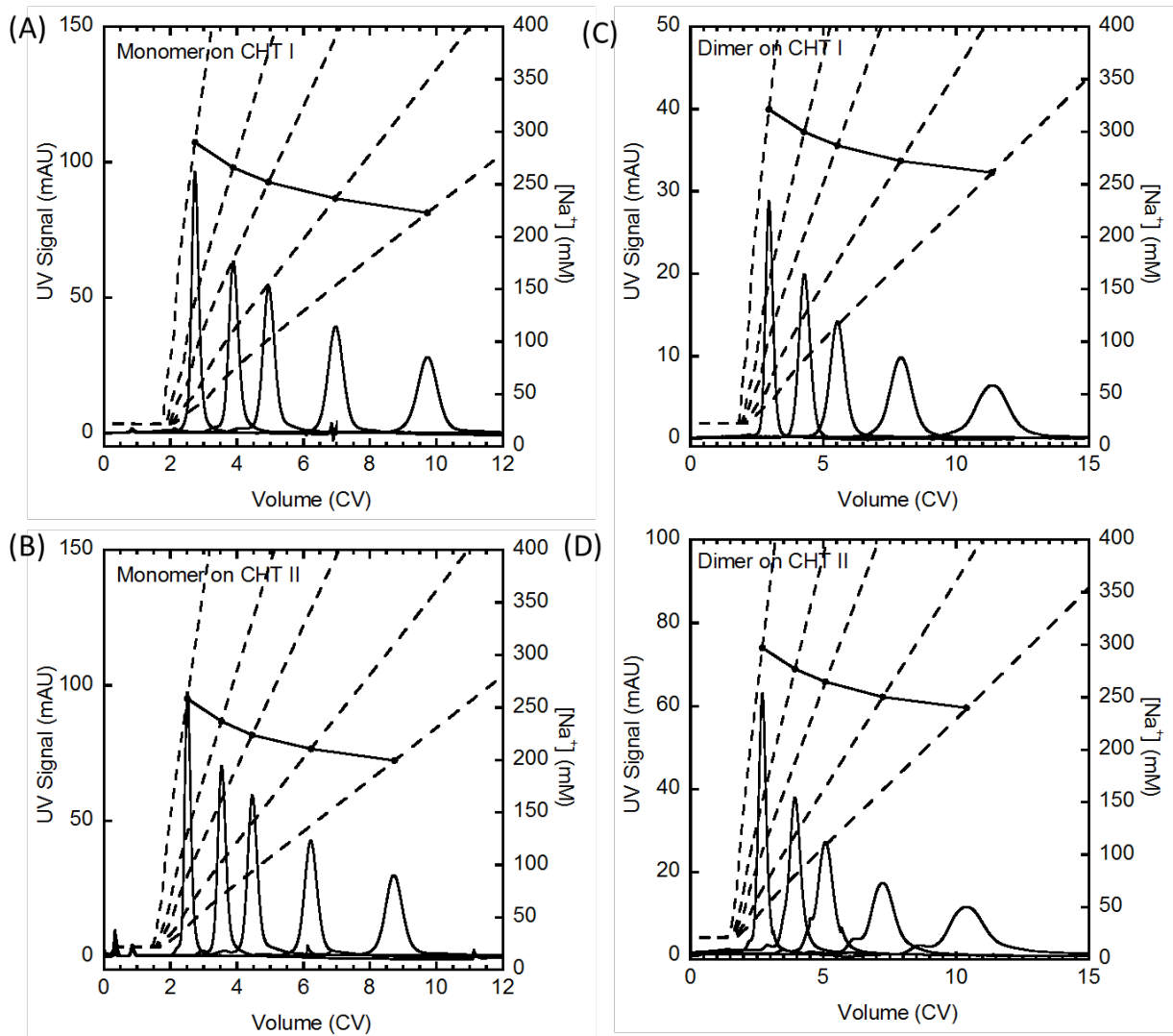
Figure 5.3. Overlaid linear gradient elution chromatograms of mAb monomer and dimer on CHT Type I and Type II. Solid and dashed lines represent the UV signals and the sodium concentration converted from conductivity. The thick solid lines connect the conductivity values at which the peak elutes at each gradient slope.
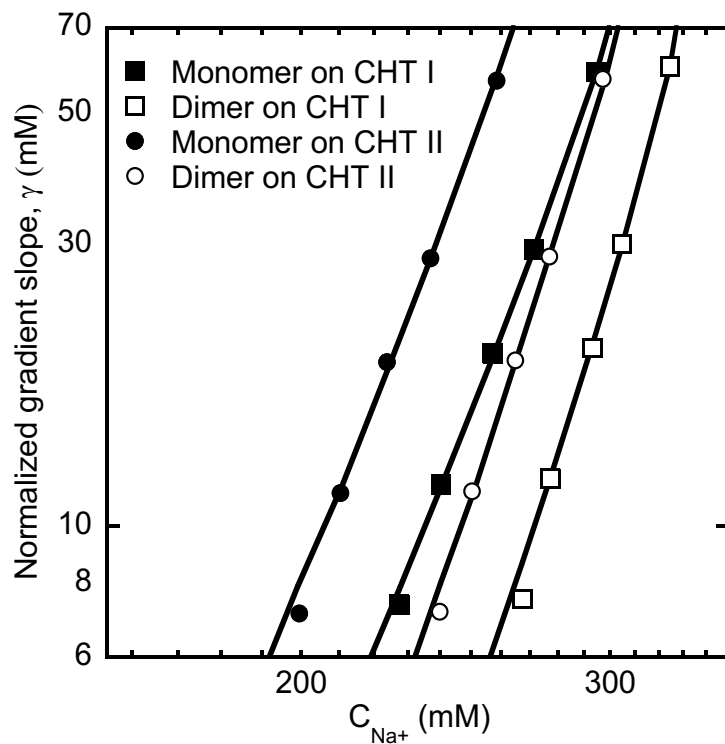
Figure 5.4. Normalized gradient slope with the Na⁺ concentration at elution for LGE experiments.

Table 5.2. Summary of the protein effective charge, z, and equilibrium constant, A, from LGE experiments

Molecule	CHT Type	z	A (mM^z)
Monomer	Type I	5.88	3.18×10^{14}
	Type II	6.05	3.01×10^{14}
Dimer	Type I	7.32	2.32×10^{18}
	Type II	7.26	6.73×10^{17}

5.4.4 Model calibration

Batch isotherm data obtained at sodium phosphate concentrations of 10, 35 and 70 mM were utilized in the EI method. For both monomer and dimer, the adsorption isotherm becomes linear at high Na^+ concentration. This occurs at Na^+ concentrations above 175 and 185 mM for the monomer on CHT Type I and II, respectively, and above 185 and 200 mM for the dimer on CHT Type I and II, respectively. At these Na^+ concentrations and higher, Eq. (5.2) with the parameters in Table 5.2 are used instead of the batch isotherm data.

Figure 5.5 shows a comparison between the experimental results and model prediction obtained at different protein loadings with a phosphate gradient. As discussed previously, protein adsorption on CHT Type I is nearly completely dominated by pore diffusion. Conversely, adsorption on CHT Type II depends on a combination of pore diffusion and binding kinetics. Therefore, no extra kinetic resistance was added to the adsorption of CHT Type I. However, a kinetic resistance expressed according to Eq. (5.11) was introduced into the model for CHT Type II using k_{des} values for 0.2 and 0.02 for monomer and dimer, respectively, and β equal to 0.145 for both of monomer and dimer. The effective pore diffusivities, D_e, determined from confocal laser scanning microscopy (shown in Table 4.2 of Chapter 4) were used for both Type I and II adsorption without adjustments. The effective pore diffusivity of salt is expected to be at least one order of magnitude higher than the protein values, so that mass transfer resistance of salt is negligible in the model calculation.

As seen in Figure 5.5A-C, for CHT Type I, the EI method accurately describes the elution peak shape without any added kinetic resistance. This is consistent with the conclusion in Chapter 4 that the protein behavior on CHT Type I is mainly controlled by mass transfer resistance. The main discrepancy seen is associated with the 30 mg/mL load condition. For this run, the model

predicts higher retention for both monomer and dimer compared to the experimental profiles, suggesting this discrepancy may have been caused by a systemic reason. Figure 5.5D-F compares the model predictions using the pore diffusion model (shown as dashed lines) with the model predictions combining pore diffusion and adsorption kinetics (shown as solid lines). All the peaks with dashed lines for both monomer and dimer at low load and high load are much shaper compared to the experimental results, demonstrating that more kinetic resistance exists in addition to mass transfer resistance. These results are also consistent with the conclusion of Chapter 4 that spreading kinetic resistances is only associated with the CHT Type II and this resistance can be suppressed in weak binding conditions introduced by high sodium concentrations.
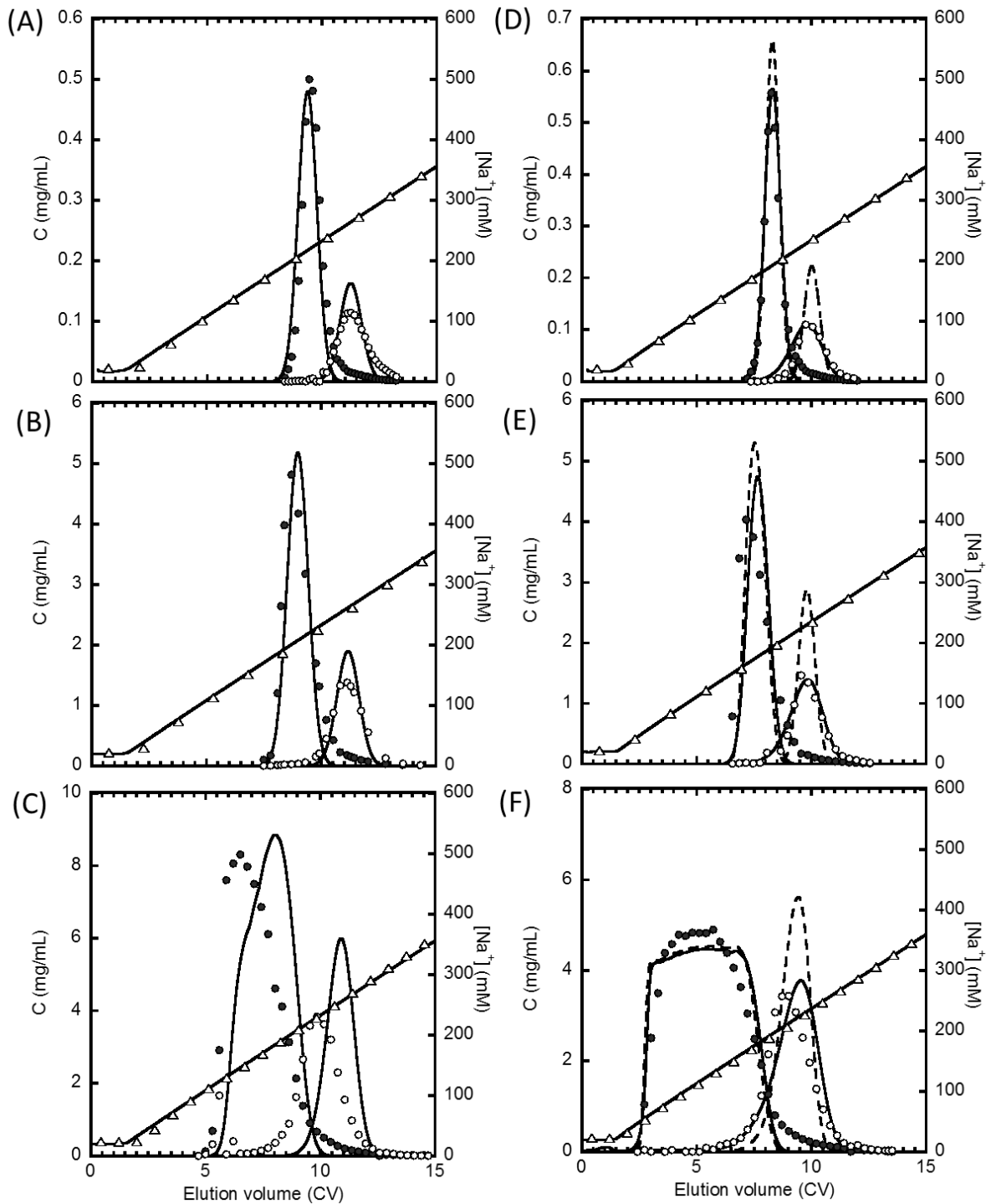
Figure 5.5. Comparison of experimental data (dots) and model prediction (lines) based on the EI method with 20 to 510 mM Na$^+$ gradients at pH 7.0 in 20 CV on CHT Type I (A-C) and CHT Type II (D-F). Protein loads are (A, D) 0.8 mg/mL, (B, E) 10 mg/mL and (C, F) 30 mg/mL. Monomer and dimer are solid and hollow circles, respectively. Na$^+$ concentration is shown as triangles. Dash lines shown model predictions based on pore diffusion alone without a kinetic resistance in (D-F).

5.5 Comparison of frontal analysis and gradient chromatography

5.5.1 Chromatographic optimization

Our previous work developed and validated a mechanistic model that is capable of describing mAb monomer dimer separation by either frontal analysis or gradient chromatography. The goal of this section is to compare these two modes of operation. For simplicity, we focus only one stationary phase, CHT Type II. In order to compare the two processes, objective functions need to be defined based on certain constraints. The operating parameters are divided into two categories: design parameters and decision variables following Gallant *et al.* (1996), Felinger and Guiochon (1998), and Katti and Jagland (1998). Design parameters are variables that are not allowed to be changed during the process, while the decision variables are selected to maximize the objective function.

In designing preparative chromatography processes, productivity, *P* and recovery yield, *Y* are the most commonly used values to characterize the column performance. These quantities are calculated from the following equations:

$$P_i = \frac{C_{i,Load}V_{Load}Y_i}{(1-\varepsilon)V_c t_{cycle}} \tag{5.18}$$

$$Y_i = \frac{\int_{t_1}^{t_2} C_i dt}{C_{i,F}t_F} \tag{5.19}$$

where $C_{i,Load}$ and V_{Load} are the protein load concentration of component i and load volume, respectively, ε is the extraparticle void fraction, V_c is the column volume and t_{cycle} is the total cycle time. In general, one cycle includes equilibration, load, elution, and regeneration. In Eq.

(5.19), t_1 and t_2 are the cut times which allow the achievement of the required constraint. In this work, we define the objective function as the product of productivity and yield, PrY. Previous work by Felinger and Guiochon (1998) found that optimizing using this product as the objective function compared to productivity alone significantly increase yield and only slightly decrease the productivity. A comparison of the two operation processes, frontal analysis and gradient elution, is listed in Table 5.3 including the process duration for each step and the corresponding flow velocity. To maximize the production rate, the column needs be operated at the highest possible flow rate unless flow rate could make an impact in the separation performance in this step. Thus, equilibrium and regeneration are operated at the maximum flow rate which is determined by the maximum pressure drop based on the Darcy equation:

$$\Delta P_{max} = \frac{u_{max} \eta L}{B_0} \tag{5.20}$$

where u is the superficial mobile phase velocity, η is the liquid viscosity, L is the column length and B_0 is the hydraulic permeability.

The focus of this work will be the process comparison after 40 μm CHT Type II has been selected as a stationary phase and the sodium phosphate buffer at pH 7.0 has been selected as a mobile phase. Thus, stationary phase, particle size, buffer species and pH are all fixed design parameters during the process comparison. In practice, a chromatographer has to design a process based on available column length (L) and column diameter (D) as well as feed constituents ($C_{F,M}$ and $C_{F,D}$). To simplify the comparison, we assume the same column and the same load material are used for both modes of operation.

The load volume, $V_{Load,LGE}$, for gradient elution is another important factor that impacts the overall productivity. However, in previous experiments, up to 85% of column binding capacity was utilized under the highest load condition (seen in Figure 5.5F) and no breakthrough observed. For this case, we have chosen to load the column for a gradient elution to 50% of the column binding capacity. Accordingly, $V_{Load,LGE} = 0.5 \times EBC_M / C_M$, where EBC_M is the column equilibrium binding capacity of monomer. The monomer product will be collected at different steps for two chromatographic modalities. For frontal analysis, pure monomer breaks through during the loading step. The load volume, $V_{Load,FA}$, can thus be calculated based on the purity level. For gradient elution, the pure monomer elutes during the elution step. The elution volume, $V_{Elute,FA}$ is also calculated based on a fixed purity level. All the design parameters are listed in Table 5.4.

Table 5.3. Comparison of frontal analysis and gradient elution processes

Operation procedure	Frontal analysis		Gradient elution	
	Duration	Flow velocity	Duration	Flow velocity
Equilibrium	3 CV	u_{max}	3 CV	u_{max}
Load	$V_{Load,FA}$	u	$V_{Load,LGE}$	u
Elute	2 CV	u_{max}	$V_{Elute,FA}$	u
Regeneration	2 CV	u_{max}	2 CV	u_{max}

The optimization process can only be carried out in an operating window within certain constraints. In general, there are two types of constraints: physical constraints and efficiency constraints. The physical constraints refer to the factors that can adversely affect the separation, such as the maximum pooled protein concentration. In this work, we assume the proteins are

stable in the operation range and the only concern is the efficiency constraint. In this case, the efficiency constraint is a monomer purity of 95%.

There are many decision variables that directly impact the objective function. For both modes of operation, residence time (L/u) directly impacts the column resolution through controlling the band shape and spreading. For gradient chromatography, the elution gradient slope $(= \left(C_{Na^+}^{final} - C_{Na^+}^{initial} \right) / CV_G$) is another important variable. Unlike the gradient elution, frontal analysis is sensitive to the loading salt concentration since that salt directly influences selectivity and kinetic resistance. Each of these three decision variables will be discussed below. The comparison will begin with individual process optimization followed by a comprehensive comparison of these two.

5.5.1.1 Frontal analysis optimization

As discussed in Chapter 4, frontal analysis separation performance varies depending on the load Na^+ concentration. The relationship between process productivity (P), pooled monomer yield (Y), and PrY values are shown as a contour plot in Figure 5.6. The contour plots of productivity, yield and the product of productivity and yield were generated by JMP statistical analysis software (SAS Institute, Cary, NC) using 20-50 data points. Na^+ concentration affects these relationships through its impact on binding capacity and band broadening. Lower Na^+ results in greater loadability compared to higher Na^+. It also causes lower monomer recovery for a given pooled monomer purity or lower pooled monomer purity for a given monomer recovery. As shown in Figure 5.6A, optimum productivity appears at 70 mM Na^+. This relationship is also shown in Figure 5.6B where intermediate salt provides a better yield at any residence time. By comparing the objective function from all three buffer conditions shown in Figure 5.6C, 70 mM

Na$^+$ and 5.3 min residence time can be selected as the optimum process condition with the

highest *PrY* value.
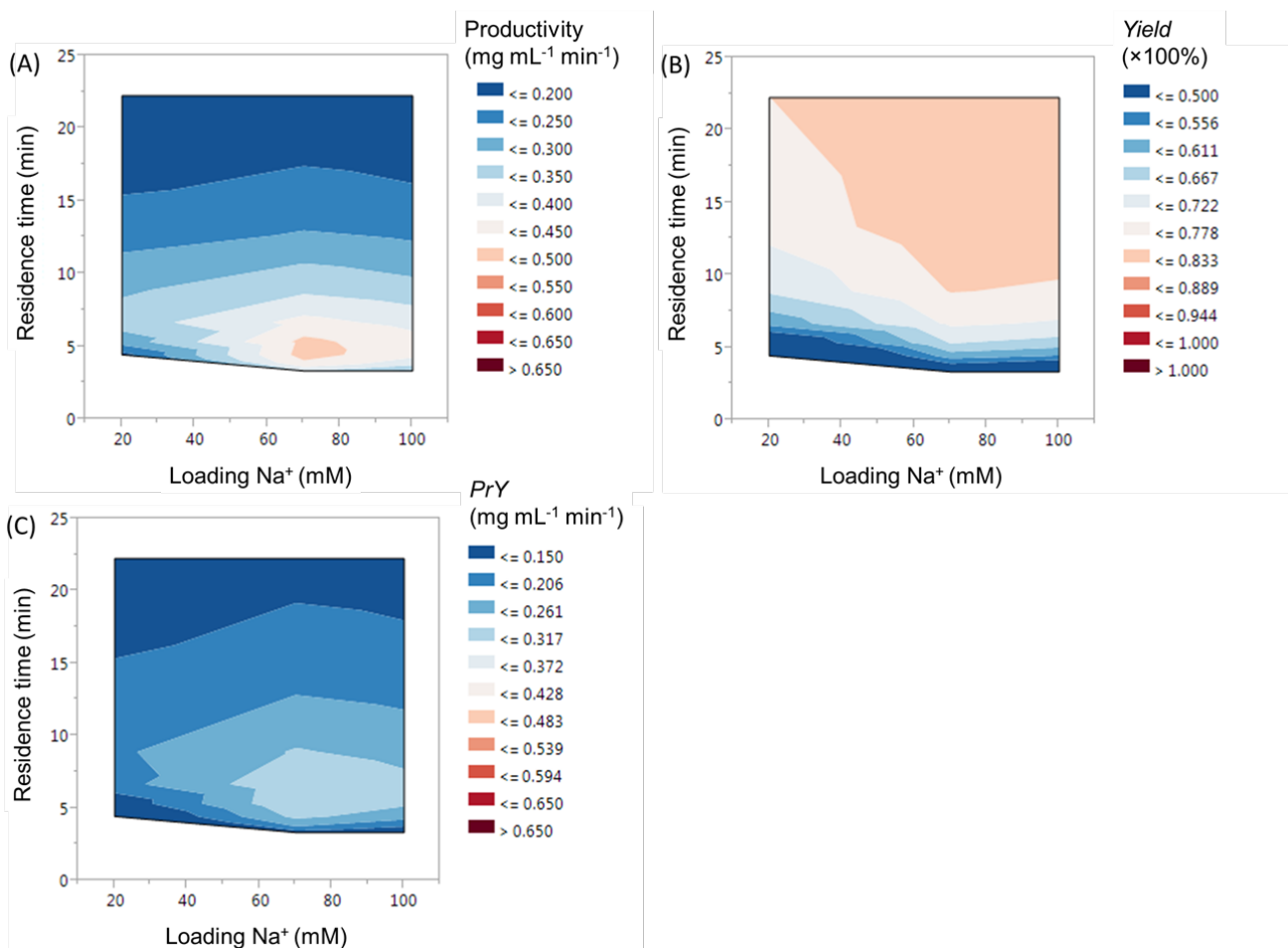
Figure 5.6. Contour plots of (A) productivity, (B) yield and (C) product of productivity and yield in different residence times and gradient durations for frontal analysis mode separations.

5.5.1.2 Gradient chromatography optimization

To minimize the differences between two modes of operation and simplify the comparison, 70

mM Na$^+$ is also chosen as the loading buffer for gradient elution. A sodium phosphate buffer

containing 510 mM Na$^+$ that can fully elute all the bound materials is chosen as the final buffer

for the gradient. In this case, the gradient duration is the only impact factor for column

performance. Figure 5.7 shows the contour plot of objective functions with different gradient

durations and residence times. Previous work has demonstrated that productivity has a quadratic relationship with different normalized gradients (Carta and Jungbauer, 2010). This result is also seen in Figure 5.7A. At practical residence times (< 10 min), there is a clear optimum gradient that maximizes productivity. At higher residence times (> 10 min), higher productivity is obtained with a shorter gradient. Figure 5.7B shows that the yield is stable at most of the operation conditions. Only the conditions at the left bottom corner deliver severe yield losses, where the process is operated at shorter gradients with short residence times. Therefore, the best operation condition can be determined as the values that maximize the product of productivity and yield seen in Figure 5.7C. The optimized residence time is 3.8 min with a 10 CV gradient from 70 Na^+ to 510 Na^+.
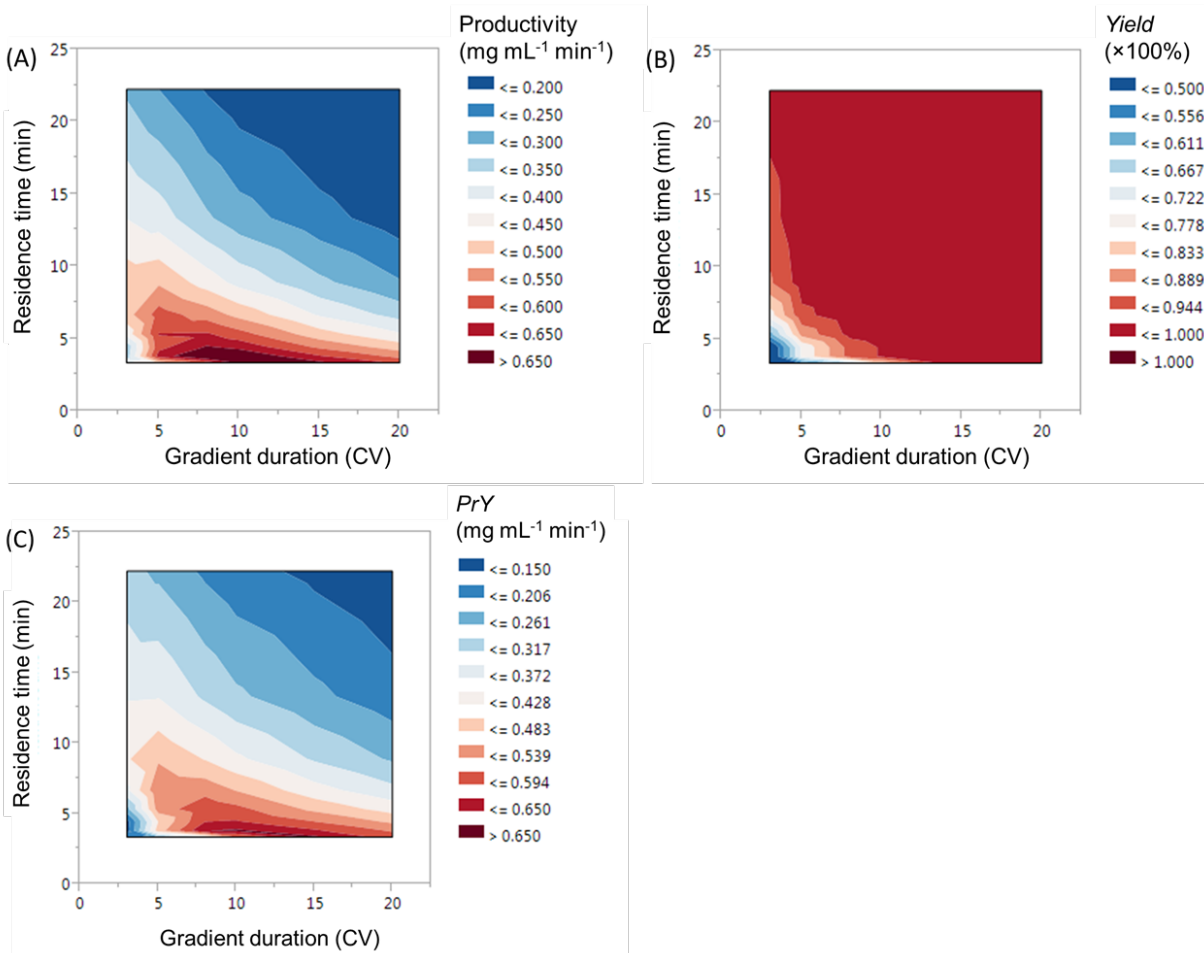
Figure 5.7. Contour plots of (A) productivity, (B) yield and (C) product of productivity and yield in different residence times and gradient durations for gradient elution mode separations.

5.5.2 Performance comparison

A comparison of frontal analysis and gradient elution can be conducted by comparing Figure 5.6 and Figure 5.7. The optimized gradient elution provides a process with a 0.70 mg/(mL min) productivity and 95% monomer yield. The optimized frontal analysis only provides 0.46 mg/(mL min) productivity with a 67% yield. As high as 80% yield can be achieved by frontal analysis method using 10 min residence time in the exploring conditions. The low performance of frontal analysis is partially due to that bound monomer is not fully displaced by the dimer. Another reason is that the severe spreading kinetic resistances reduce the selectivity from ideal cases.

Therefore, yield and productivity is also lower than the gradient elution mode. Even though the kinetic resistance also occurs during gradient chromatograpy, proteins are separated during the elution step, where high salt concentrations suppress the spreading resistance (shown in Chapter 4). Accordingly, gradient elution provides better resolution and thus higher yield leading to greater productivity compared to frontal analysis for this case of monomer-dimer separation.

Table 5.4. Operation conditions chosen to compare frontal analysis and gradient elution processes.

Variable	Type	Comments
Column diameter (D)	Design parameter	1.0 cm
Column length (L)	Design parameter	8.5 cm
Feed monomer concentration ($C_{F,M}$)	Design parameter	2.9 mg/mL
Feed dimer concentration ($C_{F,M}$)	Design parameter	1.3 mg/mL
pH	Design parameter	7.0
Eluting salt	Design parameter	510 mM Na$^+$
Load volume for LGE (V_{Load})	Design parameter	29 mL
Maximum flow rate (u_{max})	Design parameter	6.4 cm/min
Monomer purity	Constraint	95%
Loading salt	Decision parameter	70 mM Na$^+$
Elution gradient for LGE	Decision parameter	10 CV
Flow velocity (u)	Decision parameter	2.2 cm/min for LGE 1.6 cm/min for FA

Chapter 6 Concluding Remarks and Recommendations

This dissertation provides a comprehensive study of Type I and Type II ceramic hydroxyapatite (CHT) chromatographic adsorbents and the utilizations of CHT in mAb monomer-dimer separation. This includes a physical characterization of adsorbent particles, a study of mAb monomer/dimer competitive behavior on the particle level, examinations of chromatographic separation using frontal analysis and bind-elute chromatography as well as a mechanistic study of protein adsorption on the surface of CHT via model characterization. The final conclusions and recommendations for future work are discussed below.

6.1 Competitive binding of mAb monomer and dimer

The adsorption of a mAb monomer and dimer is consistent with electrostatic interaction, akin to that observed for binding to cation exchange resins. Adsorption capacities for mAb monomer and dimer are higher for Type I compared to Type II in approximate proportion to the higher surface area of the former, suggesting that the nanocrystal surfaces is accessible by both molecules. Relatively high selectivities are obtained for the dimer relative to the monomer at low Na^+ concentrations. The exact reasons for this behavior are not known. However, since the monomer and dimer have the same pI, it is likely that preferential binding of the dimer for these conditions occurs because of its larger size and binding charge per molecule compared to those of the monomer. The adsorption kinetics is controlled by pore diffusion for both CHT types and for both single component and mixture adsorption, and is much faster for Type II because of its larger pore size. A remarkable result is the readily occurring displacement of bound monomer by the dimer. The rate at which this occurs and the relatively high dimer/monomer selectivity suggests that CHT (Type II, in particular) can also be used to perform monomer-dimer separations by frontal analysis as has already been shown for cation exchangers.

From a more practical viewpoint, one recommendation can be concluded that the choice of Type I vs. Type II for the monomer-dimer system will depend on whether high capacity or high speed is desired. Type I has higher binding capacity and more protein can be loaded per cycle. However, it also has slower kinetics, thereby requiring longer residence times and, thus, longer cycles. On the other hand, while less protein can be loaded per cycle on Type II, the faster kinetics allows shorter residence times and, thus, shorter cycles. The choice between CHT and cation exchange is not as straightforward, however. For example, comparing CHT Type II and the cation exchanger Nuvia HR-S, CHT appears to have higher selectivity, faster mass transfer, and faster displacement kinetics at low salt conditions. However, selectivity and rates depend on salt concentration for Nuvia HR-S, so that a definitive conclusion is not possible at this point. Moreover, additional factors such as stability, cleanability, packability, reusability, column backpressure, and cost will come into play when making such a comparison.

A recommendation for future work would include extending this work to other applications where protein interacts to C-sites or applications involving multimodal interactions with P- and C-sites. For example, acidic proteins, such as thyroglobulin (Tg) and bovine serum albumin (BSA), can be used as model proteins to explore the selectivity of C-sites. It would be of interest to study this model protein mixture system. First of all, the molecular weight of BSA is 10 times smaller than that of Tg. Since high selectivity has been seen with basic proteins of different sizes, such as, the strongly bound mAb dimer that partially displaces the weakly bound mAb monomer, it would be insightful to check whether this is the case also for the adsorption on C-sites. Secondly, we have already observed that large molecules such as virus-like particles (VLPs) cannot diffuse through CHT pores and only bind at the outer surface of the CHT particles, these bound VLPs do not influence the transport of RNA. A remaining question is whether this

behavior will occur to other mixtures of small and large proteins. BSA-Tg kinetic and equilibrium adsorption can be performed to reveal the steric effects on diffusion. The comparison between acidic protein behavior and the mAb competitive binding will further elucidate the underlying cause of the CHT displacement phenomena.

6.2 Frontal chromatography of mAb monomer and dimer

The separation of antibody monomer-dimer mixtures by frontal analysis was obtained using either CHT Type I or Type II columns at residence times between 2.5 and 5.6 min indicating that the adsorption dynamics are sufficiently fast in both cases for practical conditions. The two component breakthrough curves consist of a pure monomer front followed by a monomer-dimer displacement front. Relatively pure monomer, which is the weaker bound species, is recovered between the two fronts. The binding capacities obtained from the frontal analysis data agree with Langmuir model predictions over a range of Na^+ concentrations in the load buffer. However, kinetic effects are pronounced resulting in separations that are not as good as predicted under ideal conditions. For CHT Type I, which has smaller pores, adsorption is nearly completely dominated by pore diffusion. Conversely, for CHT Type II, which has larger pores, columns dynamics results from a combination of pore diffusion and binding kinetics, the latter becomes more pronounced as the salt concentration is reduced and protein binding becomes stronger. Although sharper breakthrough fronts are obtained at higher salt concentrations because of the reduce impact of adsorption kinetics, the binding capacity decreases leading to a smaller distance between the pure monomer front and the monomer-dimer displacement front requiring a trade-off of capacity and rates.

Three different column dynamic models based on different mechanistic assumptions were tested for their ability to describe the experimental results and predict separations – a pore diffusion

model, a pore diffusion model with Langmuir adsorption kinetics, and a pore diffusion model with spreading kinetics where adsorbed molecules are hypothesized to exist in two different interconvertible bound states, one freely exchangeable for molecules in solution and the other not at all directly exchangeable with molecules in solution. The spreading model provided the best description of the CHT Type II frontal analysis data and could be used to predict the effects of feed concentration, percentage of dimer in the feed, and residence time. This model could also predict the intraparticle concentration profiles observed by confocal microscopy during co-adsorption of monomer-dimer mixtures on individual CHT particles. Finally, the spreading kinetic model was corroborated by comparing experimental results and model predictions for isocratic elution for conditions where the isotherm is linear using rate parameters determined from the moments of the experimental peaks. These results show that the spreading kinetics model, including pore diffusion, can also describe the low-loading isocratic elution behavior with parameters that follow trends similar to those observed for the frontal analysis case, suggesting that the postulated existence of multiple binding sites is likely responsible not only for the displacement kinetics but also the elution behavior of each individual monomer and dimer species.

6.3 Gradient elution chromatography of mAb monomer and dimer

The separation of antibody monomer-dimer mixtures by gradient chromatography using a linear gradient elution was obtained with either CHT Type I or Type II columns. The gradient generated by increasing sodium chloride created a pH drop leading to low column resolution for mAbs. On the other hand, sodium phosphate buffer maintained the pH well during the gradient and provided a good separation of the monomer-dimer mixture.

A chromatographic model based on the EI scheme coupled with a pore diffusion model combined with lumped adsorption kinetics was developed and validated in this work. This model can successfully account for the displacement of two components and accurately predict the protein elution behavior on CHT stationary phases. For CHT Type I, adsorption is nearly completely dominated by the pore diffusion kinetics, which is consistent with the results obtained from frontal analysis. The spreading kinetic resistance associated with CHT Type II, seen from frontal analysis and isocratic elution, were also observed in gradient elution as sharper peaks compared to the experimental results were predicted using the pore diffusion model only. A lumped kinetic function which accounts for the change of spreading kinetics due to the change of sodium phosphate concentrations in the gradient elution successfully describes the spreading kinetics and provides a good agreement with the experimental data.

A procedure for optimization and evaluation of frontal analysis and bind-elute chromatography is presented based on a mAb monomer-dimer case study using the model developed in Chapter 4 and Chapter 5. A trade-off between productivity and yield is seen for both modalities. In the comparison of frontal analysis and gradient elution, the latter shows better productivity and yield compared to the former. One of the key reasons is that the displacement of monomer by dimer occurs very slowly on the column. High yield still could be obtained with frontal analysis. An 84 % yield via frontal analysis was seen in the design; however, it requires a 22 mins residence time. Thus, productivity is very low due to the high residence time. Another reason for the low yield is that the selectivity of frontal analysis is dominated by the spreading kinetics that can only be reduced by higher salt concentrations present in gradient elution.

Conversely, there are other beneficial effects brought by frontal analysis. For example, frontal analysis is very easy to operate, where adsorption and separation both occurs during the load

116

step. From the perspective of cost, frontal analysis is less costly since it does not require various buffers, reliable pumps and mixers to generate a gradient. Another advantage is that the eluate is still in the low salt buffer and is highly concentrated, thus, no additional buffer exchange steps or concentration steps are required for the following steps. If we consider the overall purification process, a frontal analysis polishing step can save time and provide higher productivity. However, if the yield is most crucial parameter, gradient elution is preferable to frontal analysis.

This work demonstrated the benefits of mechanistic modeling to obtain a deeper understanding of chromatographic processes. Furthermore, the model and the optimization procedure developed in this work is sufficiently general that it can be adapted to the purification of most proteins on many chromatographic adsorbents, leading to robust and efficient downstream purification process designs.

Although the method presented in this work provides a reliable way to optimize the process in terms of productivity and yield, this work neglects a few aspects, such as the cost of the instrument and material. A recommendation for further work would be an economic analysis of different modalities. Other issues including the choice of pH, elution salt species, and loading concentration remain to be addressed. Further, isocratic elution and displacement chromatography could also be considered in future comparisons in order to gain a broader vision of the effect of all the chromatographic modalities.

Another recommendation in furthering this work is process optimization using frontal analysis as a load step and gradient elution as an elution step. This combination allows maximum utilization of the column total binding capacity. Meanwhile, a higher resolution and yield can also be obtained by collecting the bound material with a high salt elution. Purified protein can be collected in both loading and elution phases maximizing the selectivity of the column. This

combination can be implemented using a multi-column system and operated using the concept of continuous chromatography (Kaltenbrunner *et al.*, 2016; Müller-Späth *et al.*, 2011; Strube *et al.*, 1998).Wherein, one column would be loaded with frontal analysis, while the other pre-saturated column could be eluted by gradient elution. This setup allows operating many columns simultaneously, which further increases the process efficiency. Currently, the biggest problem associated with continuous chromatography is process design since many operation variables are involved in the process, it may not be easy to decouple the impact of different parameters. The mechanistic column model and the comparison method developed in this thesis can be directly applied to provide a robust and efficient process design.

Chapter 7 Appendix

7.1 Supporting tables and figures

Table 7.1. DLS results for mAb monomer and dimer solutions before and after 24 h incubation with CHT Type II in a vial rotated end-over-end at 10 mM Na_2HPO_4 pH 7.0. The radii are somewhat smaller than determined in ref (Reck *et al.*, 2015) but consistent between 0 and 24 h samples.

Protein	Hydrodynamic radius by DLS (nm)
Monomer at time 0	5.3±0.1
Monomer after 24 h	5.3±0.1
Dimer at time 0	6.6±0.1
Dimer after 24 h	6.6±0.1
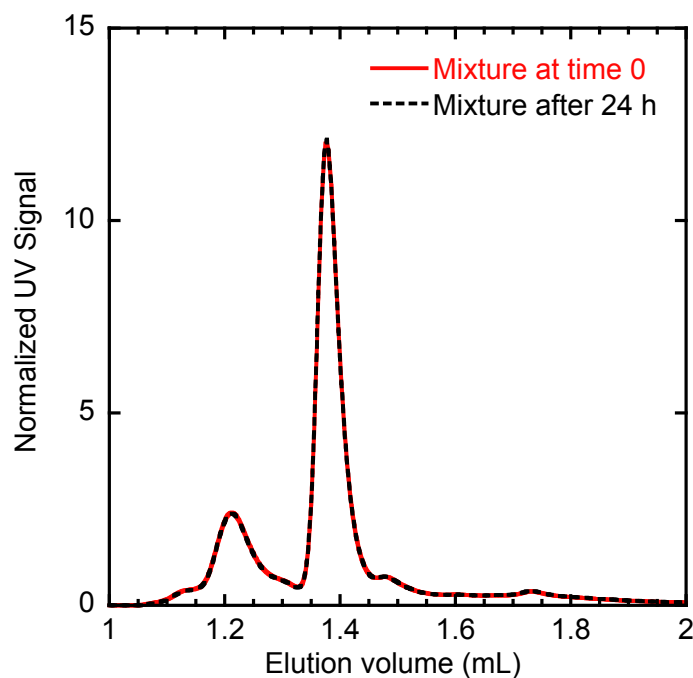
Figure 7.1. Analytical SEC of a monomer-dimer mixture before (red) and after 24 h incubation (black) in 10mM Na_2HPO_4 pH 7.0 in a vial rotated end-over-end for the same conditions of the isotherm measurements.
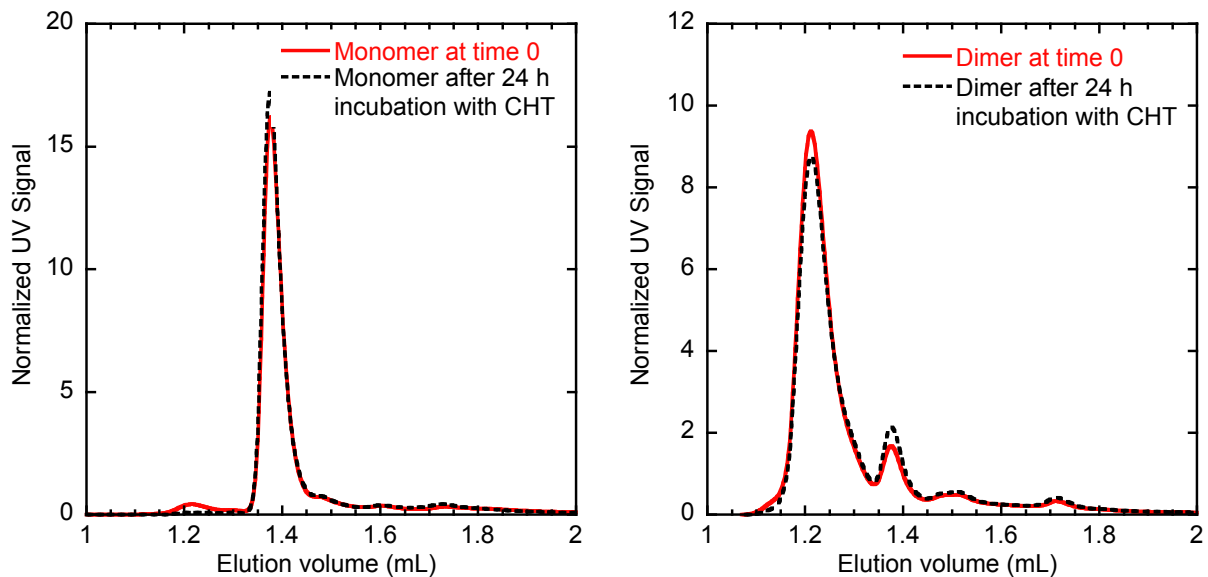
Figure 7.2. Analytical SEC results for monomer and dimer solutions, before (red) and after 24 h incubation (black) with CHT Type II in 10mM Na_2HPO_4 pH 7.0. The chromatograms are normalized to yield the same peak area.
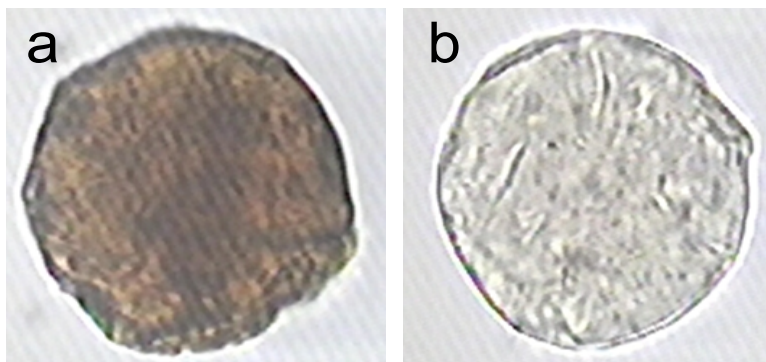
Figure 7.3. Optical microscopy images of CHT Type II immersed in water (a) and immersed in benzyl alcohol (b).
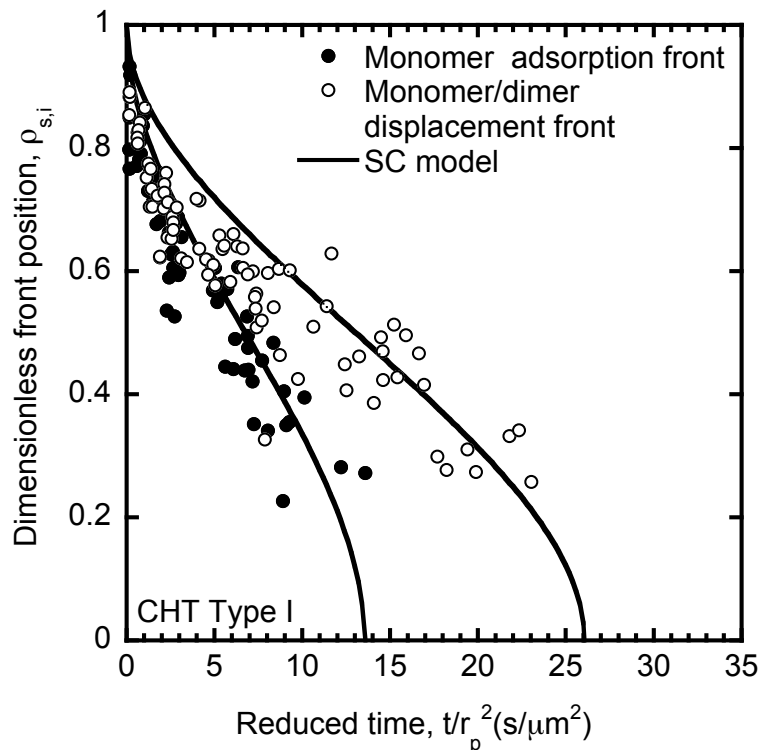
Figure 7.4. Dimensionless position of the monomer adsorption front and the monomer-dimer displacement front during binary adsorption of the mAb monomer-dimer mixture on CHT Type I particles. Lines are calculated from Eq. (3.5) and (3.6) with fitted values of $q_M^* = 17$ mg/mL and $q_D^* = 71$ mg/mL adjusted within the estimated error of the isotherm model predictions. Average deviations between model and data are 7.5% for the monomer and 15% for the dimer.
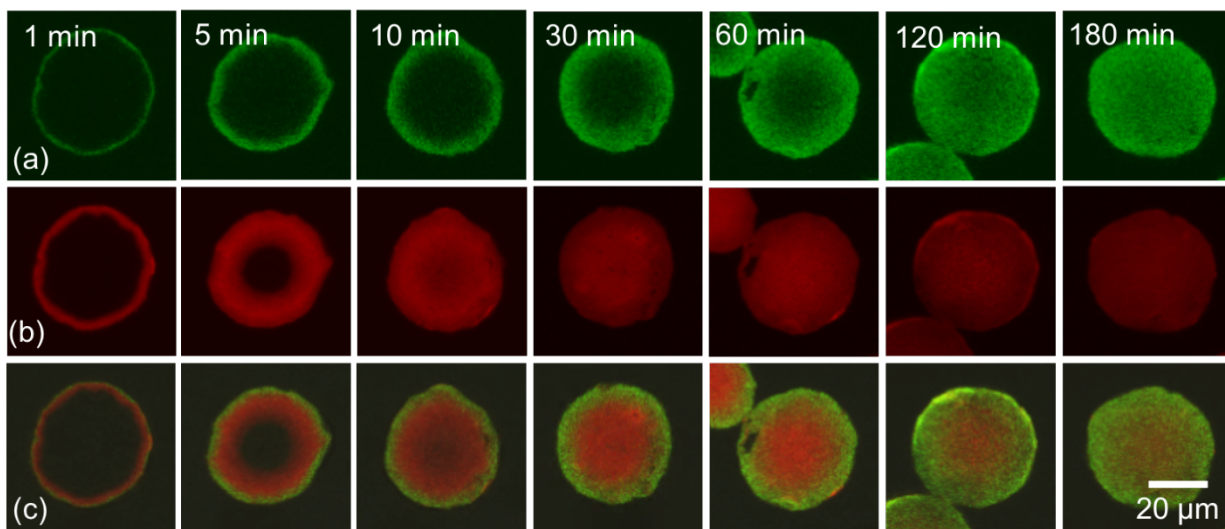
Figure 7.5. CLSM images of binary adsorption of the mAb monomer-dimer in 10 mM Na_2HPO_4, 50 mM NaCl at pH 7 on CHT Type I particles. Monomer and dimer concentrations were 1.5 and 0.5 mg/mL, respectively. (a) dimer, (b) monomer, (c) composite image.

121
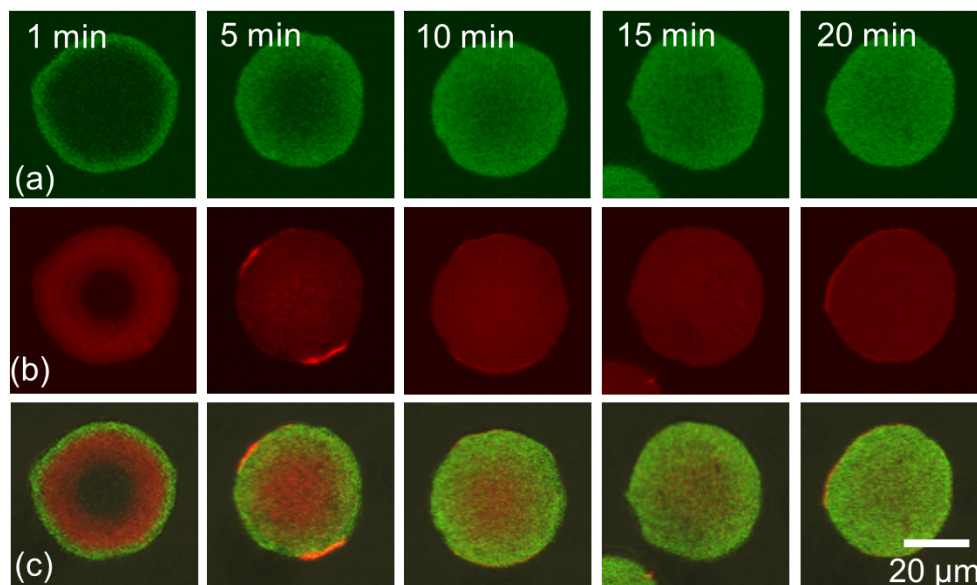
Figure 7.6. CLSM images of binary adsorption of the mAb monomer-dimer in 10 mM Na_2HPO_4, 50 mM NaCl at pH 7 on CHT Type II particles. Monomer and dimer concentrations were 1.5 and 0.5 mg/mL, respectively. (a) dimer, (b) monomer, (c) composite image.
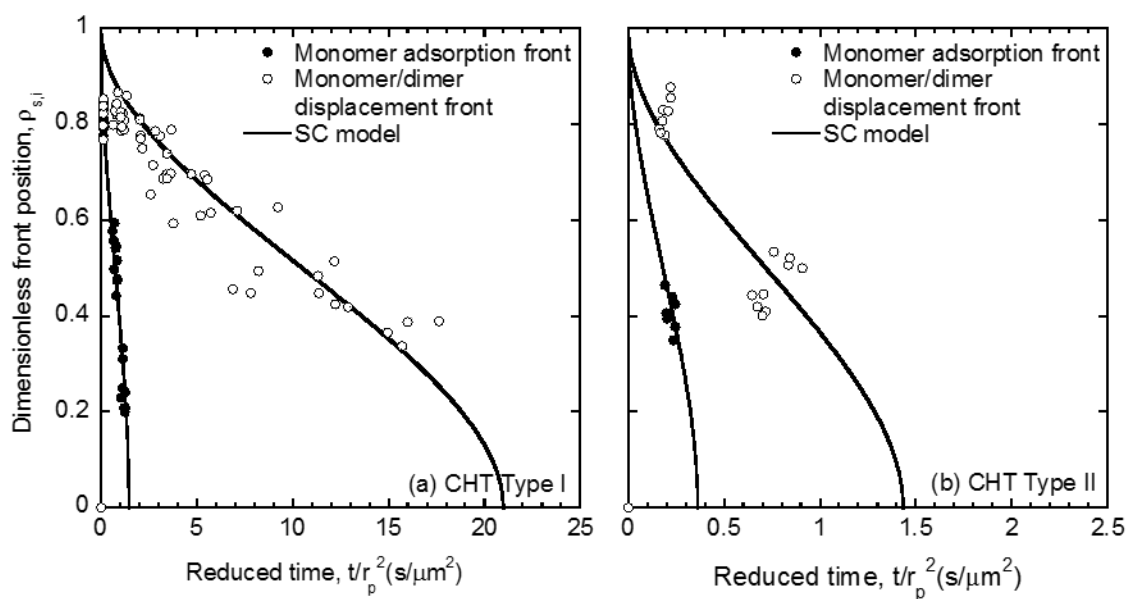
Figure 7.7. Dimensionless position of adsorption front for the mAb monomer and the mAb dimer on (a) CHT Type I particles and (b) CHT Type II particles for the data of Figure 7.5 and Figure 7.6. Lines are based on Eq. (3.5) and (3.6). The R^2 values for the regression are 0.98 and 0.91 for monomer and dimer, respectively, on CHT Type I, and 0.97 and 0.92 for monomer and dimer, respectively, on CHT Type II.

122

7.2 Derivation of analytical solution of peak moment

For the linear isotherm case, analytical solution can be obtained easily in the Laplace domain. The moments of the pulse response peak can then be derived explicitly using the van der Laan theorem as shown, for example, in refs. (Qamar *et al.*, 2014, 2016; Schneider and Smith, 1968). Column dynamics including pore diffusion combined with spreading kinetics is described by the following equations and boundary conditions:

$$\varepsilon D_L \frac{\partial^2 C}{\partial x^2} = u\frac{\partial C}{\partial x} + \varepsilon\frac{\partial C}{\partial t} + (1-\varepsilon)\frac{3D_e}{r_p}\frac{\partial c}{\partial r}\bigg|_{r=r_p} \tag{7.1}$$

$$x = 0, \quad C = C_F \tag{7.2}$$

$$x = L, \quad \frac{\partial C}{\partial x} = 0 \tag{7.3}$$

$$\left(\varepsilon'_p + q_m K_L\right)\frac{\partial c}{\partial t} + r_S = \frac{D_e}{r^2}\frac{\partial}{\partial r}\left(r^2\frac{\partial c}{\partial r}\right) \tag{7.4}$$

$$r = 0, \quad \frac{\partial c}{\partial r} = 0 \tag{7.5}$$

$$r = r_p, \quad c = C \tag{7.6}$$

$$r_S = k_S\left(q_m K_L c - \frac{q_S}{K_S}\right) \tag{7.7}$$

$$\frac{\partial q_S}{\partial t} = r_S \tag{7.8}$$

where, for simplicity, subscript i, identifying the component, has been dropped. In the Laplace domain, these equations become:

$$\frac{d^2\tilde{C}}{dx^2} - \frac{v}{D_L}\frac{d\tilde{C}}{dx} - \frac{s}{D_L}\tilde{C} - \frac{3\phi D_e}{D_L r_p}\frac{d\tilde{c}}{dr}\bigg|_{r=r_p} = 0 \tag{7.9}$$

$$\left(\varepsilon'_p + q_m K_L\right)s\tilde{c} + k_S q_m K_L\left(\tilde{c} - \frac{\tilde{q}_S}{q_m K_L K_S}\right) = \frac{D_e}{r^2}\frac{d}{dr}\left(r^2\frac{d\tilde{c}}{dr}\right) \tag{7.10}$$

$$sq_S = k_S q_m K_L \left(\tilde{c} - \frac{\tilde{q}_S}{q_m K_L K_S} \right) \tag{7.11}$$

Combining Eqs. (7.10) and (7.11) yields:

$$\frac{1}{r^2} \frac{d}{dr} \left(r^2 \frac{d\tilde{c}}{dr} \right) = a\tilde{c} \tag{7.12}$$

where

$$a = \frac{(\varepsilon'_p + q_m K_L)s}{D_e} + \frac{q_m K_L K_S}{D_e} \frac{s}{1 + sK_S/k_S} \tag{7.13}$$

Solution of this ODE subject to boundary conditions (7.5) and (7.6) gives:

$$\tilde{c} = \tilde{C} \frac{\exp\left[(r_p - r)\sqrt{a} \right] \left(-1 + e^{2r\sqrt{a}} \right)}{\left(-1 + e^{2r_p\sqrt{a}} \right) r/r_p} \tag{7.14}$$

$$\left. \frac{d\tilde{c}}{dr} \right|_{r=r_p} = \tilde{C} \left[-\sqrt{a} - \frac{1}{r_p} + \frac{2\sqrt{a}\ e^{2r_p\sqrt{a}}}{-1 + e^{2r_p\sqrt{a}}} \right] \tag{7.15}$$

Finally, combining this equation with Eq. (7.9) and integrating with boundary conditions (7.2) and (7.3) gives the following result for the column transfer function:

$$\left. \frac{d\tilde{c}}{dr} \right|_{r=r_p} = \tilde{C} \left[-\sqrt{a} - \frac{1}{r_p} + \frac{2\sqrt{a}\ e^{2r_p\sqrt{a}}}{-1 + e^{2r_p\sqrt{a}}} \right] \tag{7.16}$$

$$\frac{\tilde{C}}{\tilde{C}^F} = \exp\left\{ \frac{vL}{2D_L} - \frac{vL}{2D_L} \sqrt{1 + \frac{4D_L}{v^2} \left[s + \frac{3\phi D_e}{r_p} \left(-\sqrt{a} - \frac{1}{r_p} + \frac{2\sqrt{a}\ e^{2r_p\sqrt{a}}}{-1 + e^{2r_p\sqrt{a}}} \right) \right]} \right\} \tag{7.17}$$

The central moments of the pulse response peak are found from the following equations:

$$\mu_0 = \lim_{s \to 0} \tilde{C}(s, L) \tag{7.18}$$

$$\mu_1 = -\frac{1}{\mu_0} \lim_{s \to 0} \frac{d\tilde{C}(s, L)}{ds} \tag{7.19}$$

$$\mu_2' = \frac{1}{\mu_0} \lim_{s \to 0} \frac{d^2 \tilde{C}(s,L)}{ds^2} - \left(\mu_1\right)^2 \tag{7.20}$$

$$\mu_3' = -\frac{1}{\mu_0} \lim_{s \to 0} \left[\frac{d^3 \tilde{C}(s,L)}{ds^3} \right] - 3\mu_1\mu_2 + 2\left(\mu_1\right)^3 \tag{7.21}$$

which yield:

$$\mu_1 = \frac{L}{v}\left(1+k'\right) \tag{7.22}$$

$$\mu_2' = \frac{2Lr_p^2 k'^2}{15D_e v \phi} + \frac{2L}{k_S v^3}\left[v^2 \phi q_m K_L K_S^2 + D_L k_S \left(1+k'\right)^2 \right] \tag{7.23}$$

$$\mu_3' = \frac{2L}{105v^5}\left\{ \frac{2r_p^4 v^4 k'^3}{D_e^2 \phi^2} + \frac{42r_p^2 v^2 k'\left[v^2 q_m K_L K_S^2 + D_L k_S k'(1+k')/\phi \right]}{D_e k_S} \right.$$

$$\left. + \frac{315\left[v^4 \phi q_m K_L K_S^3 + 2v^2 \phi D_L q_m K_L k_S K_S^2 \left(1+k_i'\right) + 2D_L^2 k_S^2 (1+k')^3 \right]}{k_S^2} \right\} \tag{7.24}$$

where $k' = \phi\left[\varepsilon_p + q_m K_L\left(1+K_S\right)\right]$ is the retention factor. These expressions were obtained using

Wolfram Mathematica® 10. HETP and peak skew are then calculated as:

$$\text{HETP} = \frac{\mu_2' L}{\left(\mu_1\right)^2} \tag{7.25}$$

$$\text{Peak skew} = \frac{\mu_3'}{\left(\mu_2'\right)^{3/2}} \tag{7.26}$$

Figure 7.8 shows the theoretical effects of the equilibrium constant, K_S, and of the rate constant, k_S, on HETP and peak skew. Calculations are shown as an example for the dimer on CHT Type II at 210 mM Na$^+$ for the conditions of Table 4.3. As seem from this figure, increasing K_S, which corresponds to greater tendency to spread, increases both HETP and peak skew, while increasing k_S which corresponds to faster spreading kinetics, reduces both.
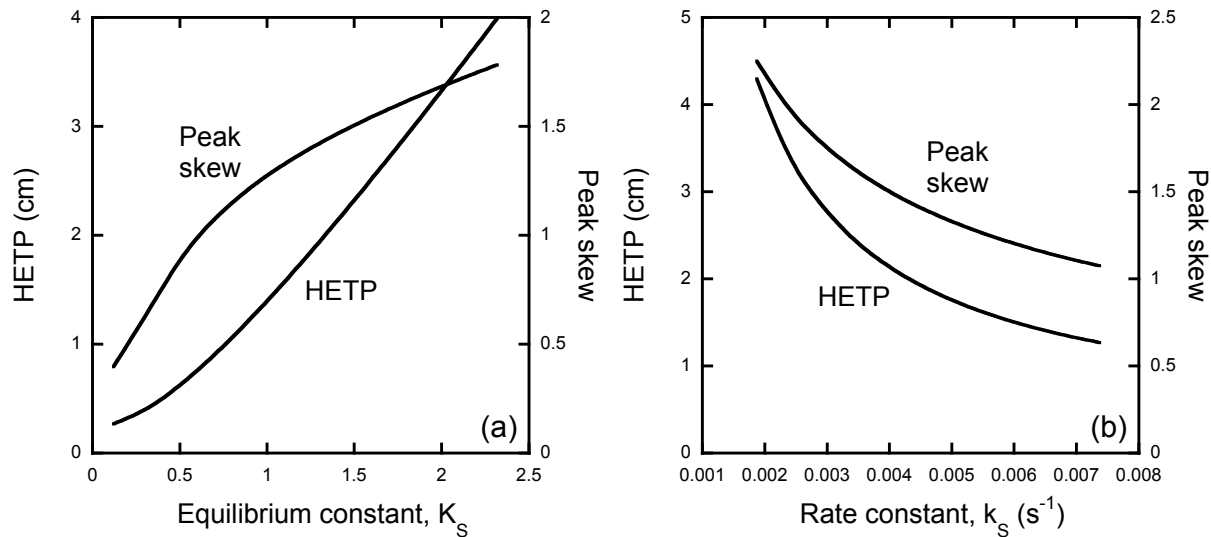
Figure 7.8. Theoretical effects of the equilibrium constant, K_S, and of the rate constant, k_S, in the pore diffusion model with spreading kinetics on HETP and peak skew. Calculations are shown as an example for the dimer on CHT Type II at 210 mM Na^+ for the conditions of Table 4.3. The retention factor was kept constant in these calculations.

7.3 Determination of moments of the isocratic elution peaks from the EMG function

The exponentially modified Gaussian (EMG) function was used to avoid the well-known challenges associated with the direct calculation of the moments by numerically integrating the experimental isocratic elution peaks. For this purpose, the experimental peaks were fitted with the EMG function, defined by the following relationship:

$$C(t) = \frac{A}{2\tau} \exp\left(\frac{\sigma_G^2}{2\tau^2} - \frac{t - t_G}{\tau} \right) \left[1 - \mathrm{erf}\left(\frac{\sigma_G}{\sqrt{2}\tau} - \frac{t - t_G}{\sqrt{2}\sigma_G} \right) \right] \tag{7.27}$$

where A is the area under the peak, t is the time, τ is a constant that quantify the decay time of the system, σ_G is the standard deviation of the Gaussian peak, t_G is the retention time of the Gaussian input function. The three parameters τ, σ_G, and t_G were obtained by regression. The first moment, second central moment, and the peak skew were then calculated from the following relationships:

$$\mu_1 = \tau + t_G \tag{7.28}$$

$$\mu_2' = \sigma_G^2 + \tau_G^2 \tag{7.29}$$

$$\text{Peak skew} = \frac{2\left(\tau_G / \sigma_G\right)^3}{\left[1 + \left(\tau_G / \sigma_G\right)^2\right]^{3/2}} \tag{7.30}$$

Figure 7.9 shows, as an example, the EMG function fitted to the experimental data for the dimer on CHT Type II. The fitted EMG parameters for the data in Figure 4.8 in Chapter 4 are summarized in Table 7.2.
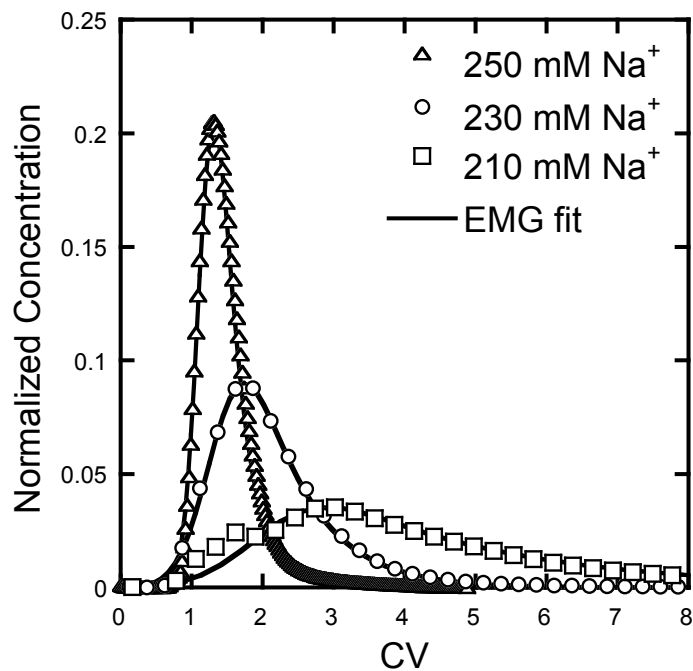
Figure 7.9. Comparison of EMG fitted chromatograms and the normalized isocratic elution peaks obtained for dimer on CHT Type II. Data from Figure 4.8.

Table 7.2. EMG parameters fitted to the experimental data for isocratic elution of monomer and dimer on CHT Type I and Type II (data in Figure 4.8).

CHT Type I				
	Na^+ (mM)	t_G	σ_G	τ
Monomer	280	1.09	0.14	0.10
	230	3.02	0.48	0.50
Dimer	300	1.11	0.18	0.30
	250	1.55	0.40	0.90
CHT Type II				
Monomer	230	1.17	0.13	0.14
	170	3.22	0.45	0.48
	150	6.80	1.1	1.2
Dimer	250	1.15	0.18	0.29
	230	1.36	0.39	0.76
	210	1.85	0.70	1.4

128

7.4 Purification of rapid and sensitive detection of the interaction of human papillomavirus virus-like particles with yeast whole cell RNA using biolayer interferometry

7.4.1 Introduction

The removal of host cell impurities is often a critical problem in the production of biopharmaceuticals, which can be exacerbated when association between target molecules and contaminants occurs. RNA contamination may be a special concern particularly with non-secreted products expressed in eukaryotic cells since a substantial amount of RNA is released during primary recovery. Many types of proteins are known to associate with RNA either specifically, when protein displays special binding sequences or structure motifs, or non-specifically. Because of these concerns, a tool to quickly determine the extent and rate of association is desirable.

A number of techniques have been developed to study biomolecular interactions including filter-binding assays (Stockley, 2009), electrophoretic mobility shift assays (Molloy, 2000), cross-linking immunoprecipitation (CLIP) (Kuo and Allis, 1999; Orlando *et al.*, 1997), and isothermal titration calorimetry (Freire *et al.*, 1990). Although such methods can yield valuable affinity information, they provide little or only indirect kinetic results. In fact, both of the association and the dissociation rate are important to fully understand RNA-protein interactions. Application of biosensor technology, on the other hand, offers the possibility of capturing real-time kinetic data. Two such techniques are surface plasmon resonance (SPR) and biolayer interferometry (BLI). Both can provide association and dissociation rate constants (k_a and k_d, respectively) and thus the dissociation equilibrium constant (K_d). While SPR uses microfluidics to deliver samples to the biosensor surface, BLI uses dip-sensors and stationary shaking plates, thereby avoiding the possibility of clogging and permitting use with crude samples (Abdiche *et al.*, 2008). BLI utilizes

a fiber optic with two light reflecting layers: a thin top layer with a high refractive index (e.g., n > 1.8) and a thick bottom layer with a refractive index intermediate between the solution and the top layer (e.g., n = 1.5 (Tan *et al.*, 2008)). White light traveling through the fiber optic is partially reflected back by the top layer and partially reflected back by the bottom layer. Since the distance traveled by the light reflected by the two layers is different, constructive and destructive interference occurs, resulting in the waveform. If an analyte binds to the bottom layer, the waveform shifts since the optical path length is increased, allowing real time quantification of association and dissociation events. The binding signal, measured by the wavelength shift, is assumed to be directly related to the amount of analyte bound on the tip.

BLI has gained widespread use to detect biomolecular interactions both with proteins and with larger bioparticles. For example, Maun *et al.* (2010) used it to study the interaction between an inhibitor antibody, 5E1, and sonic hedgehog (Shh) using streptavidin (SA) biosensor. Figuera-Losada and LoGrasso (2012) studied the interaction of the c-Jun N-terminal kinase with its substrates ATF2 and c-Jun. Roh et al. (2011) used biotinylated hepatitis C virus (HCV) RNA as a tool to detect HCV viral protein, NS3, since NS3 could specifically bind with viral RNA and facilitate RNA unwinding during the viral replication.

Detection and quantification of biomolecular interactions is also critical for virus-like particles (VLPs) which are receiving increasing attention for a variety of therapeutic applications. For example, Selvarajah *et al.* (2013) immobilized the chikungunya virus VLPs onto amine reactive biosensors to screen the response of two human IgG Fabs, C9 and E8. Auer *et al.* (2015) used histidine-tagged Noroviruses (Nov) VLPs on the Ni-NTA sensors to directly detect its antibodies in human serum. Carvalho *et al.* (2017, 2018) demonstrated the ability of BLI to detect and

quantify label-free influenza VLPs and model mucins,. Additional applications of BLI in vaccine research are in Petersen (2017).

Our focus is to develop a BLI-based method to detect and quantify the interaction of RNA with human papillomavirus virus-like particles (HPV VLPs) recombinant expressed in yeast. As described by Cook *et al.* (1999), different HPV VLP types are produced in large quantity and purified in their assembled state by a combination of chromatographic steps. Clearance of RNA from these products is generally a concern and it is possible for host cell RNA to associate with VLPs, which, in turn, can weaken the digestion ability of nuclease. Any such RNA-VLP association is likely to be dynamic, and knowing the interaction under different conditions is desirable for the design of purification processes. Many HPV VLP serotypes exist. The two used in this work (Type 11 and Type 18) are components of the commercial product GARDASIL®9, a 9-valent HPV vaccine from Merck & Co., Inc.

VLP sensors can be made by immobilizing positively charged VLPs onto a negatively charged biosensor surface via electrostatic interaction. This method provides a way to study the interactions between RNA and VLPs without any modification of either species. Alternatively, immobilized RNA sensors can be made by coupling biotinylated RNA on a streptavidin (SA) coated biosensor surface, taking advantage of extraordinarily high affinity between SA and biotin (Howarth *et al.*, 2006). The specific aims of this work are thus to: (1) construct immobilized VLP and immobilized RNA biosensors; (2) test the ability to detect RNA-VLP interaction; (3) determine binding constants; and (4) determine the effect of solution composition on RNA-VLP association.

131

7.4.2 Materials

Purified recombinant human papillomavirus (HPV) Type 11 and Type 18 VLPs were obtained from Merck & Co., Inc. (Elkton, VA, USA). Frozen samples were thawed at room temperature in a water bath; then 0.015% polysorbate 80 (Amresco, Solon, OH) was added to increase stability. VLPs were stored at -80°C and thawed at room temperature in a water bath before using. The extinction coefficient based on a protein assay and a linear regression is 1.415 mL/(mg of VLP protein×cm) at 280 nm. The VLPs hydrodynamic radius of 34 ± 2 nm was obtained by dynamic light scattering (DLS) using a Dynapro Nanostar unit (Wyatt Technology Corporation, CA). DLS was used to monitor whether aggregation or disruption of the VLPs occurred during analytical processing. HPV VLPs contain 72 L1 pentamers and each L1 protein has a molecular weight of 55 kDa (Joyce *et al.*, 1998). The estimated molecular weight of VLPs is thus around 20,000 kDa. Whole cell RNA from *S. cerevisiae* was obtained from Sigma-Aldrich Co. (St. Louis, MO) as a model for actual RNA impurities encountered during the manufacturing process. The extinction coefficient of RNA is 25 mL/(mg×cm) at 260 nm estimated from a gravimetric determination. The RNA hydrodynamic radius was estimated to be 2.0 ± 0.5 nm also by the DLS. The molecular weight of RNA was estimated as 20 kDa from the empirical equation of ssRNA (Werner, 2010) $r_h = \left(2.05 \pm 0.1\right) \times 10^{-10} \times \left(Mw/340\right)^{(0.58 \pm 0.1)}$. All the samples were buffer-exchanged into the different target buffers with PD 10 desalting columns from GE Healthcare (Piscataway, NJ, USA). All other chemicals were purchased from Thermo Fisher Scientific (Waltham, MA, USA).

The BLI experiments were conducted with a BLItz system from Pall ForteBio Inc. (Menlo Park, CA). All BLI experiments were conducted at room temperature in pH 7 buffers with vibration set at 1500 rpm. Each biosensor was first hydrated with a loading buffer, 250 mM NaCl and 5 mM

Na$_2$HPO$_4$, for 600 s immediately prior to use. All measurements were performed on a fresh tip with 200 μL solution in microtubes.

7.4.3 Quantitative data treatment

In order to extract rate and equilibrium constants, the BLI sensorgrams were fitted with a binding model. Although different rate equations could be considered, we used only the simplest 1:1 binding model:

$$\frac{d\Gamma}{dt} = k_a\left(\Gamma_m - \Gamma\right)C - k_d\Gamma \tag{7.31}$$

where Γ and C are is the analyte concentrations bound to the probe and in solution, respectively, k_a and k_d are the association and dissociation rate constants, and Γ_m is the maximum binding capacity. The dissociation equilibrium constant is $K_d = k_d/k_a$. Integrated forms of this equation for the association phase (with $\Gamma\big|_{t=0} = 0$ and $C = C_0$) and for the dissociation phase (with $\Gamma\big|_{t=t_0} = \Gamma_0$ and $C = 0$) are (O'Shannessy et $al.$, 1993):

$$\Gamma_a(t) = \frac{\Gamma_m C_0}{K_d + C_0}\left\{1 - \exp\left[-\left(K_d + C_0\right)k_a t\right]\right\} \tag{7.32}$$

$$\Gamma_d(t) = \Gamma_0 \exp\left[-k_d\left(t - t_0\right)\right] \tag{7.33}$$

where t_0 is the start time of the dissociation phase. The MATLAB (The Mathworks, Natick, ME, USA) regression routine $lsqnonlin$ was used to determine best-fit values of k_a, K_d, and Γ_m.

7.4.4 Results and discussion

7.4.4.1 Immobilized VLP biosensors

Amine-reactive second generation (AR2G) probes were obtained from Pall ForteBio Inc. (Menlo Park, CA) and were used for immobilizing VLPs. The surface of these probes is covered by

carboxyl groups, which are negatively charged at pH 7 and which can be expected to interact favorably with positively charged VLPs even at relatively high ionic strengths. For example, Wu *et al.* (2016) found that HPV VLPs were strongly bound to the negatively charged resin POROS HS at NaCl concentrations as high as 500 mM. Experiments with the immobilized VLP biosensors were listed in the caption of Figure 7.10.

Figure 7.10A and B show the experimental sensorgrams (solid lines) for the VLP immobilization and RNA association/dissociation phases, respectively, for Type 18 VLPs, while Figure 7.10C and D show the corresponding sensorgrams for Type 11 VLPs. As seen from Figure 7.10A and C, the VLP loading is highly reproducible for multiple BLI probes and for both VLP types reaching a binding signal of 2.0 nm with a standard deviation of 0.1 at the end of the loading phase II (150 s). The binding signal during the ensuing RNA association and dissociation phases (III and IV, respectively), shown in Figure 7.10B and D, demonstrate that RNA binding to the VLP-functionalized probes occurs primarily with Type 18 VLPs. Very little association appears to occur with Type 11. In the case of Type 18, the binding curves are clearly dependent on the RNA concentration in the 0.5-7.8 μM range. It should be noted that the association/dissociation signals for both VLP types are shown flipped as absolute deviations from the baseline. The actual signals were in fact negative, which also observed by others for DNA aptamer and cells (Bruno, 2015; Verzijl *et al.*, 2017), occurs as a result of the large size of the VLPs, which likely causes the interaction surface to be located at a large distance away from the biosensor surface.

Lines calculated according to Eqs. (7.32) and (7.33) are shown in Figure 7.10B using the fitted parameters summarized in Table 7.3, which are given along with the estimated error of their regressed values. Note that the fitting of the dissociation curves was quite poor, in part because of the low signal and in part because the assumed 1:1 binding stoichiometry is likely

134

inappropriate for this case. In reality, it is likely that multiple RNA molecules interact with each immobilized VLP.
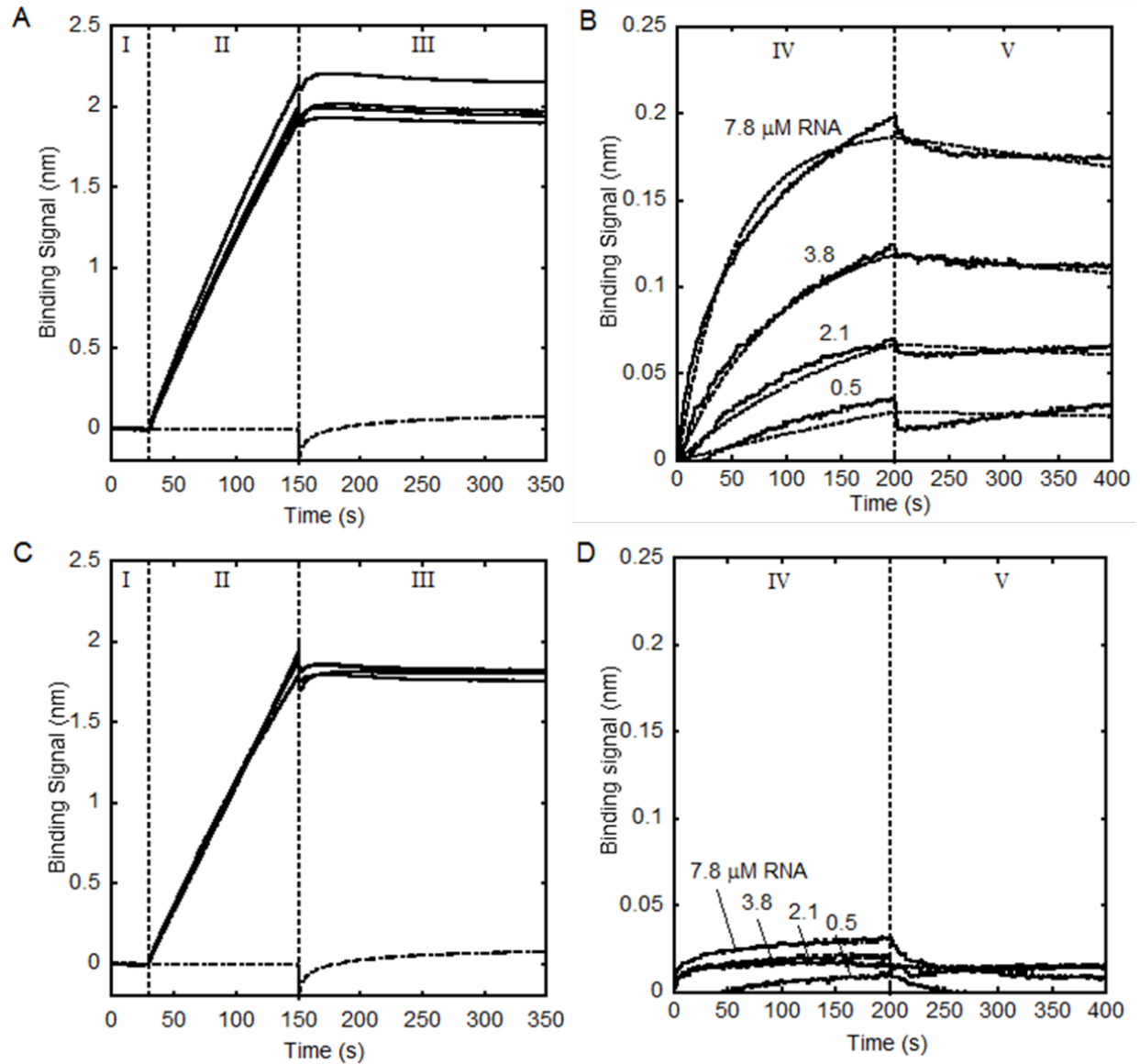
Figure 7.10. Sensorgrams obtained with immobilized-VLP BLI probes and yeast RNA using HPV VLP Type 18 (A and B) and HPV VLP Type 11 (C and D). Solid lines are data and dashed lines are fitted lines. The vertical dashed lines denote: Phase I – equilibration in VLP binding buffer 250 mM NaCl, 5 mM Na_2HPO_4, pH 7; Phase II – VLPs loading in binding buffer; Phase III – wash in binding buffer with 1% BSA Phase IV – association with serially diluted RNA samples in binding buffer with 1% BSA; Phase V – dissociation in binding buffer with 1% BSA. The curves in Figures 1B and 1D are aligned at the end of phase III and plotted on a different vertical scale. Dash-dotted lines show the results obtained for a blank probe without exposure to VLPs.

7.4.4.2 Immobilized RNA biosensors

Biosensors obtained by immobilizing the VLPs via electrostatic interaction have the advantage of simplicity but are potentially sensitive to the buffer composition. Moreover, immobilizing a large ligand and binding a smaller one is expected to give a weaker signal. Thus, immobilized RNA biosensors were prepared using streptavidin (SA) probes also obtained from Pall ForteBio Inc. (Menlo Park, CA, USA). These probes contain surface bound SA, which can be used to couple biotinylated molecules. For this purpose, RNA was biotinylated using biotinamidohexanoic acid hydrazide through the selective periodate-mediated oxidation of the RNA 3'terminal ribose *cis*-diol RNA (Li *et al.*, 2010).Experimental steps with the immobilized RNA biosensors were listed in the caption of Figure 7.11.

Although, as shown above, immobilized VLP biosensors were able to distinguish between Type 18 and 11 with regards to the ability to associate with RNA, only a relatively small signal response (< 0.2 nm) was obtained due to the small size of RNA. This low response influences the accuracy of parameter determination. Additionally, it is likely that immobilization of VLPs depends on the buffer ionic strength, which requires conducting measurements at a constant buffer composition.

Figure 7.11 shows sample results obtained with immobilized-RNA probes. Figure 7.11A shows the raw sensorgrams obtained during the preparation of these sensors. As seen in this figure, loading RNA on different SA probes (phase II) gave highly reproducible results. Greater signal variations from probe to probe were, however, obtained during the subsequent casein passivation step (phase III). This phase is characterized by a sharp signal increase, which is due to the higher refractive index of the casein solution, followed by a relaxation of the signal. A further sharp drop occurs in phase IV when the probes are again immersed in the casein-free RNA load buffer.

137

Little further change occurs in the final equilibration buffer containing 0.015% polysorbate 80 (phase V). The signal obtained for a blank run without RNA is shown by the dash-dotted line in this figure and follows the refractive index changes.

Figure 7.11B shows the sensorgrams obtained for the five probes of Figure 7.11A at five different VLP concentrations for both association and dissociation phases (VI and VII, respectively) in a pH 7 buffer containing 5 mM Na$_2$HPO$_4$ and 250 mM NaCl. As done previously, signals are shown flipped and normalized by the signal obtained for each probe at the end the preceding phase V. As seen in this figure, the normalized signals follow consistent trends with respect to the VLP concentration. Calculations based on Eqs. (7.32) and (7.33) using the fitted parameters in Table 7.3 are shown by the dashed lines. A significantly better fit is obtained compared to that obtained for the immobilized VLP probes; this is likely because the assumed 1:1 binding stoichiometry is more realistic for this case.

Figure 7.11C-D give additional examples of results showing the effect of NaCl concentration on VLP association and dissociation on the immobilized RNA probe in the same pH 7 buffer containing 5 mM Na$_2$HPO$_4$. The fitted curves (dashed lines) with the parameter values in Table 7.3 provide a good description of the data. Results obtained for pH 7 buffers containing 250 mM NaCl but with different Na$_2$HPO$_4$ concentrations are also shown in Table 7.3. As seen from these results, both k_a and K_d appear to correlate to ionic strength with k_a decreasing and K_d increasing as the ionic strength increases regardless of whether this increase is because of the addition of NaCl or phosphate. This result suggests that the immobilized RNA/VLP interaction is driven by electrostatic forces that become weaker as the ionic strength increases reducing both association rate and affinity. No specific effect associated with phosphate is evident from these results.

Comparing the apparent rate constant k_a based on 1:1 stoichiometry obtained for immobilized VLP probes with that obtained with the immobilized RNA probes under the same conditions shows that the former is many times lower than the latter. This result is an indication that the association stoichiometry is quite different in the two cases with many RNA molecules binding to each immobilized VLP compared to the other way around.

7.4.5 Conclusions

BLI sensors are useful in detecting and quantifying the interaction of RNA and HPV VLPs. The sensors can be constructed either by immobilizing VLPs by adsorption on the surface of positively charged probes or by coupling biotinylated RNA on streptavidin-functionalized probes. The choice of method depends on the purpose of the experiments. The former approach has the advantage of simplicity and can distinguish the ability of different HPV VLP types to interact with RNA. The latter has the advantage of robustness and can be used to explore the effects of buffer composition on the interaction without concerns for affecting the probe functionality. For quantification purposes, immobilizing RNA appears to be preferable. Binding kinetics and equilibrium constants were determined by applying a standard 1:1 interaction model to the Type 18 VLP data. Consistent results were obtained for the immobilized RNA probes. However, determination of the dissociation constant from for the immobilized VLP probes was not possible using this simple interaction model likely because of the higher-order binding stoichiometry when the much smaller RNA interacts with the immobilized VLPs.

The overall detection over a range of five different analyte concentrations could be completed within 15 min with the one-channel BLItz system. Using multichannel equipment, such as the Octet system, the method can be implemented as a high-throughput process.
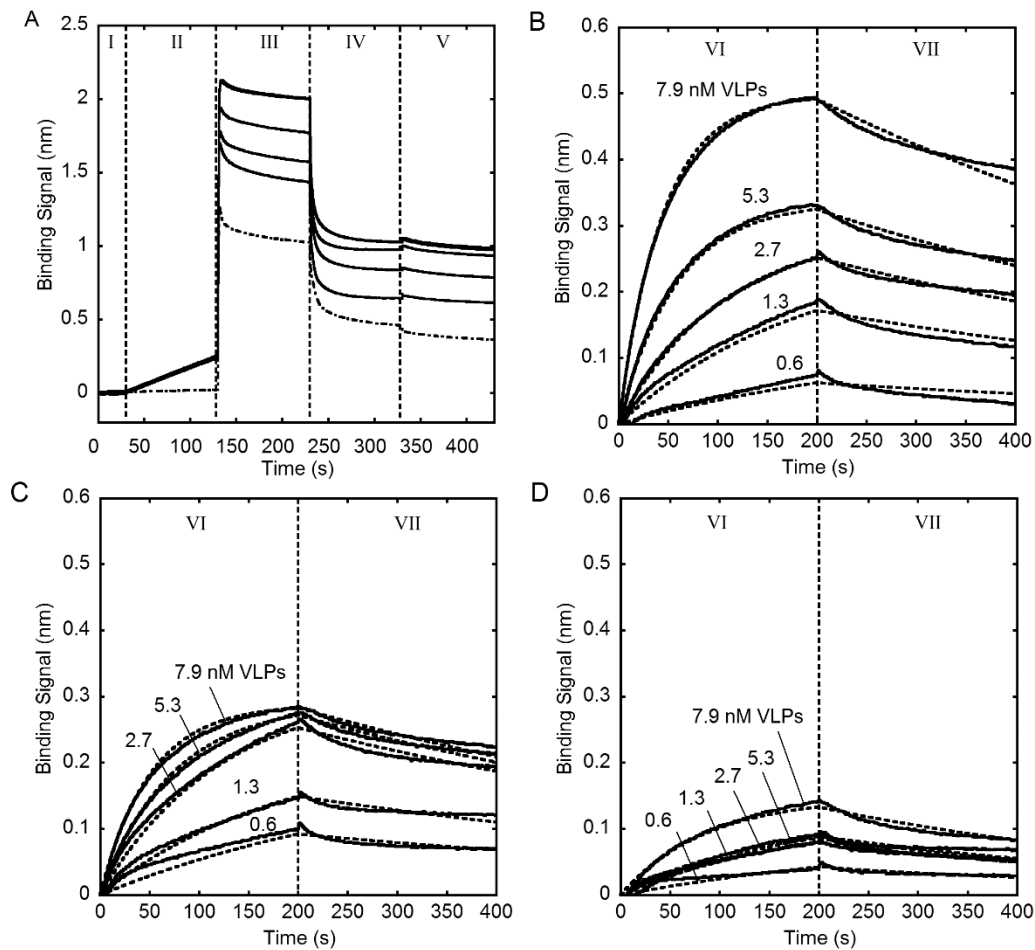
Figure 7.11. Sensorgrams obtained with immobilized-RNA BLI probes using HPV VLP Type 18. Solid lines are data and dashed lines are fitted lines. A: raw sensorgrams for probe functionalization. B: VLP-RNA interaction in 5 mM Na_2HPO_4 pH 7 buffer with 250 mM NaCl. C: VLP-RNA interaction in 5 mM Na_2HPO_4 pH 7 buffer with 300 mM NaCl. D: VLP-RNA interaction in 5 mM Na_2HPO_4 pH 7 buffer with 340 mM NaCl. The vertical dashed lines denote: Phase I – equilibrium in loading buffer (5 mM Na_2HPO_4/250 mM NaCl). Phase II – coupling of biotinyltaed RNA in loading buffer. Phase III – passivation with 1X casein blocking buffer diluted in loading buffer. Phase IV – wash in loading Phase V – equilibration in binding buffer with 0.015% polysorbate 80. Phase VI – association with serially diluted HPV18 VLPs in binding buffer with 0.015% polysorbate 80. Phase VII – dissociation in binding buffer with 0.015% polysorbate 80. Timescales were adjusted to zero at the beginning of association.

Table 7.3. Kinetic and equilibrium constants for HPV VLP Type 18 interaction with yeast RNA at pH 7.

Biosensor	[NaCl] (mM)	[Na$_2$HPO$_4$] (mM)	Ionic strength (mM)	k_a (10^6 M^{-1}s^{-1})	K_d (10^{-9} M)	Γ_m (nm)
Immobilized VLP sensors	250	5	263	0.0026 ± 0.0002	175 ± 12	0.154 ± 0.025
Immobilized RNA sensors	250	5	263	3.12 ± 0.03	0.48 ± 0.01	0.394 ± 0.007
	300	5	313	2.02 ± 0.04	0.76 ± 0.02	0.342 ± 0.011
	340	5	353	1.09 ± 0.05	2.16 ± 0.10	0.305 ± 0.039
	250	30	327	2.25 ± 0.04	0.60 ± 0.02	0.321 ± 0.017
	250	50	378	1.52 ± 0.05	2.10 ± 0.15	0.278 ± 0.043

Reference

Abbas, S.A., Sharma, V.K., Patapoff, T.W., and Kalonia, D.S. (2012) *Opposite effects of polyols on antibody aggregation: Thermal versus mechanical stresses. Pharm. Res.*, **29**, 683–694.

Abdiche, Y., Malashock, D., Pinkerton, A., and Pons, J. (2008) *Determining kinetics and affinities of protein interactions using a parallel real-time label-free biosensor, the Octet. Anal. Biochem.*, **377**, 209–217.

Almagro, J.C., Daniels-Wells, T.R., Perez-Tapia, S.M., and Penichet, M.L. (2018) *Progress and challenges in the design and clinical development of antibodies for cancer therapy. Front. Immunol.*, **8**, 1751.

Aoyama, K. and Chiba, J. (1993) *Separation of different molecular forms of mouse IgA and IgM monoclonal antibodies by high-performance liquid chromatography on spherical hydroxyapatite beads. J. Immunol. Methods*, **162**, 201–210.

Arosio, P., Rima, S., and Morbidelli, M. (2013) *Aggregation mechanism of an IgG2 and two IgG1 monoclonal antibodies at low pH: From oligomers to larger aggregates. Pharm. Res.*, **30**, 641–654.

Asenjo, J.A. and Andrews, B.A. (2009) *Protein purification using chromatography: Selection of type, modelling and optimization of operating conditions. J. Mol. Recognit.*, **22**, 65–76.

Auer, S., Koho, T., Uusi-Kerttula, H., Vesikari, T., Blazevic, V., and Hytönen, V.P. (2015) *Rapid and sensitive detection of norovirus antibodies in human serum with a biolayer interferometry biosensor. Sensors Actuators, B Chem.*, **221**, 507–514.

Bankston, T.E., Dattolo, L., and Carta, G. (2010) *pH Transients in hydroxyapatite chromatography columns-Experimental evidence and phenomenological modeling. J. Chromatogr. A*, **1217**, 2123–2131.

Beck, A., Goetsch, L., Dumontet, C., and Corvaïa, N. (2017) *Strategies and challenges for the next generation of antibody-drug conjugates. Nat. Rev. Drug Discov.*, **16**, 315–337.

Bee, J.S., Davis, M., Freund, E., Carpenter, J.F., and Randolph, T.W. (2010) *Aggregation of a monoclonal antibody induced by adsorption to stainless steel. Biotechnol. Bioeng.*, **105**, 121–129.

Borg, N., Brodsky, Y., Moscariello, J., Vunnum, S., Vedantham, G., Westerberg, K., and Nilsson, B. (2014) *Modeling and robust pooling design of a preparative cation-exchange chromatography step for purification of monoclonal antibody monomer from aggregates. J.*

Chromatogr. A, **1359**, 170–181.

Borrebaeck, C.A. and Carlsson, R. (2001) *Human therapeutic antibodies. Curr. Opin. Pharmacol.*, **1**, 404–408.

Boschetti, E. and Jungbauer, A. (2000) *Separation of antibodies by liquid chromatography. Sep. Sci. Technol.*, **2**, 535–632.

Brinkmann, U. and Kontermann, R.E. (2017) *The making of bispecific antibodies. MAbs*, **9**, 182–212.

Brooks, C.A. and Cramer, S.M. (1992) *Steric mass‑action ion exchange: Displacement profiles and induced salt gradients. AIChE J.*, **38**, 1969–1978.

Bruno, J.G. (2015) *Predicting the uncertain future of aptamer-based diagnostics and therapeutics. Molecules*, **20**, 6866–6887.

Buss, N.A.P.S., Henderson, S.J., McFarlane, M., Shenton, J.M., and De Haan, L. (2012) *Monoclonal antibody therapeutics: History and future. Curr. Opin. Pharmacol.*, **12**, 615–622.

Carta, G. and Jungbauer, A. (2010) *Protein chromatography: process development and scale-up*. WILEY-VCH Verlag.

Carta, G., Ubiera, A.R., and Pabst, T.M. (2005) *Protein mass transfer kinetics in ion exchange media: Measurements and interpretations. Chem. Eng. Technol.*, **28**, 1252–1264.

Carvalho, S.B., Moleirinho, M.G., Wheatley, D., Welsh, J., Gantier, R., Alves, P.M., et al. (2017) *Universal label-free in-process quantification of influenza virus-like particles. Biotechnol. J.*, **12**, 1700031.

Carvalho, S.B., Moreira, A.S., Gomes, J., Carrondo, M.J.T., Thornton, D.J., Alves, P.M., et al. (2018) *A detection and quantification label-free tool to speed up downstream processing of model mucins. PLoS One*, **13**, 1–14.

Chames, P., Van Regenmortel, M., Weiss, E., and Baty, D. (2009) *Therapeutic antibodies: Successes, limitations and hopes for the future. Br. J. Pharmacol.*, **157**, 220–233.

Cook, J.C., Joyce, J.G., George, H. a, Schultz, L.D., Hurni, W.M., Jansen, K.U., et al. (1999) *Purification of virus-like particles of recombinant human papillomavirus type 11 major capsid protein L1 from Saccharomyces cerevisiae. Protein Expr. Purif.*, **17**, 477–484.

Creasy, A., Reck, J., Pabst, T., Hunter, A., Barker, G., and Carta, G. (2018) *Systematic interpolation method predicts antibody monomer-dimer separation by gradient elution*

chromatography at High protein Loads. Biotechnol. J., **14**, 1–9.

Cromwell, M.E.M., Hilario, E., and Jacobson, F. (2006) *Protein aggregation and bioprocessing. AAPS J.*, **8**, E572–E579.

Cummings, L.J., Snyder, M.A., and Brisack, K. (2009) *Protein chromatography on hydroxyapatite columns*. In: *Methods in Enzymology* , pp. 387–404.

Czajkowsky, D.M., Hu, J., Shao, Z., and Pleass, R.J. (2012) *Fc-fusion proteins: New developments and future perspectives. EMBO Mol. Med.*, **4**, 1015–1028.

Dengl, S., Wehmer, M., Hesse, F., Lipsmeier, F., Popp, O., and Lang, K. (2013) *Aggregation and chemical modification of monoclonal antibodies under upstream processing conditions. Pharm. Res.*, **30**, 1380–1399.

Diedrich, J., Heymann, W., Leweke, S., Hunt, S., Todd, R., Kunert, C., et al. (2017) *Multi-state steric mass action model and case study on complex high loading behavior of mAb on ion exchange tentacle resin. J. Chromatogr. A*, **1525**, 60–70.

Ecker, D.M., Jones, S.D., and Levine, H.L. (2015) *The therapeutic mnoclonal antibody market. MAbs*, **7**, 9–14.

Fargues, C., Bailly, M., Grevillot, G., Laboratoire, L., Ensic-cnrs, C., Bp, G., and Cedex, N. (1998) *Adsorption of BSA and hemoglobin on hydroxyapatite support : equilibria and multicomponent dynamic adsorption. Adsorption*, **4**, 5–16.

Fee, C.J. and Van Alstine, J.M. (2004) *Prediction of the viscosity radius and the size exclusion chromatography behavior of PEGylated proteins. Bioconjug. Chem.*, **15**, 1304–1313.

Felinger, A. and Guiochon, G. (1998) *Comparing the optimum performance of the different modes of preparative liquid chromatography. J. Chromatogr. A*, **796**, 59–74.

Ferri, C., Zignego, A.L., and Pileri, S.A. (2002) *Cryoglobulins. J. Clin. Pathol.*, **55**, 4–13.

Figuera-Losada, M. and LoGrasso, P. V. (2012) *Enzyme kinetics and interaction studies for human JNK1β1 and substrates Activating Transcription Factor 2 (ATF2) and c-Jun N-terminal kinase (c-Jun). J. Biol. Chem.*, **287**, 13291–13302.

Freire, E., Mayorga, O.L., and Straume, M. (1990) *Isothermal titration calorimetry. Anal. Chem.*, **62**, 950A-959A.

Gagnon, P. (2008) *Improved antibody aggregate removal by hydroxyapatite chromatography in the presence of polyethylene glycol. J. Immunol. Methods*, **336**, 222–228.

Gagnon, P., Cheung, C.-W., and Yazaki, P.J. (2009) *Cooperative multimodal retention of IgG,*

fragments, and aggregates on hydroxyapatite. J Sep Sci., **32**, 3857–3865.

Gagnon, P., Ng, P., Zhen, J., Aberin, C., He, J., Mekosh, H., et al. (2006) *A ceramic hydroxyapatite– based purification platform. Bioprocess Int.*, **4**, 50–60.

Gallant, S.R., Vunnum, S., and Cramer, S.M. (1996) *Optimization of preparative ion-exchange chromatography of proteins: Linear gradient separations. J. Chromatogr. A*, **725**, 295–314.

Ghose, S., McNerney, T.M., and Hubbard, B. (2002) *pH transitions in ion-exchange systems: Role in the development of a cation-exchange process for a recombinant protein. Biotechnol. Prog.*, **18**, 530–537.

Giddings, J.C. (1991) *Unified separation science.* Wiley.

Giovannini, R. and Freitag, R. (2000) *Comparison of different types of ceramic hydroxyapatite for the chromatographic separation of plasmid DNA and a recombinant anti-Rhesus D antibody. Bioseparation*, **9**, 359–368.

Giovannini, R. and Freitag, R. (2002) *Continuous Isolation of Plasmid DNA by Annular Chromatography. Biotechnol. Bioeng.*, **77**, 445–454.

Glueckauf, E. (1955) *Theory of chromatography. Part 10.—Formulæ for diffusion into spheres and their application to chromatography. Trans. Faraday Soc.*, **51**, 1540–1551.

Goldstein, G. (1987) *Overview of the development of Orthoclone OKT3: monoclonal antibody for therapeutic use in transplantation. Transplant. Proc.*, **19**, 1–6.

Gorbunoff, M.J. (1984a) *The interaction of proteins with hydroxyapatite: I. Role of protein charge and structure. Anal. Biochem.*, **136**, 425–432.

Gorbunoff, M.J. (1984b) *The interaction of proteins with hydroxyapatite: II. Role of acidic and basic groups. Anal. Biochem.*, **136**, 433–439.

Gorbunoff, M.J. and Timasheff, S.N. (1984) *The interaction of proteins with hydroxyapatite: III. Mechanism. Anal. Biochem.*, **136**, 440–445.

Grilo, A.L. and Mantalaris, A. (2019) *The increasingly human and profitable monoclonal antibody market. Trends Biotechnol.*, **37**, 9–16.

Grushka, E. (1972) *Characterization of exponentially modified Gaussian peaks in chromatography. Anal. Chem.*, **44**, 1733–1738.

Guélat, B., Ströhlein, G., Lattuada, M., Delegrange, L., Valax, P., and Morbidelli, M. (2012) *Simulation model for overloaded monoclonal antibody variants separations in ion-exchange chromatography. J. Chromatogr. A*, **1253**, 32–43.

Guiochon, G. (2002) *Preparative liquid chromatography*. J. Chromatogr. A, **965**, 129–161.

Guo, J. and Carta, G. (2014) *Unfolding and aggregation of a glycosylated monoclonal antibody on a cation exchange column . Part II . Protein structure effects by hydrogen deuterium exchange mass spectrometry*. J. Chromatogr. A, **1356**, 129–137.

Guo, J., Creasy, A.D., Barker, G., and Carta, G. (2016) *Surface induced three-peak elution behavior of a monoclonal antibody during cation exchange chromatography*. J. Chromatogr. A, **1474**, 85–94.

Guo, J., Zhang, S., and Carta, G. (2014) *Unfolding and aggregation of a glycosylated monoclonal antibody on a cation exchange column . Part I . Chromatographic elution and batch adsorption behavior*. J. Chromatogr. A, **1356**, 117–128.

Gzil, P., Baron, G. V, and Desmet, G. (2003) *Computational fluid dynamics simulations yielding guidelines for the ideal internal structure of monolithic liquid chromatography*. J. Chromatogr. A, **991**, 169–188.

Hagel, L., Östberg, M., and Andersson, T. (1996) *Apparent pore size distributions of chromatography media*. J. Chromatogr. A, **743**, 33–42.

Haimer, E., Tscheliessnig, A., Hahn, R., and Jungbauer, A. (2007) *Hydrophobic interaction chromatography of proteins IV Kinetics of protein spreading*. J. Chromatogr. A, **1139**, 84–94.

Hanke, A.T. and Ottens, M. (2014) *Purifying biopharmaceuticals: Knowledge-based chromatographic process development*. Trends Biotechnol., **32**, 210–220.

Holzmann, D., Holzinger, D., Hesser, G., Schmidt, T., and Knör, G. (2009) *Hydroxyapatite nanoparticles as novel low-refractive index additives for the long-term UV-photoprotection of transparent composite materials*. J. Mater. Chem., **19**, 8102–8106.

Horenstein, A.L., Crivellin, F., Funaro, A., Said, M., and Malavasi, F. (2003) *Design and scaleup of downstream processing of monoclonal antibodies for cancer therapy: From research to clinical proof of principle*. J. Immunol. Methods, **275**, 99–112.

Hori, S., Ohtani, S., Miyazaka, K., Ishikawa, T., and Tanabe, H. (1990) *Separation of high-molecular mass RNAs by high-performance liquid chromatography on hydroxyapatite*. J. Chromatogr. A, **515**, 611–619.

Howarth, M., Chinnapen, D.J.F., Gerrow, K., Dorrestein, P.C., Grandy, M.R., Kelleher, N.L., et al. (2006) *A monovalent streptavidin with a single femtomolar biotin binding site. Nat.*

Methods, **3**, 267–273.

Hunter, A.K. and Carta, G. (2001) *Effects of bovine serum albumin heterogeneity on frontal analysis with anion-exchange media*. *J. Chromatogr. A*, **937**, 13–19.

Joyce, J.G., George, H.A., Hofman, K.J., Jansen, K.U., and Neeper., M.P. (1998) *Recombinant human papillomavirus type 18 vaccine*. U.S. Patent No. 5,820,870.

Jungabauer, A., Tauer, C., Reiter, M., Purtscher, M., Wenisch, E., Steindl, F., et al. (1989) *Comparison of protein A, protein G and copolymerized hydroxyapatite for the purification of human monoclonal antibodies*. *J. Chromatogr. A*, **476**, 257–268.

Jungbauer, A., Hahn, R., Deinhofer, K., and Luo, P. (2004) *Performance and characterization of a nanophased porous hydroxyapatite for protein chromatography*. *Biotechnol. Bioeng.*, **87**, 364–375.

Jungbauer, A., Machold, C., and Hahn, R. (2005) *Hydrophobic interaction chromatography of proteins: III. Unfolding of proteins upon adsorption*. *J. Chromatogr. A*, **1079**, 221–228.

Jungbauer, A., Tauer, C., Reiter, M., Purtscher, M., Wenisch, E., Steindl, F., et al. (1989) *Comparision of Protein A, Protein G and copolymerized hydroxyapatite for the purification of human monoclonal antibodies*. *J. Chromatogr.*, **476**, 257–268.

Kaltenbrunner, O., Diaz, L., Hu, X., and Shearer, M. (2016) *Continuous bind-and-elute protein A capture chromatography: Optimization under process scale column constraints and comparison to batch operation*. *Biotechnol. Prog.*, **32**, 938–948.

Katti, A.M. and Jagland, P. (1998) *Development and optimization of industrial scale chromatography for use in manufacturing*. *Analusis*, **26**, 38–54.

Kawasaki, T. (1991) *Hydroxyapatite as a liquid chromatographic packing*. *J. Chromatogr. A*, **544**, 147–184.

Kawasaki, T., Nikura, M., and Kobayashi, Y. (1990) *Fundamental study of hydroxyapatite high-performance liquid chromatography. Direct experimental confirmation of the exsistence of two types of adsorbing surface on the hydroxyapatite crystal*. *J. Chromatogr.*, **515**, 125–148.

Kiese, S., Papppenberger, A., Friess, W., and Mahler, H. (2012) *Shaken, not stirred: Mechanical stress testing of an IgG1 antibody*. *J. Pharm. Sci.*, **101**, 322–332.

Kluters, S., Wittkopp, F., Jöhnck, M., and Frech, C. (2016) *Application of linear pH gradients for the modeling of ion exchange chromatography: Separation of monoclonal antibody*

monomer from aggregates. J. Sep. Sci., **39**, 663–675.

Köhler, G. and Milstein, C. (1975) *Continuous cultures of fused cells secreting antibody of predefined specificity. Nature*, **256**, 495.

Kopaciewicz, W., Rounds, M.A., Fausnaugh, J., and Regnier, F.E. (1983) *Retention model for high-performance ion-exchange chromatography. J. Chromatogr. A*, **266**, 3–21.

Kozlowski, S. and Swann, P. (2006) *Current and future issues in the manufacturing and development of monoclonal antibodies. Adv. Drug Deliv. Rev.*, **58**, 707–722.

Kramarczyk, J.F., Kelley, B.D., and Coffman, J.L. (2008) *High-throughput screening of chromatographic separations: II. Hydrophobic interaction. Biotechnol. Bioeng.*, **100**, 707–720.

Kumar, V. and Rathore, A.S. (2014) *Two-stage chromatographic separation of aggregates for monoclonal antibody therapeutics. J. Chromatogr. A*, **1368**, 155–162.

Kuo, M.-H. and Allis, C.D. (1999) *In vivo cross-linking and immunoprecipation for studying dynamic protein: DNA associations in a chromatin environment. Methods*, **19**, 425–433.

Leavy, O. (2010) *Therapeutic antibodies: Past, present and future. Nat. Rev. Immunol.*, **10**, 297.

Li, D., Meyer, M.H.F., Willkomm, D.K., Keusgen, M., and Hartmann, R.K. (2010) *Analysis of bacterial RNase P RNA and protein interaction by a magnetic biosensor technique. Biochimie*, **92**, 772–778.

von Lieres, E. and Andersson, J. (2010) *A fast and accurate solver for the general rate model of column liquid chromatography. Comput. Chem. Eng.*, **34**, 1180–1191.

Liu, H.F., Mccooey, B., Duarte, T., Myers, D.E., Hudson, T., Amanullah, A., et al. (2011) *Exploration of overloaded cation exchange chromatography for monoclonal antibody purification. J. Chromatogr. A*, **1218**, 6943–6952.

Lu, Y., Williamson, B., and Gillespie, R. (2009) *Recent advancement in application of hydrophobic interactionchromatography for aggregate removal in industrial purification process. Curr. Pharm. Biotechnol.*, **10**, 427–433.

Luellau, E., Von Stockar, U., Vogt, S., and Freitag, R. (1998) *Development of a downstream process for the isolation and separation of monoclonal immunoglobulin A monomers, dimers and polymers from cell culture supernatant. J. Chromatogr. A*, **796**, 165–175.

Lundström, I. and Elwing, H. (1990) *Simple kinetic models for protein exchange reactions on solid surfaces. J. Colloid Interface Sci.*, **136**, 68–84.

Malina, D., Biernat, K., and Sobczak-kupiec, A. (2013) *Studies on sintering process of synthetic hydroxyapatite. Acta Biochim. Pol.*, **60**, 851–855.

Manning, M.C., Chou, D.K., Murphy, B.M., Payne, R.W., and Katayama, D.S. (2010) *Stability of protein pharmaceuticals: An update. Pharm. Res.*, **27**, 544–575.

Marichal-Gallardo, P.A. and Álvarez, M.M. (2012) *State-of-the-art in downstream processing of monoclonal antibodies: Process trends in design and validation. Biotechnol. Prog.*, **28**, 899–916.

Martin, C., Iberer, G., Ubiera, A., and Carta, G. (2005) *Two-component protein adsorption kinetics in porous ion exchange media. J. Chromatogr. A*, **1079**, 105–115.

Mason, B.D., Schöneich, C., and Kerwin, B.A. (2012) *Effect of pH and light on aggregation and conformation of an IgG1 mAb. Mol. Pharm.*, **9**, 774–790.

Maun, H.R., Wen, X., Lingel, A., De Sauvage, F.J., Lazarus, R.A., Scales, S.J., and Hymowitz, S.G. (2010) *Hedgehog pathway antagonist 5E1 binds hedgehog at the pseudo-active site. J. Biol. Chem.*, **285**, 26570–26580.

Mazzer, A.R., Perraud, X., Halley, J., O'Hara, J., and Bracewell, D.G. (2015) *Protein A chromatography increases monoclonal antibody aggregation rate during subsequent low pH virus inactivation hold. J. Chromatogr. A*, **1415**, 83–90.

McCue, J.T., Engel, P., Ng, A., Macniven, R., and Thommes, J. (2008) *Modeling of protein monomer / aggregate purification and separation using hydrophobic interaction chromatography. Bioprocess Biosyst. Eng.*, **31**, 261–275.

McCue, J.T., Engel, P., and Thömmes, J. (2009) *Modeling the effects of column packing quality and residence time changes on protein monomer/aggregate separation. J. Chromatogr. A*, **1216**, 4895–4901.

Melander, W.R., Rassi, Z. el, and Horvath, C. (1989) *Interplay of hydrophpbic and electrostatic interactions in biopolymer chromatography. J. Chromatogr.*, **469**, 3–27.

Milligan, J.R., Catz-Biro, L., and Archer, M.C. (1987) *Effect of phosphate concentration on the yield and purity of DNA separated from RNA by hydroxyapatite chromatography. J. Chromatogr. A*, **411**, 481–485.

Molloy, P.L. (2000) *Electrophoretic mobility shift assays*. In: *Transcription Factor Protocols*, pp. 235–246. Springer.

Morbidelli, M., Servida, A., Storti, G., and Carra, S. (1982) *Simulation of multicomponent

adsorption beds. Model analysis and numerical solution. *Ind. Eng. Chem. Fundam.*, **21**, 123–131.

Morrison, C.J., Gagnon, P., and Cramer, S.M. (2011) *Purification of monomeric mAb from associated aggregates using selective desorption chromatography in hydroxyapatite systems. Biotechnol. Bioeng.*, **108**, 813–821.

Müller-Späth, T., Ströhlein, G., Aumann, L., Kornmann, H., Valax, P., Delegrange, L., et al. (2011) *Model simulation and experimental verification of a cation-exchange IgG capture step in batch and continuous chromatography. J. Chromatogr. A*, **1218**, 5195–5204.

Musante, L., Ravidá, A., Shortt, B., Byrne, B., Saraswat, M., and Holthofer, H. (2013) *Preparative purification of recombinant proteins: current status and future trends. Biomed Res. Int.*, **2013**, 1–18.

Nakanishi, K., Sakiyama, T., and Imamura, K. (2001) *On the adsorption of proteins on solid surfaces, a coomon but very complicated phenomenon. J. Biosci. Bioeng.*, **91**, 233–244.

Norde, W. and Lyklema, J. (2012) *Interfacial behaviour of proteins, with special reference to immunoglobulins. A physicochemical study. Adv. Colloid Interface Sci.*, **179**, 5–13.

O'Shannessy, D.J., Brigham-Burke, M., Soneson, K.K., Hensley, P., and Brooks, I. (1993) *Determination of rate and equilibrium binding constants for macromolecular interactions using surface plasmon resonance: use of nonlinear least squares analysis methods. Anal Biochem*, **212**, 457–468.

Oberholzer, M.R. and Lenhoff, A.M. (1999) *Protein adsorption isotherms through colloidal energetics. Langmuir*, **15**, 3905–3914.

Orlando, V., Strutt, H., and Paro, R. (1997) *Analysis of chromatin structure by in vivo formaldehyde cross-linking. Methods*, **11**, 205–214.

Ortega-Vinuesa, J.L., Tengvall, P., and Lundström, I. (1998) *Molecular packing of HSA, IgG, and fibrinogen adsorbed on silicon by AFM imaging. Thin Solid Films*, **324**, 257–273.

Pabst, T.M. and Carta, G. (2007) *pH transitions in cation exchange chromatographic columns containing weak acid groups. J. Chromatogr. A*, **1142**, 19–31.

Petersen, R.L. (2017) *Strategies using bio-layer interferometry biosensor technology for vaccine research and development. Biosensor*, **7**, 49.

Qamar, S., Akram, N., and Seidel-Morgenstern, A. (2016) *Analysis of general rate model of linear chromatography considering finite rates of the adsorption and desorption steps.*

Chem. Eng. Res. Des., **111**, 13–23.

Qamar, S., Nawaz Abbasi, J., Javeed, S., and Seidel-Morgenstern, A. (2014) *Analytical solutions and moment analysis of general rate model for linear liquid chromatography. Chem. Eng. Sci.*, **107**, 192–205.

Rabe, M., Verdes, D., and Seeger, S. (2011) *Understanding protein adsorption phenomena at solid surfaces. Adv. Colloid Interface Sci.*, **162**, 87–106.

Ramirez-gutierrez, C.F., Londoño-restrepo, S.M., Real, A., and Mondragón, M.A. (2017) *Effect of the temperature and sintering time on the thermal, structural, morphological, and vibrational properties of hydroxyapatite derived from pig bone. Ceram. Int.*, **43**, 7552–7559.

Ratner, B.D., Hoffman, A.S., Schoen, F.J., Lemons, J.E., Dyro, J., Martinsen, O.G., et al. (2009) *Biomedical engineering desk reference*. Academic Press.

Reck, J.M., Pabst, T.M., Hunter, A.K., and Carta, G. (2017) *Separation of antibody monomer-dimer mixtures by frontal analysis. J. Chromatogr. A*, **1500**, 96–104.

Reck, J.M., Pabst, T.M., Hunter, A.K., Wang, X., and Carta, G. (2015) *Adsorption equilibrium and kinetics of monomer – dimer monoclonal antibody mixtures on a cation exchange resin. J. Chromatogr. A*, **1402**, 46–59.

Roh, C., Kim, S.E., and Jo, S.K. (2011) *Label free inhibitor screening of hepatitis C virus (HCV) NS5B viral protein using RNA oligonucleotide. Sensors*, **11**, 6685–6696.

Ruthven, D.M. (1984) *Principles of adsorption and adsorption processes*. WILEY-VCH Verlag.

Saito, M., Kurosawa, Y., and Okuyama, T. (2012) *Purification of anti-japanese encephalitis virus monoclonal antibody by ceramic hydroxyapatite chromatography without proteins A and G. Hybridoma*, **31**, 68–71.

Saito, M., Yoshitake, T., and Okuyama, T. (2016) *Separation and analysis of charged isomers of monoclonal immunoglobulin G by ceramic hydroxyapatite chromatography. Prep. Biochem. Biotechnol.*, **46**, 215–221.

Schmoeger, E., Paril, C., Tscheliessnig, R., and Jungbauer, A. (2010) *Adsorption of plasmid DNA on ceramic hydroxyapatite chromatographic materials. J. Sep. Sci.*, **33**, 3125–3136.

Schneider, P. and Smith, J.M. (1968) *Adsorption rate constants from chromatography. AIChE J.*, **14**, 762–771.

Schröder, M., Schäfer, R., and Friedl, P. (2002) *Induction of protein aggregation in an early*

secretory compartment by elevation of expression level. *Biotechnol. Bioeng.*, **78**, 131–140.

Schubert, S. and Freitag, R. (2009) *Investigation of the interaction mechanism of the recombinant human antibody MDJ8 and its fragments with chromatographic apatite phases*. *J. Chromatogr. A*, **1216**, 3831–3840.

Sejergaard, L., Karkov, H.S., Krarup, J.K., Hagel, A.B.B., and Cramer, S.M. (2014) *Model-based process development for the purification of a modified human growth hormone using multimodal chromatography*. *Biotechnol. Prog.*, **30**, 1057–1064.

Selvarajah, S., Sexton, N.R., Kahle, K.M., Fong, R.H., Mattia, K.A., Gardner, J., et al. (2013) *A neutralizing monoclonal antibody targeting the acid-sensitive region in chikungunya virus E2 protects from disease*. *PLoS Negl. Trop. Dis.*, **7**, e2423.

Shi, X.L., Feng, M.Q., Shi, J., Shi, Z.H., Zhong, J., and Zhou, P. (2007) *High-level expression and purification of recombinant human catalase in Pichia pastoris*. *Protein Expr. Purif.*, **54**, 24–29.

Shukla, A.A., Hubbard, B., Tressel, T., Guhan, S., and Low, D. (2007) *Downstream processing of monoclonal antibodies-Application of platform approaches*. *J. Chromatogr. B Anal. Technol. Biomed. Life Sci.*, **848**, 28–39.

Sing, K.S.W. (1982) *Reporting physisorption data for gas/solid systems*. *Pure Appl. Chem.*, **54**, 2201–2218.

Stanker, L.H. and Vanderlaan, M. (1985) *One-step purification of mouse monoclonal antibodies from ascites fluid by hydroxylapatite chromatography*. *J. Immunol. Methods*, **76**, 157–169.

Stanker, L.H., Vanderlaan, M., and Juarez-Salinas, H. (1985) *One-step purification of mouse monoclonal antibodies from ascites fluid by hydroxylapatite chromatography*. *J. Immunol. Methods*, **76**, 157–169.

Stockley, P.G. (2009) *Filter-binding assays*. In: *DNA-Protein Interactions* , pp. 1–14. Springer.

Stone, M.T., Cotoni, K.A., Stoner, J.L., and Jayson, L. (2019) *Cation exchange frontal chromatography for theremoval of monoclonal antibody aggregates*. *J. Chromatogr. A*, **1599**, 152–160.

Strube, J., Haumreisser, S., Schmidt-Traub, H., Schulte, M., and Ditz, R. (1998) *Comparison of batch elution and continuous simulated moving bed chromatography*. *Org. Process Res. Dev.*, **2**, 305–319.

Sukumar, M., Doyle, B.L., Combs, J.L., and Pekar, A.H. (2004) *Opalescent appearance of an*

IgG1 antibody at high concentrations and its relationship to noncovalent association. Pharm. Res., **21**, 1087–1093.

Sun, S., Gallo, C., and Kelley, B. (2016) *Removal of high molecular weight aggregates using hydroxyapatite chromatography.* U.S. Patent No. 9,469,672.

Tan, H., Chen, D.J., Tan, Y., and Witte, K.L. (2008) *Fiber-optic assay apparatus based on phase-shift interferometry.* U.S. Patent No. 7,394,547.

Tao, Y., Chen, N., Carta, G., Ferreira, G., and Robbins, D. (2012) *Modeling multicomponent adsorption of monoclonal antibody charge variants in cation exchange columns. AIChE J.*, **58**, 2503–2511.

Tiselius, A., Hjertén, S., and Levin, Ö. (1956) *Protein chromatography on calcium phosphate columns. Arch. Biochem. Biophys.*, **65**, 132–155.

Vázquez-Rey, M. and Lang, D.A. (2011) *Aggregates in monoclonal antibody manufacturing processes. Biotechnol. Bioeng.*, **108**, 1494–1508.

Verzijl, D., Riedl, T., Parren, P.W.H.I., and Gerritsen, A.F. (2017) *Biosensors and Bioelectronics A novel label-free cell-based assay technology using biolayer interferometry. Biosens. Bioelectron.*, **87**, 388–395.

Wang, Y. and Carta, G. (2019) *Competitive binding of monoclonal antibody monomer-dimer mixtures on ceramic hydroxyapatite. J. Chromatogr. A*, **1587**, 136–145.

Watanabe, T., Makitsuru, K., Nakazawa, H., Hara, S., Suehiro, T., Yamamoto, A., et al. (1999) *Separation of double-strand DNA fragments by high-performance liquid chromatography using a ceramic hydroxyapatite column. Anal. Chim. Acta*, **386**, 69–75.

Weinbrennef, W.F. and Etzel, M.R. (1994) *Competitive adsorption of α-lactalbumin and bovine serum albumin to a sulfopropyl ion-exchange membrane. J. Chromatogr. A*, **662**, 414–419.

Werner, A. (2010) *Predicting translational diffusion of evolutionary conserved RNA structures by the nucleotide number. Nucleic Acids Res.*, **39**, e17.

Wilson, E.J. and Geankoplis, C.J. (1966) *Liquid mass transfer at ever low reynolds numbers in packed beds. Ind. Eng. Chem. Fundamen.*, **5**, 9–14.

Wollacott, B.R.B., Roth, L.E., Sears, T.L., Sharpe, R.A., Jiang, M., and Ozturk, S.S. (2015) *The development of a flow-through mode cation exchange process for the purification of a monoclonal antibody. Bioprocess. J.*, **14**.

Wu, Y., Abraham, D., and Carta, G. (2016) *Comparison of perfusion media and monoliths for*

protein and virus-like particle chromatography. *J. Chromatogr. A*, **1447**, 72–81.

Xu, H., Lu, J.R., and Williams, D.E. (2006) *Effect of surface packing density of interfacially adsorbed monoclonal antibody on the binding of hormonal antigen human chorionic gonadotrophin. J. Phys. Chem. B*, **110**, 1907–1914.

Yamamoto, S. (1995) *Plate height determination for gradient elution chromatography of proteins. Biotechnol. Bioeng.*, **48**, 444–451.

Yang, H. and Etzel, M.R. (2003) *Evaluation of three kinetic equations in models of protein purification using ion-exchange membranes. Ind. Eng. Chem. Res.*, **42**, 890–896.

Yao, Y. and Lenhoff, A.M. (2004) *Determination of pore size distributions of porous chromatographic adsorbents by inverse size-exclusion chromatography. J. Chromatogr. A*, **1037**, 273–282.

Zafir-Lavie, I., Michaeli, Y., and Reiter, Y. (2007) *Novel antibodies as anticancer agents. Oncogene*, **26**, 3714–3733.

Zenhäusern, R. and Rippin, D.W.T. (1998) *Modelling and simulation of multicomponent nonlinear chromatography. Comput. Chem. Eng.*, **22**, 259–281.

Zhang, L., Parasnavis, S., Li, Z., Chen, J., and Cramer, S. (2019) *Mechanistic modeling based process development for monoclonal antibody monomer-aggregate separations in multimodal cation exchange chromatography. J. Chromatogr. A*, **1602**, 317–325.

Zhang, Y.B., Howitt, J., McCorkle, S., Lawrence, P., Springer, K., and Freimuth, P. (2004) *Protein aggregation during overexpression limited by peptide extensions with large net negative charge. Protein Expr. Purif.*, **36**, 207–216.